12-1992

Channel, a Model of Channel Erosion by Shear, Scour and Channel Headwall Propagation: Part 1. Model Development

Digital Object Identifier: https://doi.org/10.13023/kwrri.rr.186

Alex W. Fogle
University of Kentucky, alex.fogle@uky.edu

Billy J. Barfield
Oklahoma State University

Research Report No. 186

CHANNEL, A MODEL OF CHANNEL EROSION BY SHEAR, SCOUR AND CHANNEL HEADWALL PROPAGATION: PART 1. MODEL DEVELOPMENT

by

Alex W. Fogle
Hydrologist III
Kentucky Geological Survey
University of Kentucky
Lexington, KY 40506

Billy J. Barfield
Emeritus Professor
Department of Agricultural Engineering
University of Kentucky
Lexington, KY 40546
Currently: Professor and Chairman
Department of Agricultural Engineering
Oklahoma State University
Stillwater, OK 74074

Water Resources Research Institute
University of Kentucky
Lexington, KY

December, 1992

ABSTRACT

In the research conducted under this project, models were developed which predict channel erosion resulting from shear in gradually varied flow, shearing forces resulting from submerged jets and hydraulic jumps, and shearing forces resulting from free jets impinging a plunge pool. These models are linked with a runoff routing algorithm to develop the CHANNEL model. This model predicts general channel erosion resulting from time varying gradually varied flow as well as predicts the development and propagation of channel headwalls. At this writing, the model still has some problems handling the transition from open channel flow to a free jet within the scour hole.

Descriptors:

Channels, Erosion, Erosion Rates, Model Studies, Scour, Shear, Channel Scour

TABLE OF CONTENTS

LIST OF FIGURES

CHAPTER 1

INTRODUCTION AND MODEL OVERVIEW

1.1. INTRODUCTION

Channel erosion in upland watersheds is the general topic of this report, with specific emphasis on the fundamental mechanics of channel erosion resulting from the development of channel (gully) headwalls and scour holes, and from general shear excess. The emphasis is on erosion in channels with cohesive boundaries.

Entry of sediment into our nations waterways is a serious pollution problem, intensified by the chemicals adsorbed on the exchange phase of clay particles in the sediment. The subject of upland erosion from rill and interrill areas has been the subject of intensive investigations, both empirical and physically based. Channel erosion has been studied primarily from an empirical basis, with virtually little physically based information on channel headwall development and propagation and of channel bank failure. Both of these mechanisms are major sources of sediment.

In the research conducted under this project, models were developed which predict channel erosion resulting from shear in gradually varied flow, shearing forces resulting from submerged jets and hydraulic jumps and shearing forces resulting from free jets impinging a plunge pool. These models are linked with a runoff routing algorithm to develop the CHANNEL model. This model predicts general channel erosion resulting from time varying gradually varied flow as well as from the development and propagation of channel headwalls.

The modeling approach is modular and fundamentally based. New equations are easily incorporated.

1.2. OVERVIEW OF CHANNEL EROSION FROM HEADCUTTING

The growth of a channel through headwall cutting contributes significantly to the overall sediment yield of a watershed. A headwall is a transition point between flow in channels with wide shallow flow and narrow deeper flows. This point is also referred to as a knickpoint or a knickzone (dependent upon the sharpness of the overfall) or a scarp. Much of the information related to headwall cutting is derived from data on drainage basin morphology (Harvey et al., 1985; Schumm et al., 1984).

Although complete models of headwall development using physically based algorithms have not been available, recent advances have made possible the development of a first generation algorithm. A major step toward this end was made with the development of a physically based model of shear distribution from an impinging oblique jet. Beltoas (1976a, 1976b) and Beltoas and Rajaratnam (1973, 1974, 1977) provide perhaps the most significant development which allows the shear distribution of an impinging oblique jet to be calculated based on the impact angle, jet exit velocity and flow length through the plunge pool. When combined with relationships for brink depth and velocity (Delleur et al., 1956; Rouse, 1936, 1943) and equations for the trajectory of the overfall, the development of a scour hole can be estimated.

Two recent studies have shed some light on the stability and propagation of knickpoints. May (1989) summarized the work associated with development and migration of scour holes and knickpoints associated with emergency spillways. Quoting researchers including Brush and Wolman (1960), May indicates that knickpoints will wash out if the channel bed is homogeneous or if an erosion resistant material underlies an easily eroded material. Knickpoints, according to May, only maintain their identity and migrate upstream when an erosion resistant material overlays a more easily eroded material. May (1989) also proposes that an unventilated overfall will cause more scour than a ventilated overfall.

Stein (1990) improved on the Brush and Wolman (1960) concept and showed

mathematically that knickpoints could maintain a semi-vertical face and propagate upstream, even if the upstream and downstream materials were homogeneous and had the same properties. Starting with the assumption of an overfall of height H existing at time zero, Stein used the concept of shear excess and a model of increased shear due to the acceleration at the brink to predict the time t_1 required to wash out a knickpoint headwall. Using impinging jet theory and a shape function for the plunge pool, Stein predicted the time t_2 required for the plunge pool to undercut the headwall. The ratio of t_1 to t_2 determines whether or not the knickpoint will wash out or remain stable.

The Stein model assumes that a knickpoint has been developed at time zero by some mechanism and that soils are homogeneous. Models are needed to predict development of a knickpoint and propagation under nonhomogeneous conditions.

1.3. CONCEPTUAL BASIS FOR THE MODEL

The fundamental approach in the CHANNEL model is the premise that a critical tractive force exists and that detachment potential is proportional to the excess of shear over critical tractive force (Foster, 1982; Haan et al., 1992) or:

$$D_{rc} = K (\tau - \tau_c) \tag{1}$$

where D_{rc} is detachment potential (kg s^{-1} m^{-2}), K is an erodibility constant (s m^{-1}), τ is the shear on the channel boundary (Pa) and τ_c is critical tractive force (Pa). K and τ_c are soil properties. The premise of a shear excess has been questioned for non-cohesive soils (Einstein, 1950) but has been used widely to predict concentrated flow detachment for cohesive soils (Foster and Lane, 1983; Hirschi and Barfield, 1988a; 1988b; Lane and Nearing, 1989). Wilson (1992) proposed a more fundamental approach to detachment based on a probability distribution of lift forces causing detachment and found that detachment is defined by an exponential function with parameterized constants. At the present time, values for the constants are not available, thus equation (1) will be used as the basic detachment model.

Based on the shear excess concept, areas along a channel will exist where $\tau<\tau_c$ due to soil properties or flow conditions. When these conditions exist adjacent to areas with $\tau>\tau_c$, the conditions are favorable to formation of a headwall scour hole.

The scour hole development model in CHANNEL is based on the following concepts:

1. Due to changes in flow or differences in soil properties, a scour hole can be found at a point where a transition occurs from $\tau<\tau_c$ to $\tau>\tau_c$.

2. Detachment starts at the point where τ first exceeds τ_c and ends when sediment load reaches the transport capacity.

3. As detachment continues a scour hole is formed. After sufficient detachment, a submerged jet and/or hydraulic jump forms. The submergence results from downstream tailwater controls.

4. After sufficient downstream scour, the tailwater depth is lowered below the brink elevation and the jet becomes a free jet. At this point, a knickpoint (headwall) is formed.

5. Additional detachment, after the jet becomes a free jet, causes undercutting of the headwall. With sufficient undercutting, the headwall becomes unstable and fails. Thus a new headwall is formed and the scour hole moves upslope into the segment

where $\tau<\tau_c$.

After an overfall is generated, there will be an increased shear near the brink resulting from the increased energy slope near the overfall. Under some flow conditions, this increase will be such that the critical tractive force is exceeded and the headwall will wash out (Stein, 1990) reverting the flow to an open channel.

CHAPTER 2

MODEL DEVELOPMENT

The goal of this work was to pull together existing models of flow routing, free jet geometry, shear distributions, detachment/deposition processes, and channel geometry to develop a first generation model of the various channel processes that include headwall development and propagation. The following discussion is a presentation of the models and equations used to develop the framework for the CHANNEL model. The application of these models and equations to physical situations is discussed in Chapter 3. At this point, discussion will begin with the flow routing model, progress through free jet geometry modeling, shear modeling, detachment/deposition processes modeling, and, finally, end with a discussion of modeling channel shape or geometry.

2.1. FLOW ROUTING

The function of the flow routing algorithms are to determine the area, depth of flow and velocity of any point on the channel, given input channel cross sections, lateral inflows and inflow at the top of the channel. The scour hole is considered a control section and routing progresses up or downstream, as appropriate using a steady state standard step method.

2.1.1. Steady State Standard Step Method

The simplest routing procedure is the standard step method (Chow, 1959). The procedure utilized involves total energy calculations between two points on a channel. Given that total energy at point i is

$$h_i = d_i + Y_i + \alpha \frac{V_i^2}{2g} \tag{2}$$

and

$$h_i = h_{i+1} + h_{f_{i,i+1}} \tag{3}$$

then

$$h_i = d_i + Y_i + \alpha \frac{V_i^2}{2g} = d_{i+1} + Y_{i+1} + \alpha \frac{V_{i+1}^2}{2g} + h_{f_{i,i+1}} \tag{4}$$

where

$$h_{f_{i,i+1}} = S_{f_a} \Delta X + \frac{1}{2} (S_{f_i} + S_{f_{i+1}}) \Delta X \tag{5}$$

h_i is the total energy head, d_i is the depth of flow (measured from the lowest point on the boundary), Y_i is the elevation of the lowest point on the boundary, V_i is the average velocity on the cross section, ΔX is the segment length, $h_{fi,i+1}$ is the head loss due to friction on ΔX, S_{fa} is the average friction slope on ΔX and S_{fi} is the friction slope at i. S_{fi} is calculated from Manning's equation or

$$S_f = \left[\frac{n\ Q/A}{C_n R^{2/3}}\right]^2 \tag{6}$$

where n is Manning's roughness, A is cross sectional area, Q is flow rate, C_n is a constant (1.5 for English units, 1.0 for SI units) and R is hydraulic radius given by

$$R = \frac{A}{P} \tag{7}$$

where A is area and P is wetted perimeter.

2.2. FREE JET GEOMETRY IN OVERFALL

The important parameters for jet geometry are the impingement angle, impingement velocity and the width of the jet at the point of plunge. These parameters are controlled by the flow depth and velocity, curvature, and bed slope at the brink. Flow depth is related to the end-depth ratio. A definition sketch of jet geometry is given in Figure 2.1.

2.2.1. End-Depth Ratio

2.2.1.1. Subcritical Flow

The flowrate over a free overfall is defined by flow depth at the brink. If the approaching flow is subcritical, then the flow profile passes through critical depth and flow becomes supercritical before reaching the brink. Several investigators have shown (Rajaratnam et al., 1976; Rouse, 1936, 1943; Delleur et al., 1956) that, in general, brink depth is influenced by channel slope, channel roughness, and channel cross-sectional configuration.

Delleur et al. (1956) determined that Rouse's (1936) contraction constant, d_b/d_c (brink depth divided by critical depth), was dependent upon flowrate and channel bed slope. This constant, referred to as end-depth ratio (EDR), was related to these parameters by a ratio of bed slope to critical slope. Experiments were conducted by Delleur et al. (1956) in a 9.14 m long, 0.61 m wide, glass tilting flume. Critical depths ranged from 0.030 to 0.121 m, but only discharges corresponding to 0.061 and 0.121 m depths were reported. Slopes varied between -0.02 and 0.03. A smooth channel and an artificially roughened (6.4 mm square brass strips) channel were studied. A plot of these results indicated minimal change in end-depth ratio for adverse slopes, rapid variation for changes in mild slope, and a relative leveling off for steep slope changes. Roughness was shown to have little influence.

Delleur et al. (1956) proposed that the end-depth ratio for subcritical flow be given by Figure 2.2. The following equation fits the data over the range - $10 \leq S_R \leq 20$:

$$EDR = \frac{d_b}{d_c} = .6971 - .0232\ S_R - .0019\ S_R^2 + .000153\ S_R^3 + 8.56 \times 10^{-6}\ S_R^4 - 7.7 \times 10^{-7}\ S_R^5 + 1.26 \times 10^{-6}\ S_R^6 \tag{8}$$

where d_b is the brink depth, d_c is the critical depth and S_R is the ratio:

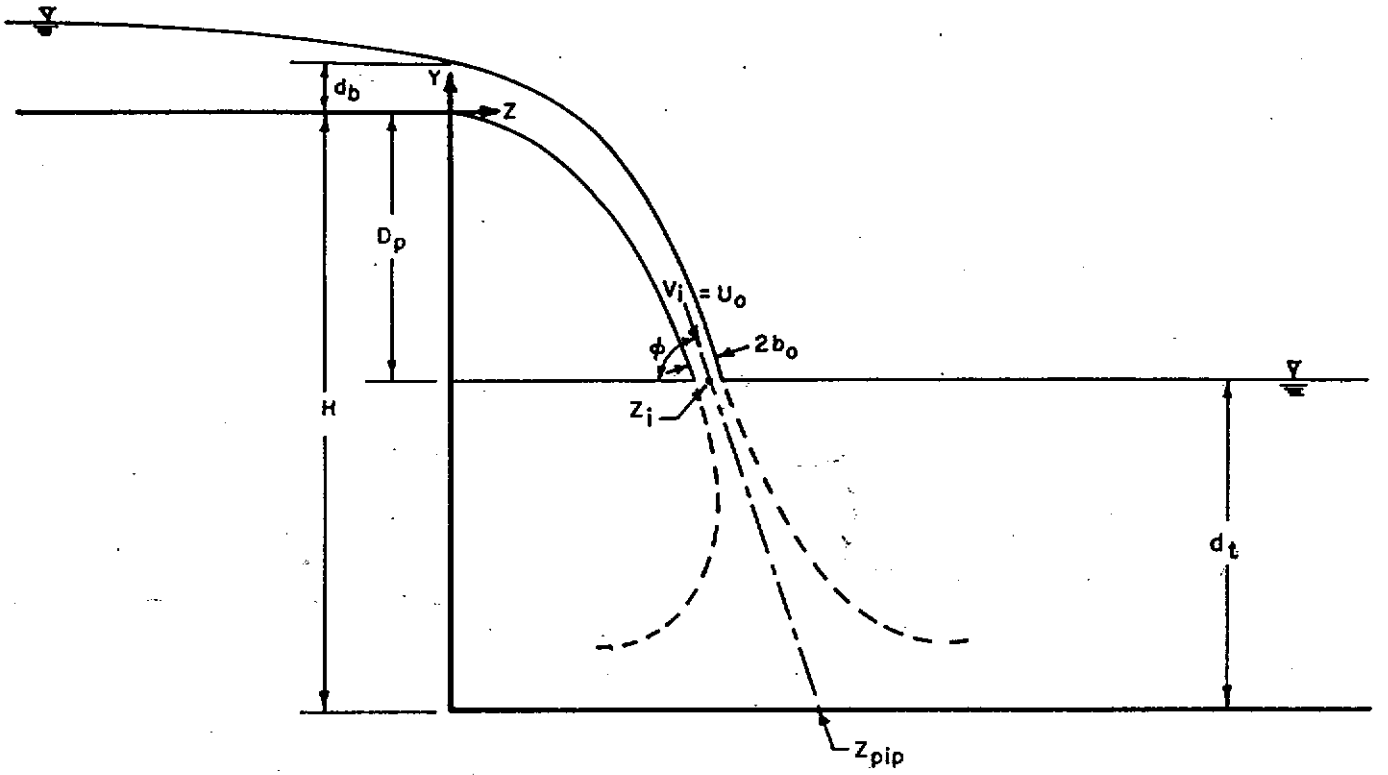

Figure 2.1. Definition sketch of free jet in overfall.

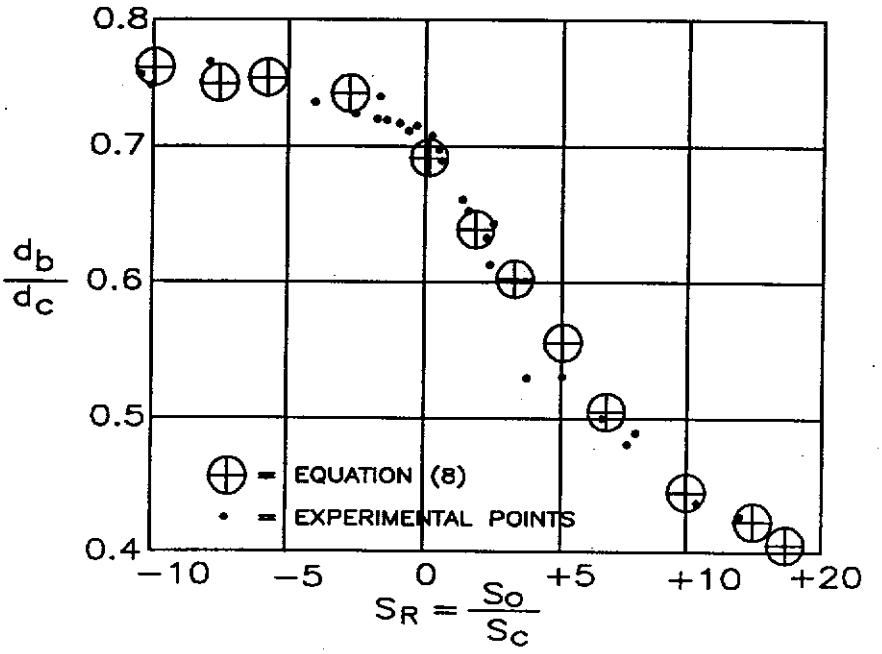

Figure 2.2. End-depth ratio as a function of the ratio of bed slope to critical slope (after Delleur et al., 1956)

$$S_R = \frac{S_o}{S_c} \tag{9}$$

where S_o is the upstream channel slope and S_c is the critical slope.

In contrast to the Delleur et al. (1956) study, a subsequent investigation by Rajaratnam et al. (1976) indicated that roughness was, indeed, an important factor in end depth determination. In preliminary testing with wire screen and glass marble roughnesses, EDR varied significantly from that of hydraulically smooth channels. Four series of tests were conducted in a 0.46 m wide, 0.38 m deep, 6.10 m long Plexiglas flume. If channel roughness scale to critical depth ratio (k_s/d_c) was less than or equal to 0.1, then EDR was the same as that for smooth channels; for values of k_s/d_c greater than 0.1, EDR was smaller than smooth channel EDR (approximately 80% of smooth channel EDR for $k_s/d_c = 0.45$). In another test using roughness strips similar to those used by Delleur et al. (1956), Rajaratnam et al. (1976) found that geometric as well as friction factors influenced end-depth ratio and that pressure distribution at the brink was essentially the same as that in a smooth channel.

A correction for upstream roughness can be made to the brink depth (d_b) using a linear regression on the Rajaratnam et al. (1976) data by:

$$RF = -0.75 + 1.05 \frac{d_c}{k_s}; \quad \frac{d_c}{k_s} \leq 10 \tag{10}$$

$$RF = 1; \quad \frac{d_c}{k_s} > 10 \tag{11}$$

where d_c is critical depth and k_s is bed grain roughness given by d_{65}. Thus the brink depth can be corrected for roughness by:

$$d_b = d_c\,(EDR)(RF); \quad \frac{d_c}{k_s} \leq 10 \tag{12}$$

$$d_b = d_c(EDR); \quad \frac{d_c}{k_s} > 10 \tag{13}$$

These relationships apply to well-ventilated overfalls. For unventilated overfalls, pressure acting on the lower streamline of discharging flow is greater than ambient. This alters the pressure distribution throughout the free stream and consequently changes end-depth ratio relationships as well as the path of the free falling fluid jet (Blevins, 1984). In addition, this pressure pocket induces unstable jet oscillations.

2.2.1.2. Supercritical Flow

For supercritical flow, the reference depth upstream is normal flow depth. For this case Hager (1983, 1984) showed that end-depth ratio, defined as the ratio of brink depth to upstream normal depth, could be calculated from:

$$EDR = \frac{d_b}{d_n} = \frac{F_o^2}{F_o^2 + \frac{4}{9}} \tag{14}$$

where F_o is the upstream Froude number given by:

$$F_o = \frac{U_n}{\sqrt{g\, d_n}} \tag{15}$$

where U_n is the upstream velocity corresponding to normal depth, d_n; and g is the acceleration of gravity.

The end-depth ratio can be corrected for roughness using equations (12) and (13) with equation (14) used to calculate EDR.

2.2.2. Jet Thickness

Rouse (1936) used the momentum principle to derive an expression for vertical stream thickness. The rate of change of momentum in the horizontal direction caused by static pressure forces was set equal to the mass discharge passing a stream section, with boundary friction losses being ignored, i.e.:

$$\frac{\gamma d_c w}{2} = \frac{Q\gamma}{g} \Delta V = \frac{Q^2 \gamma}{g w \kappa_1} - \frac{Q^2 \gamma}{g w d_c} \tag{16}$$

where Q was total flowrate, γ was specific weight of the fluid, κ_1 was vertical stream thickness measured downstream of the brink, w was channel width, and other variables were the same as previously defined. Since,

$$d_c^3 = \frac{Q^2}{g w^2} \tag{17}$$

Equation (16) was written as:

$$\frac{d_c^2}{2} = \frac{d_c^3}{\kappa_1} - \frac{d_c^3}{d_c} \tag{18}$$

which was solved for d_1 as:

$$\kappa_1 = \frac{2}{3} d_c \tag{19}$$

Thus, the ratio of vertical jet thickness to critical depth was exactly 2/3. Experiments showed that after the stream passes the overfall, where pressure was atmospheric, vertical thickness was slightly greater than two-thirds of critical depth, due to neglected boundary resistance. For critical flow, Strelkoff and Moayeri (1970) computed a ratio of vertical stream thickness to upstream flow depth of 0.672.

2.2.3. Jet Profile

A free falling jet may be described by simple particle trajectory physics relationships, potential flow theory, or an extension of Bernoulli's energy equation (Strelkoff and Moayeri, 1970; Hager, 1983, 1984).

2.2.3.1. Subcritical Flow

The fluid jet trajectory can be evaluated by simple projectile physics when flow upstream of the brink is subcritical. Rouse (1936) presented an analysis of the jet/projectile problem by considering gravity and inertial forces while ignoring viscous forces. For long jets, shear and viscous forces would cause shear interaction, causing the jet to break into many droplets (Doddiah et al., 1953). Using simple particle physics:

$$a_z = \frac{dV_z}{dt} = 0 \tag{20}$$

$$a_y = \frac{dV_y}{dt} = -g \tag{21}$$

where a_z and a_y are horizontal and vertical accelerations, V_z and V_y are horizontal and vertical velocities, and t is time. Integrating with respect to time yields velocity expressions for any time:

$$V_z = (V_{oz}) \tag{22}$$

$$V_y = (V_{oy}) - gt \tag{23}$$

where (V_{oz}) and (V_{oy}) were initial horizontal and vertical velocities. Since $V_z = dz/dt$ and $V_y = dy/dt$, further integration with respect to time yields location expressions for z and y along the jet trajectory, or:

$$z = (V_{oz})\, t \tag{24}$$

$$y = (V_{oy})\, t - \frac{gt^2}{2} \tag{25}$$

The slope of the streamline at any time can be determined from dy/dz, and thus converted into an angle. From differential calculus:

$$\frac{dy}{dt} = \frac{dy}{dz}\,\frac{dz}{dt} \tag{26}$$

thus:

$$\frac{dy}{dz} = \frac{\frac{dy}{dt}}{\frac{dz}{dt}} \tag{27}$$

Using equations (24) and (25) for y and z,

$$\left.\frac{dy}{dz}\right|_i = \frac{V_{oy} - gt_i}{V_{ox}} \tag{28}$$

where i denotes the point of impact of the jet with the plunge pool, and t_i is the time required for a particle to travel from the brink to the point of impact, determined by solving equation (25) for t_i with y equal to the distance D_p in Figure 2.1. The jet angle at impact becomes:

$$\phi = \tan^{-1} \left.\frac{dy}{dz}\right|_i \tag{29}$$

At the point of impact, the total velocity would be (Rouse, 1936):

$$V_i = \sqrt{V_z^2(t_i) + V_y^2(t_i)} \tag{30}$$

or:

$$V_i = \sqrt{V_{ox}^2 + (V_{oy} - gt_i)^2} \tag{31}$$

Equation (31) would be used to determine the impact velocity and equation (29) the angle of impact.

The vertical thickness of the jet is assumed to be constant (Rouse, 1936). Thus at impact, the horizontal width of the jet is

$$2b_o = d_b \cos\phi \tag{32}$$

where b_o is the jet half width.

Jet trajectories in CHANNEL are calculated with simple particle physics for subcritical flow. For supercritical flow, more complicated relationships are needed, as discussed below.

2.2.3.2. Supercritical Flow

When flow upstream of the brink becomes supercritical, the jet trajectory can no longer be described by a simple particle trajectory. In this case inertial forces are such that curvature of streamlines affect the total energy. Strelkoff and Moayeri (1970) utilized conformal mapping to solve for the jet trajectory. The method is extremely complicated, but yields accurate predictions.

A simpler relationship was developed by Hager (1983) using the total energy equation

$$H = y + \frac{h}{2} + \left(\frac{q^2}{2gh^2}\right)\left(1 + \frac{2hh'' - h^{2'}}{3} + hy'' = h'y' - y^2\right) \tag{33}$$

where H was total energy head, y and y' are elevation head and its first derivative, h, h', and h" is pressure head and its first and second derivatives, q is specific discharge, and g is acceleration of gravity. Hager (1983) utilized equation (33) and other relationships to develop equations for the trajectory of the overfall. The slope of the jet streamline at the brink is given by

$$\left(\left.\frac{dy}{dx}\right|_{brink}\right)^2 = \psi^2 = \frac{1 - \frac{T_e}{2} + \frac{F_o^2}{2}\left(1 - \frac{1}{T_e^2}\right)}{\left(\frac{F_o^2}{T_e^2} + \frac{3T_e}{4}\right)} \tag{34}$$

where T_e is the end-depth ratio given by:

$$T_e = \frac{d_b}{d_n} \tag{35}$$

Equation (34) yields streamline slope normalized by the upstream normal depth. Actual slope is obtained by multiplying the slope from equation (34) by the normal depth.

Given the value for T_e, Hager (1983, 1984) developed the trajectory equation for the lower overfall jet surface:

$$z = \frac{1}{\varepsilon}\left[\sqrt{\psi^2 - 2\varepsilon y} - \psi\right] \tag{36}$$

where:

$$\varepsilon = \left(\frac{T_e}{F_o}\right)^2 \tag{37}$$

Thus, knowing ψ from (34) and ε from the end-depth ratio and upstream Froude Number, the value of z for any y can be computed, thus the z, y coordinates of the point of intersection of the jet with the tailwater can be easily determined from the tailwater elevation by setting y equal to D_p in equation (36).

In order to obtain ϕ, the angle of entry of the jet at the tailwater surface, equation (36) can be inverted and differentiated to obtain

$$\left.\frac{dy}{dx}\right|_{D_p} = \tan\phi = -\left[\psi + \varepsilon z_j\right] \tag{38}$$

where:

$$\varepsilon = \left(\frac{T_e}{F_o}\right)^2 = \left(\frac{\frac{d_b}{d_n}}{\frac{U_n}{\sqrt{g\,d_n}}}\right)^2 \tag{39}$$

where z_i is the point of jet entry into the plunge pool obtained from equation (36).

2.3. SHEAR DETERMINATION

Two types of shear distributions are needed, lateral and longitudinal. In the sections where flow is treated as gradually varied channel flow, shear changes along the direction of flow will be small relative to lateral changes in shear along the boundary. In this case shear changes along the direction of flow are predicted from the flow routing equations and a lateral shear distribution is needed to predict changes in the channel geometry due to shear excess detachment. In the scour hole, the changes in shear along the horizontal flow direction will be large, requiring prediction equations for a shear profile along the direction of flow which are not a function of energy gradient.

2.3.1. Lateral Shear Distribution: Open Channel Flow

Foster and Lane (1983) assumed a symmetrical shear distribution, given by:

$$\tau_* = \frac{\tau}{\tau_a} = 1.35\ [1 - (1 - 2x_*)^{2.9}]; \quad x_* \le 0.5 \tag{40}$$

where τ is actual shear at any x_*, x_* is a normalized distance along the boundary given by

$$x_* = \frac{x}{WP} \tag{41}$$

where x is the distance along the boundary, WP is the wetted perimeter and τ_a is the average shear given by:

$$\tau_a = \gamma R S_f \tag{42}$$

where γ is weight density of water, R is hydraulic radius and S_f is the slope of the energy gradient. Equation (40) does not account for the effect of channel geometry on shear stress distribution. Wang, Foster, and Wilson (1992) modified equation (40) to consider the variation of maximum shear stress with changing width-depth ratios, and presented the more general relationship:

$$\tau_* = \frac{\tau}{\tau_a} = \left(1 + \frac{1}{\zeta}\right)[1 - (1 - 2x)^{\zeta}] \tag{43}$$

for width-to-depth ratios greater than or equal to 2.8 where

$$\zeta = \left[\frac{2w}{d}\right]^{\frac{1}{2}} \tag{44}$$

where w is the channel width and d is the flow depth. For channels where the width-depth ratio is between 1.0 and 2.8 the following was given:

$$\tau_* = \sigma\left[1 - (1 - 2x)^{\frac{1}{\sigma - 1}}\right] \tag{45}$$

where

$$\sigma = 1.1226\left(\frac{w}{d}\right)^{0.23} \tag{46}$$

For a non-symmetrical channel with actual flow data, the shear distribution could be determined from a knowledge of isovels (lines of constant velocity) at a cross section. According to Raudkivi (1976), if orthogonals to the isovels are constructed at equal increments ΔWP_i along the boundary (See Figure 2.3a), the area between adjacent isovels, ΔA_i, can be used to determine the shear distribution from

$$\tau_i = \frac{\gamma\ \Delta A_i\ S_f}{\Delta WP_i} \tag{47}$$

where τ_i is the shear in increment i and ΔA_i and ΔWP_i refer to incremental values of area and wetted perimeter. This method has been used by many researchers to define shear distribution. Leighly (1932) used the method with actual velocity profile data to define shear distribution. Lane (1953, 1955) utilized a power equation to represent the orthogonals where the isovels were not measured. Rohlf (1981) utilized Lane's power equation adding the requirement that the orthogonals be perpendicular to the boundary. A simpler procedure known as the area method was proposed by Lundgren and Jonsson (1964) as illustrated in Figure 2.3b. In this case lines are constructed perpendicular to the channel boundary and projected to the water surface. The area between adjacent projections is utilized in equation (47) for ΔA_i. Hirschi and Barfield (1988a) tested the Lundgren and Jonsson method against data taken by Replogle and Chow (1966) and found that the area method was generally more accurate than either Rohlf's method or that of Foster and Lane (1983). Procedures whereby the shear is translated into detachment are given in a later section.

2.3.2. Longitudinal Shear Distribution: Scour Hole

The shear distribution in the scour hole will be calculated separately depending on whether the flow is open channel flow with an hydraulic jump (curves 6, 7, 8, Figure 2.4), submerged jet, curve 5, Figure 2.4, or impinging jet. The discussion will start with the free jet in order to develop needed relationships. If the flow is an impinging jet, an overfall exists and the location and angle of entry of the jet into the free water surface must be calculated. These parameters are then used as input information to the free jet.

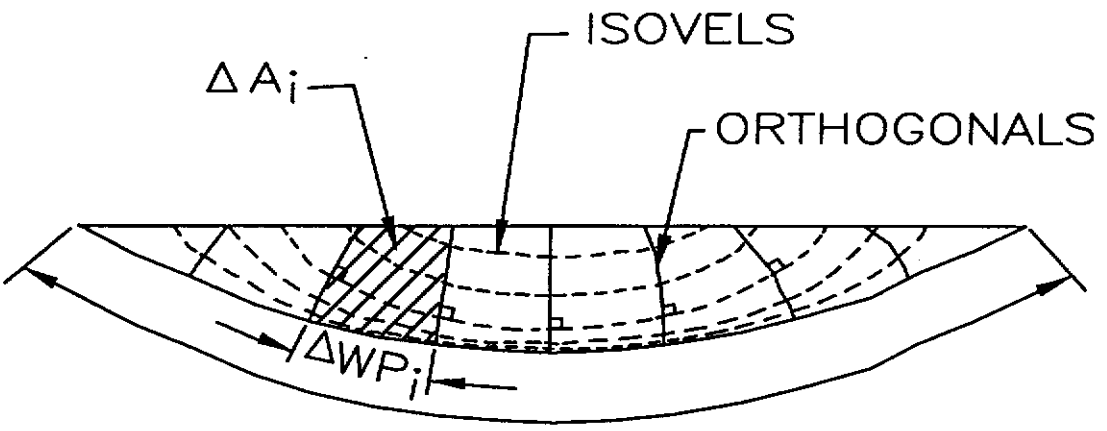

(a) Shear surfaces defined by orthogonals to isolines of velocity.

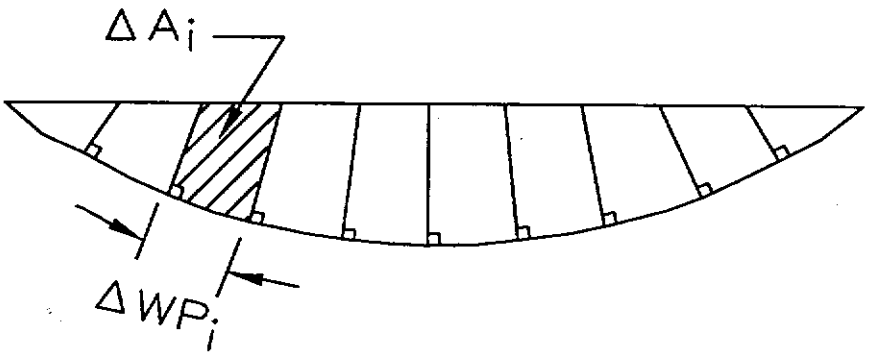

(b) Shear surfaces defined by orthogonals to channel boundary.

Figure 2.3. Channel boundary shear stress distribution calculations: (a) orthogonals to isovels (dashed lines) and (b) Lundgren and Jonsson method (Lundgren and Jonsson, 1964).

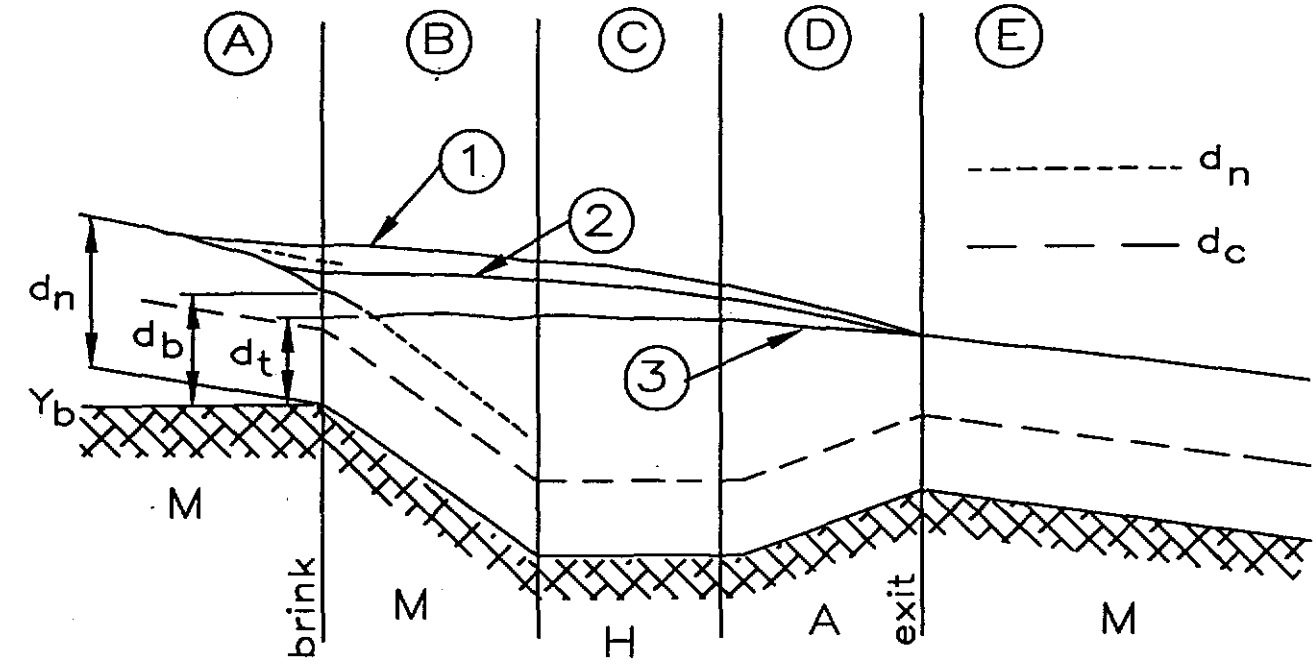

(a) Case I. submerged jet: $d_n > d_c$ on B.

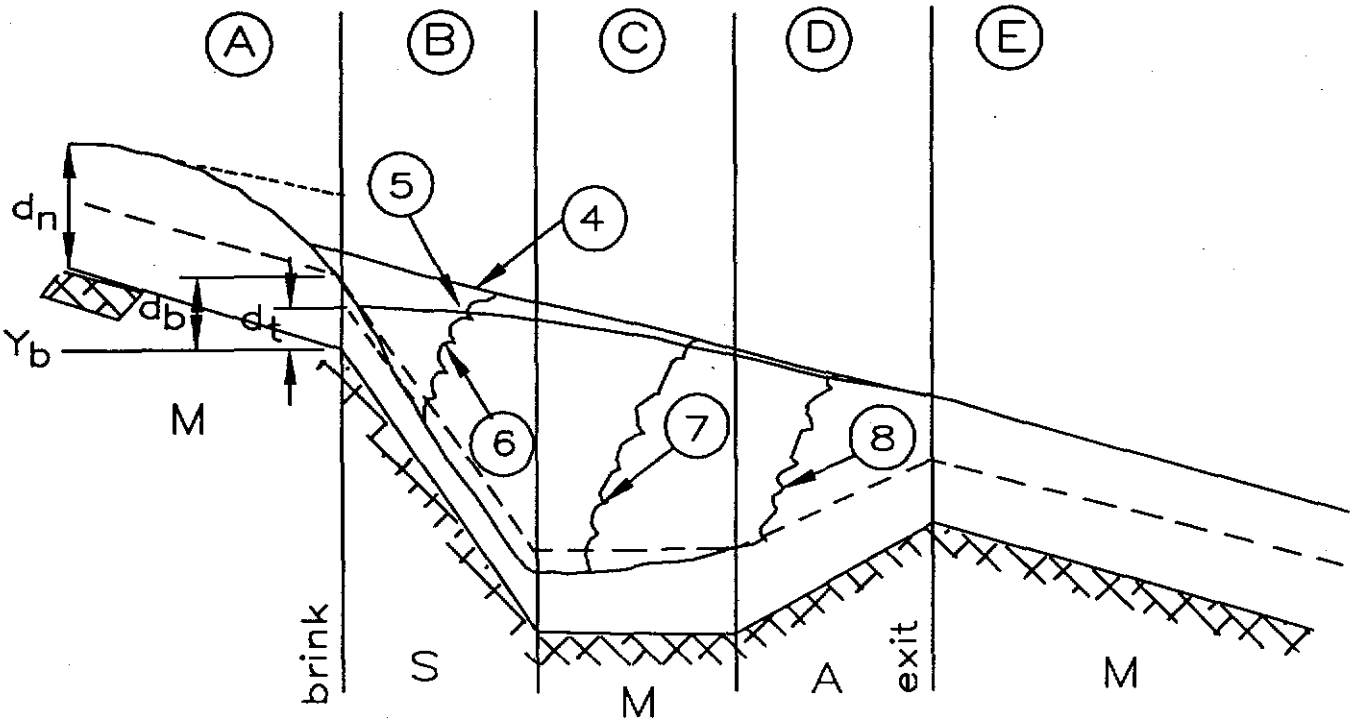

(b) Case II. submerged jet and jump: $d_n < d_c$ on B.

Figure 2.4. Illustration of possible flow profiles through the scour hole. The circled letters refer to channel segments, the numbers refer to possible flow profiles, and uncircled letters indicate slope class.

2.3.2.1. Free Jet

The free jet in the scour hole would be a special category of jets known as oblique impinging jets, as illustrated in Figure 2.5. The impinging jet has been divided into three zones (Beltaos and Rajaratnam, 1973). Zone 1 is the free jet zone. In this region, the jet is essentially uninfluenced by the presence of the wall. The rate at which the jet spreads and the velocity distribution are functions of inertial forces and distance, but not on Reynold's number. Zone II is known as the impingement zone. The spread of the jet and velocity profile in this zone are theoretically affected by inertial forces, geometry and viscous forces (Reynold's number), however, experimental data (Beltaos and Rajaratnam, 1973, Beltaos, 1976a) show that the effect of Reynold's number is nonsignificant. The point of maximum shear occurs at the transition from an impinging jet (Zone I) to a wall jet (Zone III). In Zone III is the wall jet region. In this zone, the streamlines diverge, as in a jet exiting along a wall. The primary forces are inertial and viscous, thus Reynold's number has an effect on shear and velocity distributions, although the influence has been shown to be weak (Beltaos and Rajaratnam, 1973).

The discussion will center first on perpendicular impinging jets, followed by oblique impinging jets.

2.3.2.1a. Free Jet Theory

The theory of free jets is utilized as a starting point for all jet theory. When a plane jet of thickness $2b_o$ with uniform velocity U_o, enters a stagnant infinite fluid, mixing begins to occur with the surrounding fluid, resulting in increasing jet thickness or width with increasing distance from the point of entry. For a steady flowing plane, turbulent, free jet, the pressure gradient is negligible and the equation of motion and continuity can be written:

$$u\frac{\partial u}{\partial z} + v\frac{\partial u}{\partial y} = \frac{-1}{\rho}\frac{\partial \tau_t}{\partial y} \tag{48}$$

and:

$$\frac{\partial u}{\partial z} + \frac{\partial v}{\partial y} = 0 \tag{49}$$

where u and v are the z and y components of velocity, z is the distance along the jet axis and y is the distance normal to the jet axis, τ_t is the turbulent fluid shear stress and ρ is density. Integrating the equations with respect to y, (Rajaratnam, 1976, 1983), one can obtain:

$$\int_{-\infty}^{\infty} \rho u^2 dy = 2b_o U_o^2 \tag{50}$$

where b_o is the half-width of the jet at entry and U_o is the inlet velocity. Equation (50) is essentially a statement of conservation of momentum, requiring knowledge of a velocity profile for evaluation. It has been widely shown that a similarity relationship for velocity holds for all z, giving:

$$\frac{u}{u_m} = f(\eta) \tag{51}$$

and in particular:

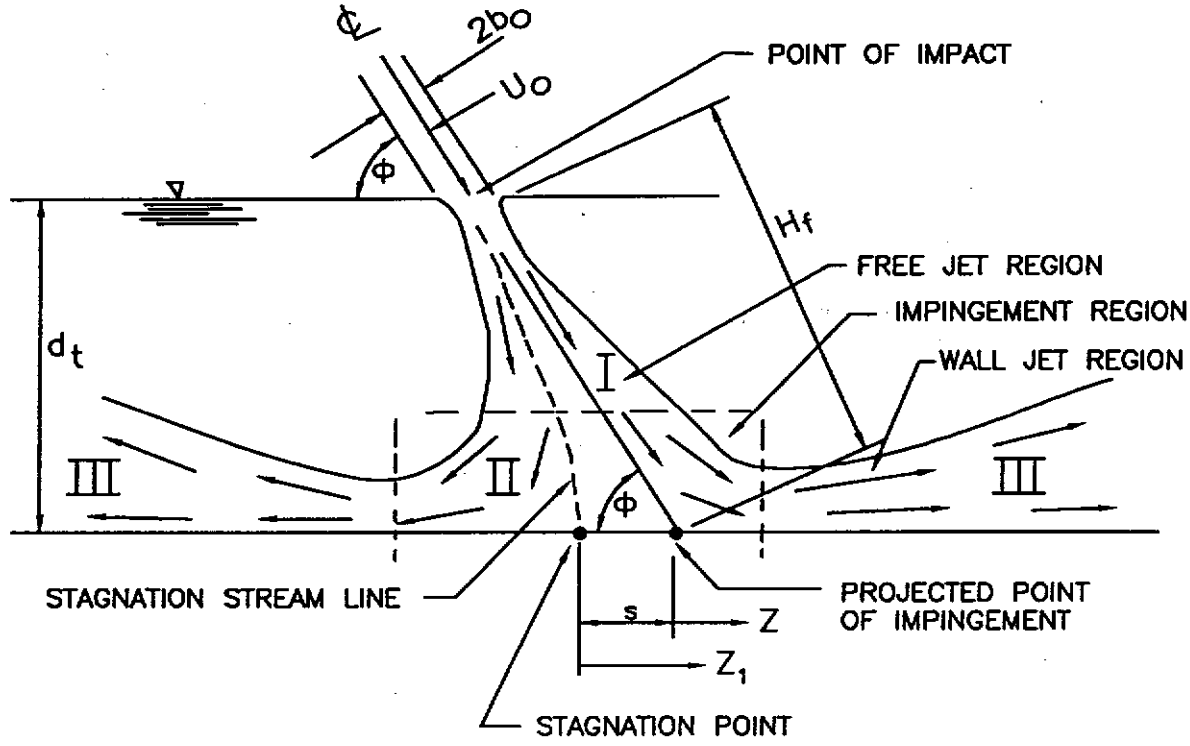

Figure 2.5. Definition sketch of an oblique impinging jet.

$$f(\eta) = e^{0.693\eta} \tag{52}$$

where u is velocity at any η, u_m is the max velocity for a cross section, η is a normalized distance given by:

$$\eta = \frac{y}{\lambda} \tag{53}$$

where y is the distance normal to the jet axis and λ is the value for y at which $u = u_m/2$. Using equation (53) in equation (50) and making the assumption that:

$$u_m = k_1 z^p \tag{54}$$

and

$$\lambda = k_2 z^q \tag{55}$$

it can be shown that:

$$u_m = \frac{k_1}{\sqrt{z}} \tag{56}$$

and

$$\lambda = \frac{k_2}{z} \tag{57}$$

Based on experimental data and theory, Rajaratnam (1982) showed that $k_2 = 0.087$ and $k_1 = 3.70\ U_o\sqrt{b_o/2}$, giving:

$$u_m = \frac{3.7\ U_o}{\sqrt{\frac{b_o z}{2}}} \tag{58}$$

$$\lambda = \frac{0.087}{z} \tag{59}$$

and

$$\frac{q}{q_o} = 0.44\sqrt{\frac{z}{b_o}} \tag{60}$$

where q is the total flow rate at any z (L^2T^{-1}) and q_o is the flow rate at z equal to zero. Entrainment causes the difference between q and q_o. From equations (57) and (58), it is clear that the spread of the jet is inversely proportional to distance and the max velocity decays proportional to the inverse square root of distance.

2.3.2.1b. Impinging Jet Theory

As the jet approaches a wall, back pressure begins to be significant and shear on the wall becomes an important external force. In this range, the pressure gradient becomes important and the equation of motion becomes (Beltaos and Rajaratnam, 1973):

$$u\frac{\partial u}{\partial z} + v\frac{\partial u}{\partial y} = \frac{-1}{\rho}\frac{\partial p}{\partial z} + \frac{1}{\rho}\frac{\partial \tau}{\partial y} \tag{61}$$

where p is the fluid pressure. A solution is needed for τ along the wall, where u and v are zero, and the vertical pressure gradient equals the horizontal shear gradient, hence:

$$\frac{\partial p}{\partial z} = \frac{\partial \tau}{\partial y} \tag{62}$$

or changing coordinates for perpendicular impinging jets:

$$\left.\frac{d\tau_o}{dz_1}\right|_{z=H} = \left.\frac{\partial p}{\partial z}\right|_{z=H} \tag{63}$$

where τ_o is the shear on the wall, z_1 is the distance along the wall, and H is the perpendicular distance from the water surface to the wall. Using empirically derived similarity profiles for pressure gradients, Beltaos and Rajaratnam showed that the following dimensionless equation could be developed:

$$\frac{U_*}{U_o}\sqrt{\frac{H}{2b_o}} = 0.17\left[erf\left(6.2\,\frac{z_1}{H}\right)\right]^{1/2} \tag{64}$$

where U_* is the shear velocity given by

$$U_* = \sqrt{\frac{\tau_o}{\rho}} \tag{65}$$

Thus, equation (64) is a prediction equation for shear. It should be noted that equation (64) is for normal impinging jets. Modifications are given in a later section for oblique jets.

2.3.2.1c. Wall Jet Theory

When a jet discharges along a boundary into a stagnant fluid, it is known as a wall jet. The equation of motion and continuity for a wall jet would be given by equations (48) and (49). Integrating equation (48) while utilizing (49), one obtains

$$\frac{d}{dz}\int_o^\infty \rho u^2 dy = -\tau_o \tag{66}$$

Using a new similarity relationship:

$$\frac{u}{u_m} = 1.48\eta^{1/7}\,[\,1 - erf\,(0.68\eta)\,] \tag{67}$$

and experimental data, Rajaratnam (1983) showed that for any z:

$$\frac{u_m}{U_o} = \frac{3.5}{\sqrt{\frac{z}{b_o}}} \tag{68}$$

and

$$\tau_o = C_f\,\rho\frac{U_o^2}{2} \tag{69}$$

where

$$C_f = \frac{0.2}{\left(\frac{z}{b_o}\right)\left(\frac{U_o\,b_o}{\nu}\right)^{1/12}} \tag{70}$$

Thus, the shear distribution is a weak function of Reynold's number. A change in Reynold's number by an order of magnitude would change C_f by a factor of 1.8.

A problem with the use of the impinging jet theory in combination with the wall jet to estimate shear stress in both zones II and III is that the predicted shears do not agree at z_1/H = 0.35, the point of transition from impinging jet to wall jet. Also, the theories do not account for impingement angles other than 90°. Therefore, Beltaos (1976a) resorted to empirical equations to predict shear and velocities for both zones II and III, as described below.

2.3.2.1d. Oblique Impinging Jets

Beltaos (1976a) conducted an extensive study of oblique impinging jets, using air as the fluid, over a range of impingement angles from 20° to 90°. For an oblique jet, the stagnation point is displaced a distance 's' from the jet centerline projection (see Figure 2.5). Based on potential jet theory and experimental data Beltaos (1976a) showed that:

$$\frac{s}{H_f} = \frac{2.15\left(1 - \frac{\phi}{90}\right)}{8\,\sin\phi} \tag{71}$$

where s is the stagnation displacement, ϕ is the angle of impingement as shown in Figure 2.5, and H_f is the flow path length through the water. Shear stress in the impingement zone was calculated as a function of the distance z_1 from the stagnation point by:

$$\frac{\tau_o}{\tau_{om}} = erf\,(0.833\ \eta) - C_1\ \eta\ g\ (\eta) \tag{72}$$

where τ_o is the shear stress at any z_1, τ_{om} is the maximum shear stress, and η is a dimensionless distance given by

$$\eta = \frac{z_1}{\xi} \tag{73}$$

and

$$g(\eta) = e^{-.693\eta^2} \tag{74}$$

C_1 is a constant approximately equal to 0.2, and ξ is a scaling parameter which depends weakly on ϕ. Beltaos presented experimental data relating ϕ and ξ. Using a piecewise linear fit to Beltaos data for ξ vs ϕ, the following equations were developed:

$$\frac{\xi}{H_f} = .1333 - \left(\frac{\phi}{130}\right)(.0166); \qquad 0° \le \phi \le 130° \tag{75}$$

$$\frac{\xi}{H_f} = .1167 - (.05)\left(1 - \frac{180 - \phi}{50}\right); \qquad 130° < \phi \le 180° \tag{76}$$

The maximum shear stress, which occurs at $\eta = 2.5$, is given by Beltaos as:

$$\frac{\tau_{om}\ H_f}{\rho\ U_o^2\ b_o} = C_*(\phi) \tag{77}$$

where $C_*(\phi)$ is given by:

$$C_*(\phi) = .058 \qquad 0° \le \phi \le 90° \tag{78}$$

$$C_*(\phi) = .058 - 0.42\left(1 - \frac{180 - \phi}{90}\right); \qquad 90° < \phi \le 180° \tag{79}$$

Shear stress does not depend on Reynold's number for the impingement zone.

For η greater than 2.5, the flow is a wall jet. For this region, Beltaos (1976a) proposed that shear be calculated from the maximum velocity as a function of z, $(z_1 - s)$, or

$$\tau_o = C_f \rho \frac{u_m^2}{2} \tag{80}$$

where C_f is a drag coefficient given as a function of Reynold's number by:

$$C_f = 0.0474 R_o^{-1/5} \tag{81}$$

where:

$$R_o = \frac{2U_o b_o}{\nu} \tag{82}$$

and ν is kinematic viscosity. The maximum velocity is given by:

$$\frac{u_m}{U_o} = \frac{C_u(\phi)}{\sqrt{\frac{z}{2b_o}}} \tag{83}$$

where $C_u(\phi)$ is given by:

$$C_u(\phi) = \sqrt{5.5 (1 + \cos \phi)} \tag{84}$$

Combining equations (77) through (84) yields:

$$\frac{\tau_o}{\tau_{om}} = .0474 R_o^{-1/5} \frac{C_u^2(\phi)}{C_*(\phi)} \left(\frac{H_f}{z}\right) \tag{85}$$

This is similar in form to a relationship proposed by Hansen et al. (1990) for a circular impinging jet.

Other researches have utilized the concept of an impinging jet to estimate scour hole development (Poreh and Hefez, 1967; Rajaratnam, 1981). The scour hole profiles have similar shapes. Most investigators predict the maximum scour hole depth and use it as a characteristic length. Stein (1990) predicted the change in scour hole depth based on an equation similar to equation (77). The shape of the scour hole was empirically determined, based on the maximum scour hole depth. In CHANNEL, the Beltaos equation is used for shear distribution with the free jet. It is recognized that some problems exist with the use of these relationships, i.e.:

- The equations of Beltaos (1976a) were developed for rigid impervious boundaries. It would be desirable to have modifications based on experimental data, but none is available.

- The equations were developed for impinging jets on flat plates. Impinging jets in a scour hole will have streamlines with greater curvature than those on a flat plate. It would be desirable to have data addressing this issue, but none are available.

2.3.2.2. Submerged Jet

If the tailwater lies above the brink depth, but below critical depth at the brink, the jet is assumed to be submerged (see Figure 2.6). Bormann and Julian (1991) evaluated scour in submerged jets downstream of grade control structures, and found that the angle of the centerline of the jet was given by:

$$\beta = .316 \sin\alpha + 0.15 \ln\left(\frac{D_p + y_o}{y_o}\right) + 0.13 \ln\left(\frac{d_t}{y_o}\right) - 0.05 \ln\left(\frac{U_o}{\sqrt{gy_o}}\right) \quad (86)$$

where α is the inclination angle of the upstream face of the scour hole, y_o is the thickness of the submerged jet, d_t is the tailwater depth and D_p is the change in elevation through the scour hole. Bormann and Julian (1991) used the depth from the brink to the original grade line for D_p. In this application, D_p will take into account the average scour hole depth.

In CHANNEL shear distribution computation for a submerged jet will utilize the following concepts:

1. If $(\beta - \alpha) \geq \delta_c$, then the initial jet depth is y_o and the initial velocity is U_o. Computation will be made with the full impinging jet equations (71-85). δ_c is a user defined limit.

2. If $(\beta - \alpha) < \delta_c$, then calculations will be made assuming a wall jet, using equations (69) and (70).

2.3.2.3. Hydraulic Jump

Shear distribution models for hydraulic jumps are lacking. In CHANNEL, shear distribution calculations for jumps will utilize the same concepts as for submerged jet calculations. The thickness of the jet will be the upstream depth of flow immediately above the jump and the velocity given by the average cross sectional velocity upstream of the jump as shown in Figure 2.7.

2.4. SEDIMENT DETACHMENT, TRANSPORT, AND DEPOSITION INTERACTIONS

Detachment and scour in a channel are related to flow variables, soil variables, and transport capacity. Two levels of discussion of detachment and deposition are needed. At one level, there is the interaction between detachment, transport and deposition that is being considered on an average over the entire channel. This can be thought of as the macro approach. On another level are the micro-scale details associated with translating shear profiles into a quantity of detached sediment and ultimately to a modified boundary. The macro-scale concepts are discussed in this section and the microscale details in the next chapter which details the model algorithms.

2.4.1. Basic Models of Detachment and Transport

An overview of the state of the art in fundamental erosion modeling is given by Storm et al. (1990). The following discussion is excerpted from that document.

2.4.1.1. Sediment Continuity Equation

The relationship which is primary for fundamental erosion processes is continuity of mass.

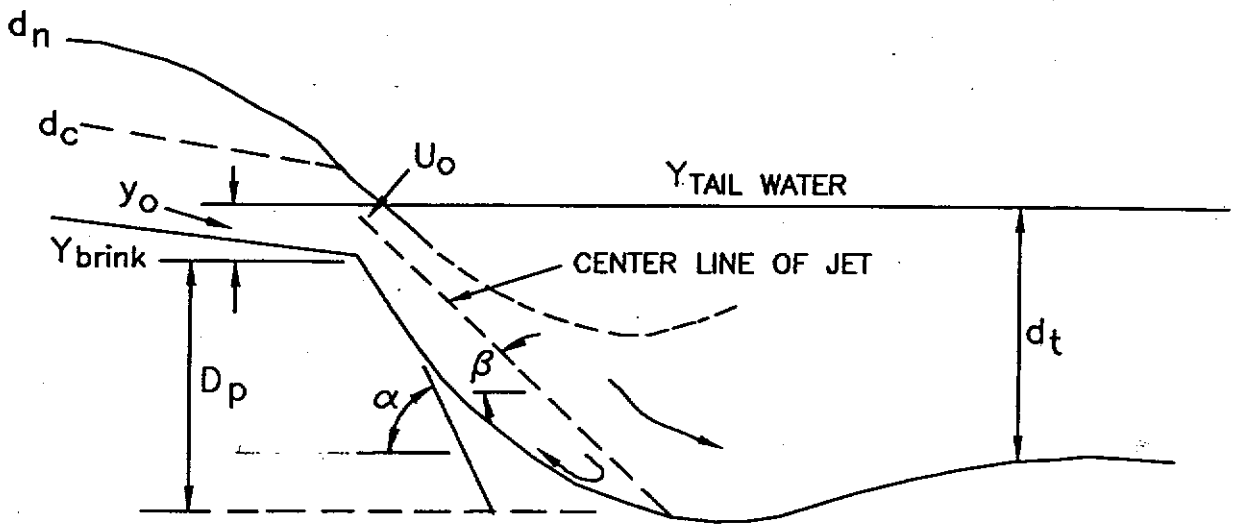

Figure 2.6. Schematic of a submerged jet.

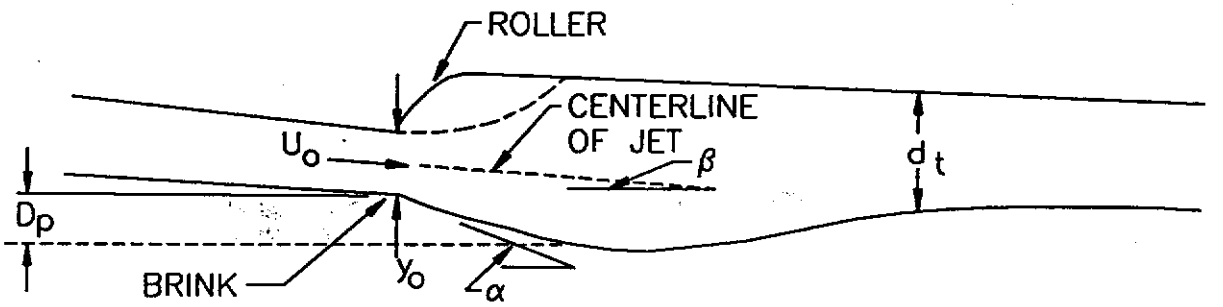

Figure 2.7. Schematic of an hydraulic jump.

For overland flow, the continuity equation is (Foster, 1982):

$$\frac{\partial q_s}{\partial z} + \rho_s \frac{\partial (cy)}{\partial t} = D_r + D_L \tag{87}$$

where q_s is sediment load, z is distance down slope, ρ_s is mass density of sediment particles, c is sediment concentration, y is flow depth, t is time, D_r is actual detachment rate, and D_L is the sediment inflow rate from lateral inflow. The erosion parameters q_s and D_r are measured per unit width of the channel. The $\partial q_s/\partial z$ term represents the change in sediment flow rate along the slope, and $\rho_s \partial(cy)/\partial t$ represents the change in sediment storage over time.

For flows that are shallow and gradually varied, the $\rho_s \partial(cy)/\partial t$ storage term may be neglected, resulting in a widely used steady state equation:

$$\frac{\partial q_s}{\partial z} = D_r + D_L \tag{88}$$

where D_r is the detachment or deposition rate in the channel.

2.4.1.2. Interaction Between Sediment Load and Deposition Rate in the Channel

As discussed earlier, the potential detachment rate is estimated as a function of shear excess (Foster, 1982) or:

$$D_{rc} = K(\tau - \tau_c) \tag{1}$$

where K is an erodibility constant, τ is shear on the channel boundary and τ_c is critical tractive force. The actual detachment can be much less than the potential detachment rate as a result of an interaction between sediment load, transport capacity, and detachment.

The interactions between sediment load and transport capacity are neglected in equations (87) and (88). Foster and Meyer (1972a, 1975) proposed that channel detachment and deposition are proportional to the difference between transport capacity and sediment load, or:

$$D_r = C_1 (T_c - q_s) \tag{89}$$

where C_1 is a first-order reaction coefficient (L^{-1}), and T_c is the sediment transport capacity. If it is assumed that the maximum detachment capacity, D_{rc}, is proportional the transport capacity, i.e.:

$$D_{rc} = C_1 T_c \tag{90}$$

then a relationship can be developed defining the interaction between sediment load and transport capacity, or (Foster and Meyer, 1972a):

$$\frac{D_r}{D_{rc}} + \frac{q_s}{T_c} = 1 \tag{91}$$

or

$$D_r = D_{rc}\left(1 - \frac{q_s}{T_c}\right) \tag{92}$$

From equations (91) and (92) it can be seen that detachment equals detachment rate capacity when the sediment load equals zero. Conversely, when sediment load approaches transport capacity, D_r approaches zero.

Foster and Meyer (1972a) utilized the stream power concept to lend credence to these concepts, claiming that the finite amount of energy in a specified flow may be used for either detaching or transporting sediment particles, but the same energy cannot be used for both. The D_r/D_{rc} term in equations (91) and (92) represents the relative amount of energy expended on sediment transport. The sum of these two equal unity, the total relative available energy.

These concepts may also be applied to deposition. During deposition, C_1 varies with sediment size, and to date there are no validated relationships describing this phenomena. Based on results by Einstein (1968), Foster (1982) proposed that C_1 be given by

$$C_1 = \frac{V_s}{q} \tag{93}$$

where V_s is settling velocity and q is flow discharge per unit width of channel for channelized flow.

The interrelationships between detachment, sediment load and transport capacity as computed in CHANNEL are defined by equations (1) and (88) - (93). Solutions to the equations must be developed numerically, except for a few idealized steady state conditions (Foster and Meyer, 1972a, 1975).

2.4.1.3. Transport Capacity Models

Most sediment transport models were developed for large streams, but have been widely used for small channels. However, major differences exist between the hydraulics of shallow flows in upland areas and deeper channel flow (Foster and Meyer, 1972b). Current transport models were developed using a limited range of sediments and flow conditions but have worked remarkably well given that background. In addition, limited transport studies have been performed on aggregates and fine particles, which are typically encountered in agricultural watersheds.

Transported sediment is typically classified as wash load, suspended load, bed load, and total load. Wash load is considered to be made up of particles finer than the bulk of the bed material and rarely settle to the channel bottom (Graf, 1971). Bed load is composed of sediment particles moving along the channel bottom by saltation, rolling, or sliding. Suspended load is bed load size sediment that is transported in complete suspension for an appreciable length of time. In contrast to bed load, suspended load is much more uniformly distributed throughout the flow depth. When a decrease in transport capacity occurs, the suspended load is not immediately deposited on the channel bottom due to the relatively small particle fall velocities.

Empiricism is inherent in all existing transport models, therefore some degree of calibration is always necessary. The selection of an appropriate transport model for a specific application is difficult at best. Currently, the most common transport models used for small channels are the bed load model of Yalin (1963), and the unit stream power concept developed by Yang (1973) for total load. Some other commonly applied total load formulas are given by Ackers and White (1973) and Laursen (1958); and bed load formulas by Meyer-Peter and Muller (1948) and Einstein (1950). Numerous other models are available as well, as summarized in Graf (1971), Simons and Senturk (1977), and Alonso et al. (1981). Alonso et al. give a comparison of the accuracy of the models.

2.4.1.3a. Yalin Bed Load Model: Uniform Particle Size

Yalin's (1963) bed load transport model was developed for cohesionless grains over a fluvial bed. In the model development dimensional analysis was used with the mechanics of average grain motion in a uniform turbulent flow field with a laminar sub-layer not exceeding the bed roughness. The model is widely used outside these constraints. The model is presented as a series of equations or (Yalin, 1977):

$$\phi = \frac{q_s\sqrt{\rho_w}}{(\gamma_s d)^{3/2}} = 0.635sY^{1/2}\left[1 - \frac{1}{as}\ln(1 + as)\right] \tag{94}$$

$$a = 2.45Y_{cr}^{1/2}S_g^{-0.4} \tag{95}$$

$$Y = \frac{\rho_w U_*^2}{\gamma_s d} \tag{96}$$

$$s = \frac{Y}{Y_{cr}} - 1 \tag{97}$$

where ϕ is a dimensionless transport rate number (originally defined by Einstein), q_s is sediment transport rate, ρ_s is the particle specific weight in water, d is mean particle diameter, Y is a mobility number, Y_{cr} is the critical mobility number found from Shields (1936) diagram, S_g is sediment specific gravity, and U_* is bed shear velocity. The Yalin equation can also be written as a concentration by defining a sediment concentration, C(ppm) as (Alonso et al., 1981):

$$C = \frac{10^6 q_s}{\gamma_w V h} \tag{98}$$

where V is average velocity (m/s) and h is flow depth (m). Substituting into equation (94) and re-arranging

$$C = 6.35x10^5\frac{S_g d U_*}{Vh}\, s\left[1 - \frac{1}{as}(1 + as)\right] \tag{99}$$

Since the Yalin equation accounts for the transport of uniform grain size, Foster (1982) developed a methodology to predict the transport of individual particle size classes for a particle size distribution. Details are presented in the following section.

2.4.1.3b. Transport Capacity: Variable Particle Size

Most current sediment transport theory was developed for stream flow conditions. However, Alonso et al. (1981) found that the Yalin (1977) equation was appropriate to use on the transport of light materials in stream flow, and a range of particle sizes and densities in shallow flow typically encountered in field conditions. Therefore, the Yalin transport equation was selected in CHANNEL to evaluate the transport capacity of open channel flow based on the evaluation by

Alonso et al. (1981) and its current widespread use. Yalin's (1977) model was presented earlier as equations (94) - (97).

Redefining several terms, Finkner et al. (1989) presented the Yalin equation as:

$$\phi = \frac{T_c}{S_g d\sqrt{\rho_w \tau}} = 0.635\ \delta \left[1 - \frac{1}{\beta} \ln (1 + \beta)\right] \tag{100}$$

$$\beta = 2.45\ S_g^{-0.4}\ Y_{cr}^{1/2} \delta \tag{101}$$

$$\delta = \frac{Y}{Y_{cr}} - 1 \tag{102}$$

$$Y = \frac{\tau}{\rho_w (S_g - 1) g\ d} \tag{103}$$

where T_c is sediment transport capacity (kg/s/m channel width), τ is shear stress acting to detached soil (Pa) and δ and β are dimensionless parameters.

The Yalin equation was developed for uniform particle size. To predict transport capacity for a sediment mixture, Foster and Meyer (1972b) modified the Yalin equation by distributing the flow's total transport capacity among the available sediment based on flow characteristics, and particle size and density. The Yalin equation (Yalin, 1963) was developed by assuming the number of particles in transport was proportional to δ. Hence, Foster and Meyer (1972b) assumed for a sediment mixture that the number of particles of type i were proportional to δ_i. The total δ for the sediment mixture, T, was found by summing all δ_i's, such that:

$$T = \sum_{i=1}^{n} \delta_i \tag{104}$$

where n is the number of particle types. For sediment particles of type i in a mixture, the number of transport particles $[Ne]_i$, is:

$$[Ne]_i = N_i \frac{\delta_i}{T} \tag{105}$$

where N_i is the total number of particles of uniform material i.

The dimensionless transport rate ϕ was assumed proportional to the number of transported particles, such that:

$$[\phi_e]_i = \phi_i \frac{\delta_i}{T} \tag{106}$$

where $[\phi_e]_i$ is the effective mass for particle type i in the mixture and ϕ_i is the ϕ evaluated for particle type i with uniform material. The potential transport capacity for particle type i in a mixture, T_{cpi}, was defined as:

$$T_{cpi} = [\phi_c]_i \, S_{gi} \, d_i \sqrt{\rho_w \, \tau} \tag{107}$$

The transport capacity of each particle class was assumed to be represented by equation (104) only if available sediment in all particles was in excess or deficit.

When there was excess transport capacity in a particle class and a deficit in another, the transport capacity was shifted in order to use all existing transport capacity. For these cases, Davis (1978) developed a methodology for redistributing the transport capacity using the following steps.

1. When the sediment load for particle class i, q_{si}, was less than or equal to T_{cpi}, ($q_{si} \leq T_{cpi}$), the required transport ϕ_{ri} by the available sediment was found using equation (100), such that:

$$\phi_{ri} = \frac{q_{si}}{S_{gi} \, d_i \sqrt{\rho_w \tau}} \tag{108}$$

Thus, the actual transport capacity for particle class i, T_{ci}, was:

$$T_{ci} = q_{si} \tag{109}$$

2. For all particle classes where $q_{si} \leq T_{cpi}$, the fraction of total transport capacity actually needed, SPT, was found using:

$$SPT = \sum_{i=1}^{n-n_{xc}} \frac{\phi_{ri}}{\phi_i} \tag{110}$$

where n_{xc} was the number of particle classes where $q_{si} > T_{cpi}$.

3. The excess sediment transport fraction, E_{xc}, that was distributed among the transport deficit classes is:

$$E_{xc} = 1 - SPT \tag{111}$$

4. For the transport deficit particle classes where $q_{si} > T_{cpi}$, the sum of the δ_i's were calculated as:

$$SDLT = \sum_{i=1}^{n_{xc}} \delta_i \tag{112}$$

5. The excess transport capacity was distributed among the n_{xc} particle classes for $q_{si} > T_{cpi}$ in proportion to their individual δ_i, such that

$$T_{ci} = \frac{\delta_i}{SDLT} E_{xc} \, \phi_i \, S_{gi} \, d_i \sqrt{\rho_w \tau} \tag{113}$$

6. If after repeating steps 1-5 all n particle classes had $q_{si} > T_{ci}$, it was assumed that the proper transport capacities were found.

7. If after repeating steps 1-5 all n_{xc} particle classes had $q_{si} < T_{ci}$, the excess transport capacity was equally redistributed among all n particles classes by:

$$SMUS = \sum_{i=1}^{n} \frac{\phi_{ri}}{\phi_i} \tag{114}$$

$$T_{ci} = \frac{q_{si}}{SMUS} \tag{115}$$

2.5. CHANNEL GEOMETRY

Channels, especially those developing in upland watersheds, are sinuous and irregular in cross section. Overall channel shape has a significant impact on the erosion and/or deposition taking place within the channel. For example, consider a channel with constant flow rate and soil properties. In a certain reach where the slope is steeper than average, the channel may be eroding quite rapidly. However, a pool may have formed a few yards downstream, where deposition is occurring. If a headwall has formed in the channel, the bottom of the scour hole may be eroding, but just downstream a delta may be forming with sediment scoured from the scour hole. All other things being constant, the channel shape is what is dictating the erosion\deposition processes that occur within a given reach.

To effectively model channel erosion processes, especially the processes of headwall development and propagation, a three dimensional model of channel geometry is required. Most channel erosion models that have been developed in the past are one or, at best, two-dimensional in scope. This presents some interesting challenges to the modeler of headwall erosion in that these dimensional limitations must be overcome. The goal in developing the channel model was to use existing one and two-dimensional models and apply them to a three-dimensional channel. The following discussion presents how real, three-dimensional channels are represented in CHANNEL.

In CHANNEL the basis for channel representation is the cross section. Cross section shape is effectively represented by a series of line segments connected by nodes as shown in Figure 2.8. The coordinate system used in CHANNEL is shown in Figure 2.9. Each node is assigned an x and y coordinate. The lowest node, the node with the smallest y coordinate, is also assigned a z coordinate. By linking the lowest node in each cross section as shown in Figure 2.9, the channel shape can be adequately represented. This type of representation allows modifications to the channel shape to be accomplished effectively.

For purposes of clarity, the linkage of the lowest node in each of the cross sections is termed the profile of the channel. The profile is basically the representation of the channel bottom. The channel slope is determined from the channel profile representation. The channel shape at any point along the channel is represented by the cross section.

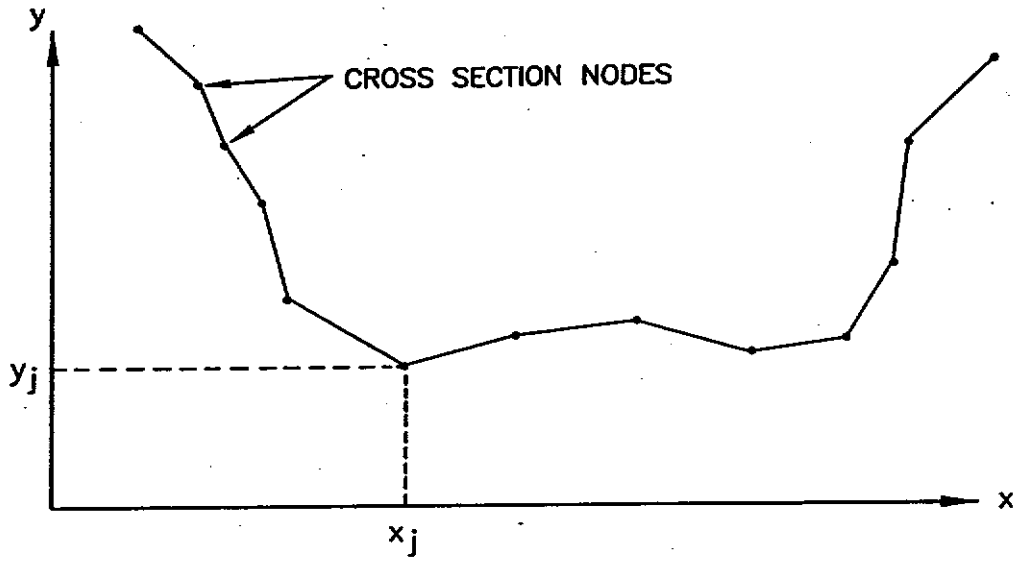

Figure 2.8. Schematic of cross section representation used in CHANNEL.

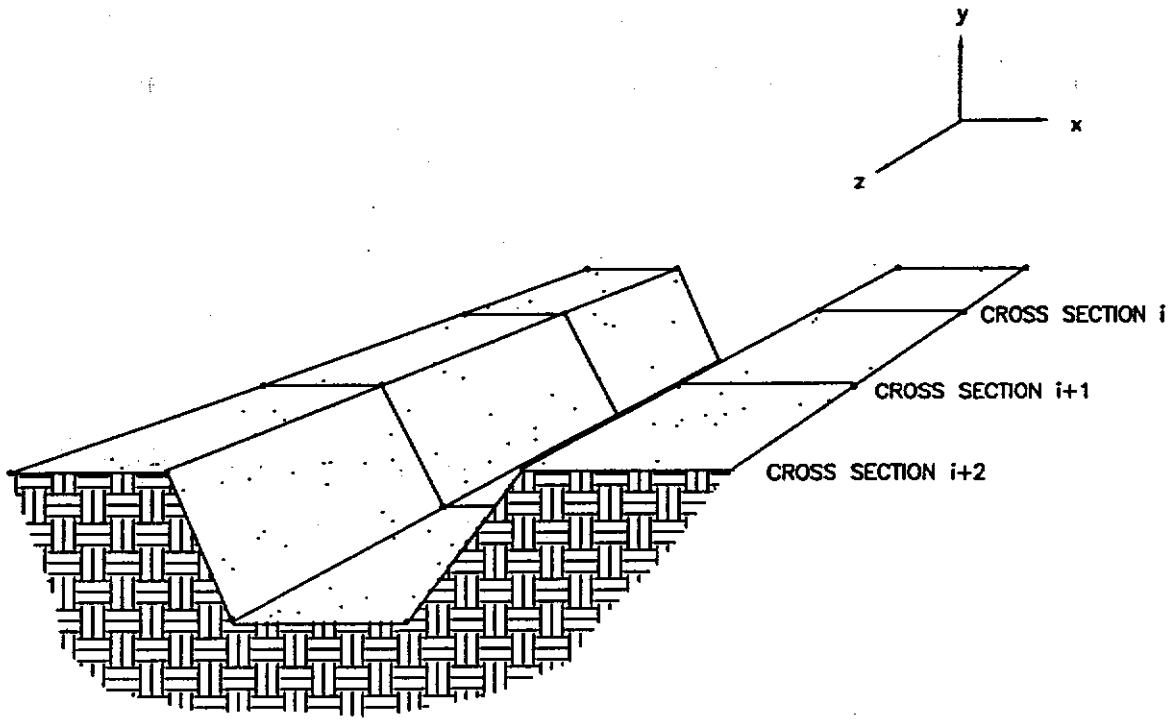

Figure 2.9. Schematic showing overall channel representation using linked cross sections.

CHAPTER 3

MODEL DESCRIPTION

The following is a discussion of the application of the models and equations presented in the previous chapter to the physical channel. The methods and algorithms used to construct the CHANNEL model are presented. The discussion will follow the flow chart of CHANNEL given in Figure 3.1. The discussion is not meant to be a user's manual for the model.

3.1. USER INPUT

3.1.1 Initial Channel Geometry

CHANNEL requires an initial channel geometry or shape before computations can begin. The model recognizes that natural channels can be broken into parts called reaches as shown in Figure 3.2. A reach is defined as a section of channel upon which either gradually varied flow or rapidly varied flow is occurring. Rapidly varied flow reaches are labeled scour holes and gradually varied flow reaches are termed GVFRs.

Reaches just upslope and downslope of scour holes must be GVFRs. However, a GVFR may consist of only one cross section within the model framework. This is illustrated in Figure 3.3a. If the channel shape changes such that scour hole 2 in Figure 3.3a moves upslope into scour hole 1, GVFR 2 is assimilated into one of the scour holes and scour hole 2 is assimilated into scour hole 1. This is illustrated in Figure 3.3b.

A channel may also consist of a series of GVFRs with no scour holes. The only constraint is that rapidly varied flow cannot occur on a GVFR because CHANNEL does not check for rapidly varied flow on GVFRs at input. The model does check for changing geometry and flow conditions in subsequent time steps. Also, all GVFRs, except the first, must have mild slopes. Only the first GVFR is allowed to be steep or greater than critical. Adverse and horizontal slopes are allowed only in scour holes.

Channel geometry is input to the model in the following steps:

(1) Input the initial number of gradually varied flow reaches (GVFR) and scour holes if any.

(2) For each GVFR and scour hole, input the number of cross sections within the reach or scour hole.

(3) For each cross section, input the profile direction coordinate (z coordinate; refer to Figure 2.9). The last cross section in a given reach and the first cross section of the subsequent downstream reach have the same z coordinate and cross-sectional shape.

(4) For each cross section, input the number of line segments used to represent the cross section shape. Each segment is connected to another segment by a node. For n segments, there are n+1 nodes.

(5) For each node within a cross section, input the x and y coordinates of the node (see Figure 2.8).

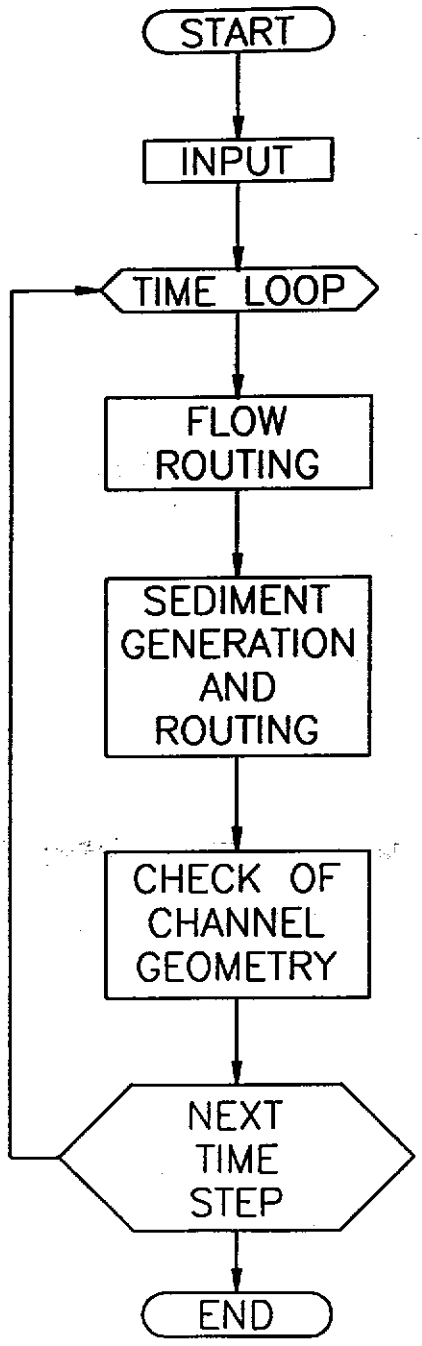

Figure 3.1. CHANNEL flowchart.

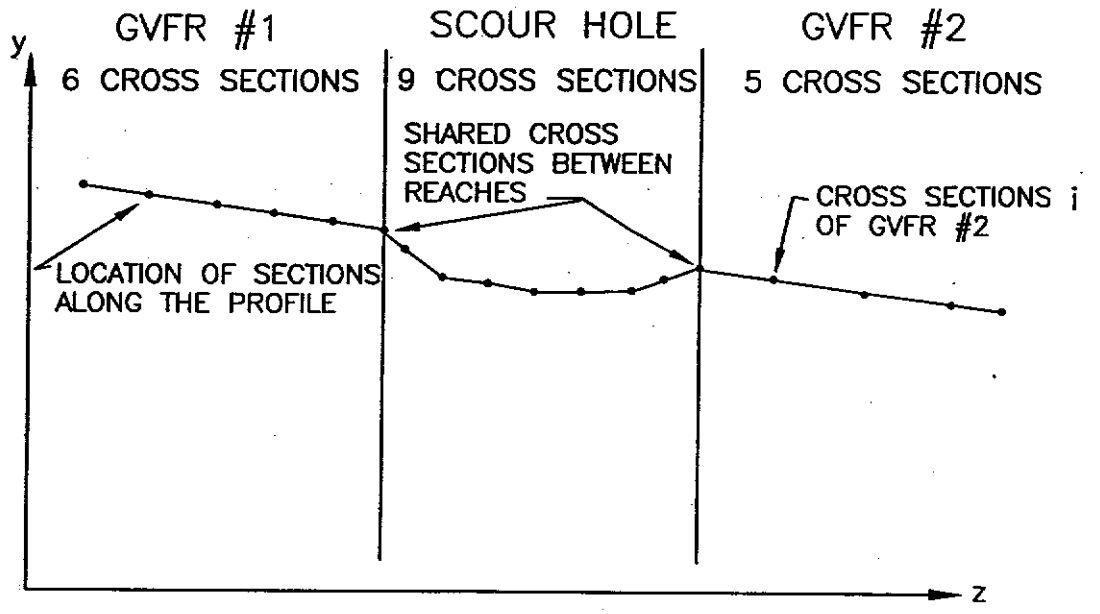

Figure 3.2. CHANNEL representation of channel profile.

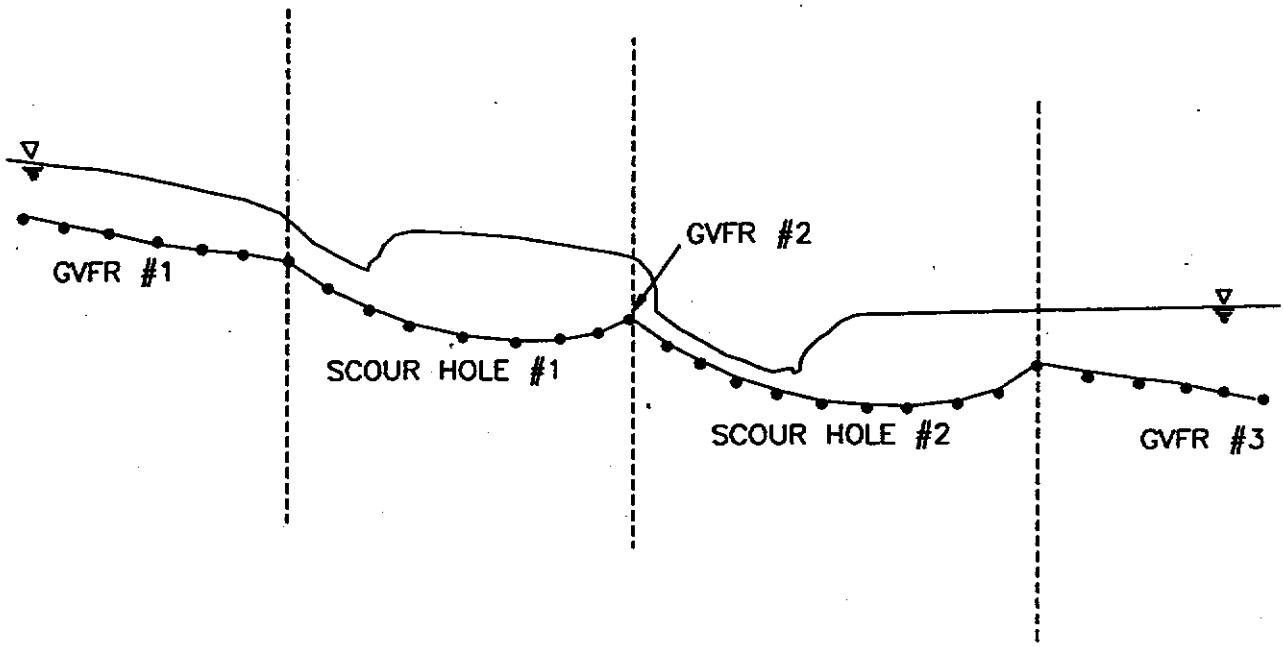

(a) Channel with one node GVFR between two scour holes.

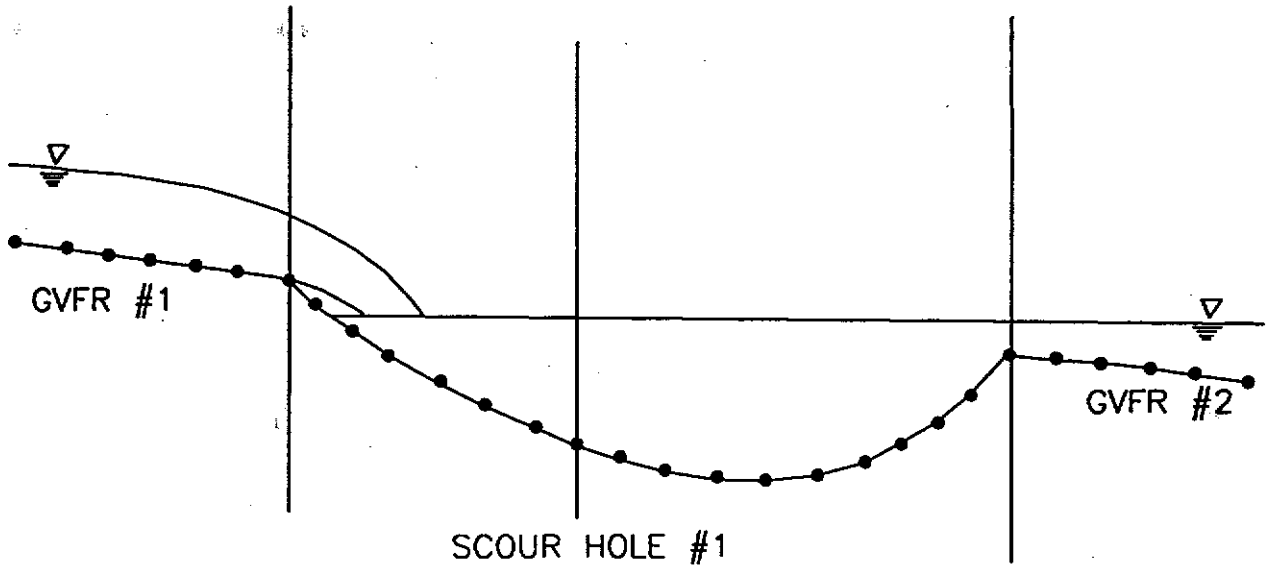

(b) New channel profile after scour hole migration.

Figure 3.3. Typical channel profiles showing the relationship between GVFRs and scour holes.

3.1.2. Channel Properties

Channel properties that are input to the model are:

- soil particle size distribution
- soil particle specific gravity in each size class
- soil critical shear
- soil erodibility
- soil bulk density
- manning's n

A single particle size distribution is used for matrix material and mannings's n can vary from cross section to cross section. Also, the model allows for variation of critical shear (τ_c), erodibility (K), and bulk density (ρ_b), along the cross section perimeter and down through the soil profile. This is illustrated by Figure 3.4. At each node of the cross section a value for τ_c, K, and ρ_b is input. If the soil parameters vary downward through the soil profile, the model requires the number of layers, or lifts (see Figure 3.4), and the y coordinate of the top of each lift, and the values of τ_c, K, and ρ_b for each lift. The last lift is assumed to extend downward indefinitely. This is done for each cross section in the channel. This method of soil representation allows for variation of the lift elevations along the channel profile as illustrated in Figure 3.5.

In addition, the model allows for some property variation in the x direction. This is illustrated in Figure 3.4 by the lines labeled x_L and x_R. To the left of x_L and to the right of x_R values for critical shear, erodibility, and bulk density are input. If a cross section node moves outside of x_L or x_R, the soil parameters for that node are set to the values input for the material outside of x_L and x_R. This allows for the modeling of flume walls or other structures if desired.

As the cross section boundary reaches a new lift or vertical boundary, τ_c, K, and ρ_b are reset to the lift or boundary values at nodes in the cross section that have crossed into the lift or boundary. This is illustrated in Figure 3.6. Movement of cross section nodes is discussed in more detail in section 3.6.

3.1.3. Inflow Hydrograph and Sedimentgraph and Lateral Inflow Hydrographs and Sedimentgraphs

Input of the hydrographs and sedimentgraphs requires as few as three hydrograph and sedimentgraph points taken at constant time intervals. Required are the number of data points, the hydrograph or sedimentgraph values, and the time increment between data points. The sedimentgraph values must also be partitioned according to particle size classes. The sedimentgraph size classes must correspond with the soil particle size classes.

For lateral inflow, a hydrograph and sedimentgraph, as input above, is required for each cross section along the channel. Lateral inflow is optional.

The time increment at which the hydrograph and sedimentgraph values are taken is arbitrary. CHANNEL linearly interpolates between input data points to generate the hydrographs and sedimentgraphs consistent with the time step being used by the model. The flow rate at each cross section is the running sum of the channel inflow and lateral inflow at each section.

3.1.4. Flow Control Depths

The model allows the user to input the downstream control depth, or choose for the model to calculate critical depth or normal depth as the downstream control depth. If the first GVFR is steep, an upstream control depth is input or determined in the same manner as the downstream control depth.

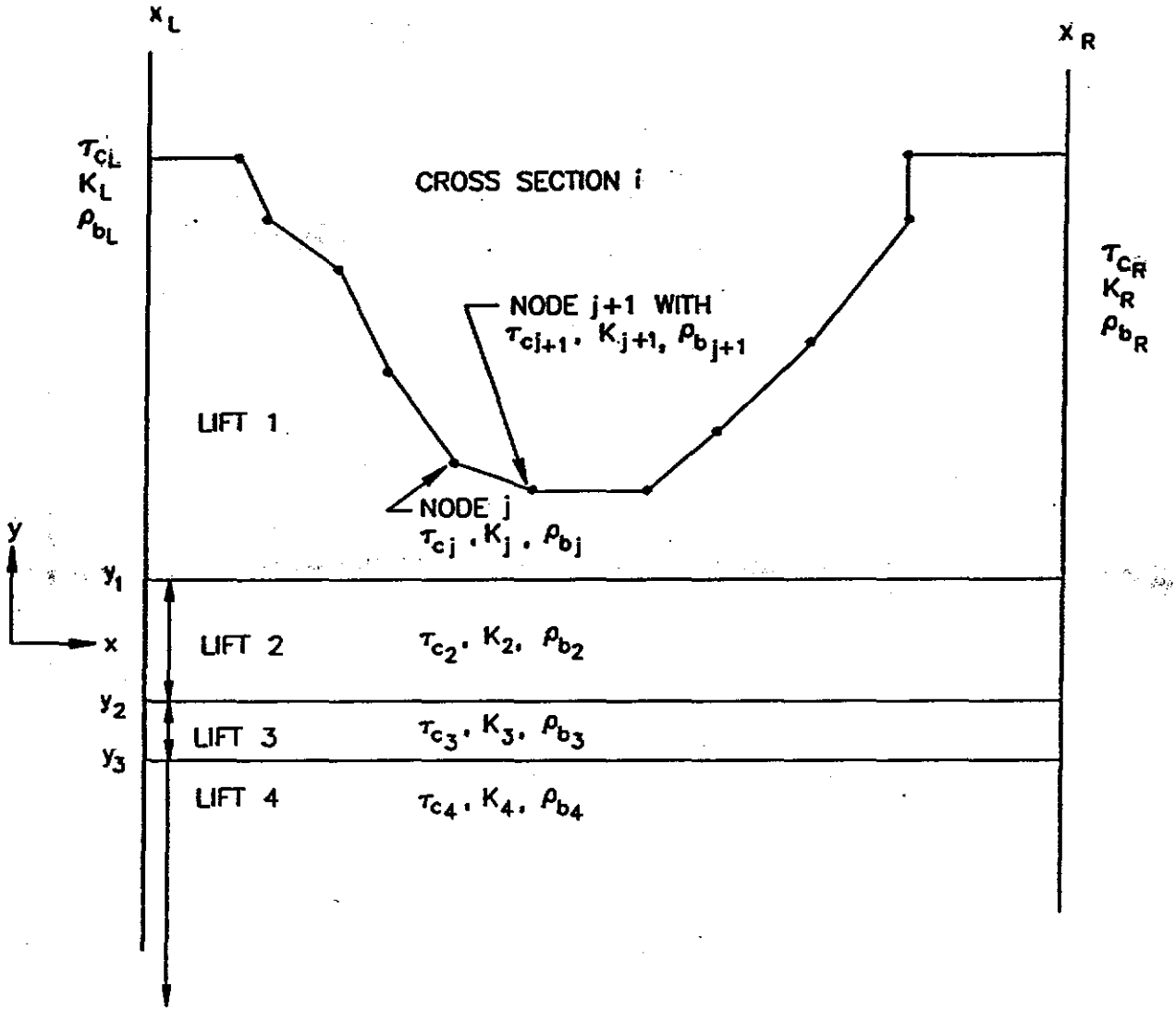

Figure 3.4. Variation of soil parameters at a cross section.

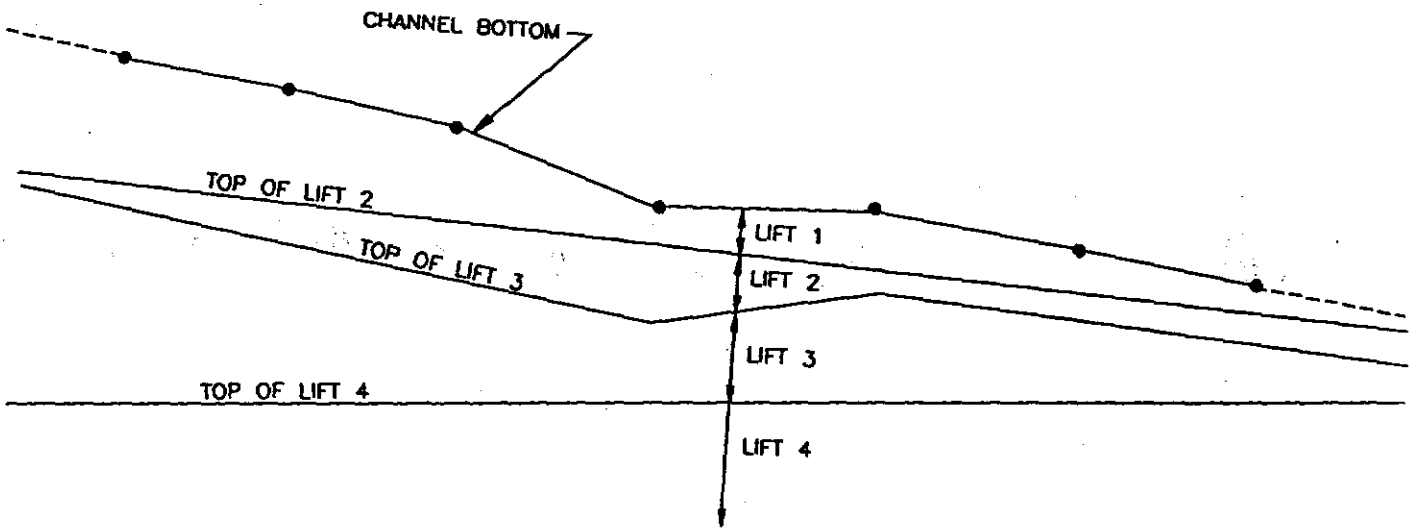

Figure 3.5. Variation of soil parameters along the channel profile.

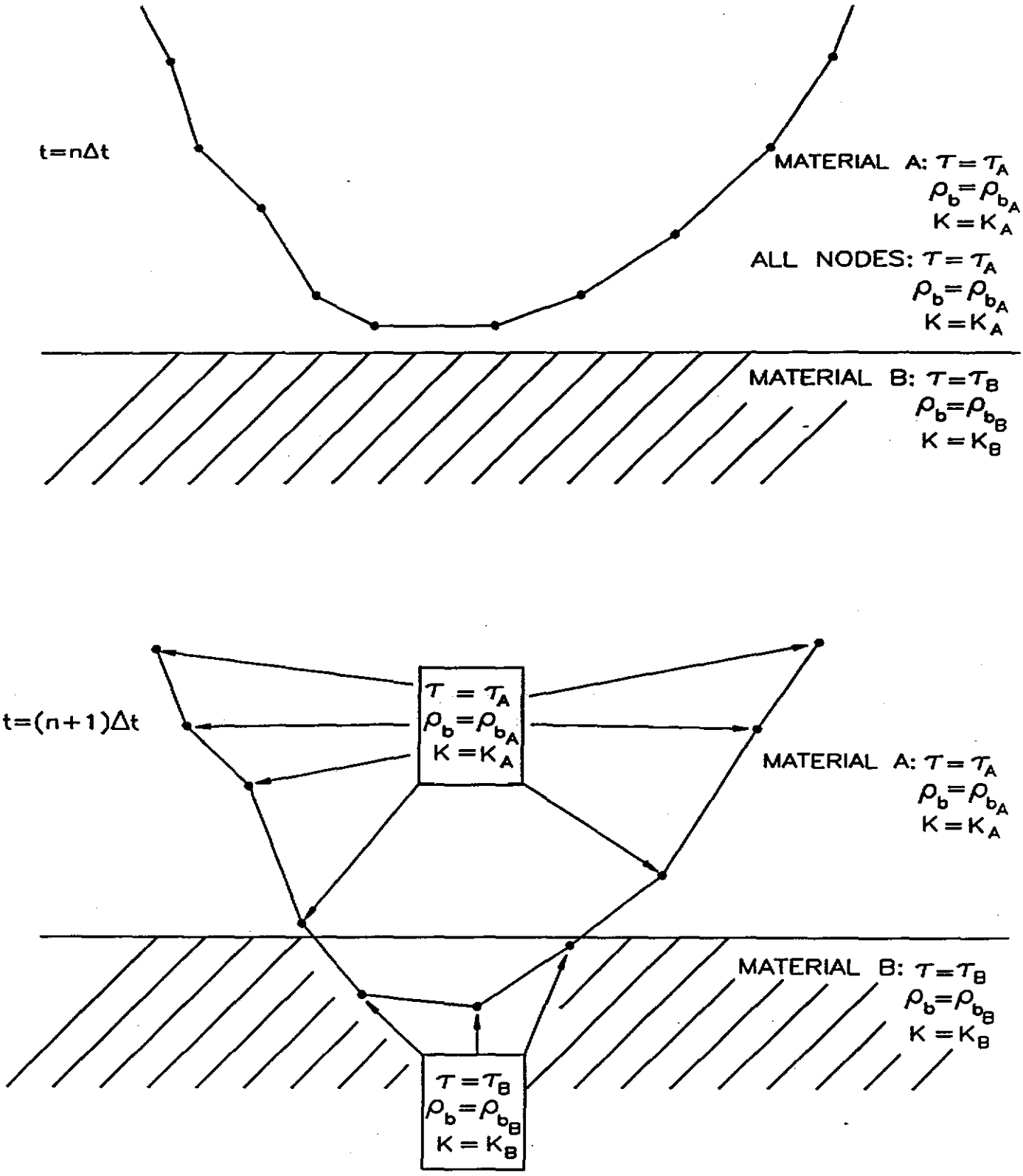

Figure 3.6. Illustration of resetting of nodal soil parameters due to channel movement into a new material.

3.2. OPEN CHANNEL FLOW PROFILES

Flow routing begins with the last channel cross section. The flow depth at this cross section is either input by the user or the user can specify calculation of the normal or critical depth. Routing progresses upstream by utilizing equations (2)-(7):

$$h_i = d_i + Y_i + \alpha \frac{V_i^2}{2g} \tag{2}$$

$$h_i = h_{i+1} + h_{f_{i,i+1}} \tag{3}$$

$$h_i = d_i + Y_i + \alpha \frac{V_i^2}{2g} = d_{i+1} + Y_{i+1} + \alpha \frac{V_{i+1}^2}{2g} + h_{f_{i,i+1}} \tag{4}$$

$$h_{f_{i,i+1}} = S_{f_a} \Delta X = \frac{1}{2} (S_{f_i} + S_{f_{i+1}}) \Delta X \tag{5}$$

$$S_f = \left[\frac{n \, Q/A}{C_n R^{2/3}} \right]^2 \tag{6}$$

$$R = \frac{A}{P} \tag{7}$$

and the standard step method. The solution procedure is as follows:

(1) Starting at the control section with a given depth d_i, calculate h_i from equation (2).

(2) Assume a value for d_{i+1} (at the next cross section) and thus assume values for area, velocity and total head, $h_{i+1,1}$, at i+1.

(3) Calculate the head loss $h_{fi,i+1}$ from equations (5) and (6), given the input roughness.

(4) Using equation (4), estimate $h_{i+1,2}$ from the assumed value of d_{i+1} and the calculated value for $h_{fi,i+1}$.

(5) Compare $h_{i+1,2}$ to $h_{i+1,1}$. If agreement is not sufficient, make a new estimate for d_{i+1} from the following depth estimation algorithm:

• if routing upstream, calculate the average head between sections from

$$h_a = \frac{1}{2}(h_{i+1,1} + h_{i+1,2}) \tag{116}$$

and estimate the new depth from

$$d_{i+1,2} = h_a - Y_{i+1} - \alpha\left(\frac{V_{i+1,1}^2}{2g}\right) \tag{117}$$

- if routing downstream:

  - if d_i is greater than or equal to normal depth, estimate $d_{i+1,2}$ from

$$d_{i+1,2} = d_{i+1,1}\left(\frac{h_{i+1,2}}{h_{i+1,1}}\right); \qquad h_{i+1,1} > h_{i+1,2} \tag{118}$$

$$d_{i+1,2} = d_{i+1,1}\left(\frac{h_{i+1,1}}{h_{i+1,2}}\right); \qquad h_{i+1,1} < h_{i+1,2} \tag{119}$$

  - if d_i is less than normal depth, estimate $d_{i+1,2}$ from equations (116) and (117).

The new depth, $d_{i+1,2}$, can be held to change only a percentage of $d_{i+1,1}$ if desired.

(6) Repeat steps 2-5 until $h_{i+1,1}$ and $h_{i+1,2}$ converges.

(7) The depth at cross section i+1 becomes the control for section i+2 and steps 1-6 are repeated.

Routing continues upstream with area, wetted perimeter, depth, and friction slope being stored for each cross section until the channel inlet, a steep GVFR #1, or a scour hole is encountered. If GVFR #1 is steep, the flow is routed downstream using the procedure outlined above until the next downstream GVFR or scour hole is reached. If the channel inlet is obtained the model proceeds to the sediment generation and routing routines. If a scour hole is encountered, CHANNEL continues the routing through the scour hole by the following procedure:

(1) Using the calculated flow parameters at the scour hole exit as the control, compute the flow profile upstream through the scour hole until the depth transitions through critical depth or the depth approaches zero on a steep section of the channel. If either of these occurs, set a flag for a possible hydraulic jump and move the routing procedure to the scour hole brink.

(2) Calculate the critical flow area and depth at the scour hole brink. This is done by utilizing a cubic spline (Conte and de Boor, 1980) to 'plot' the shape factor versus flow depth curve.

The shape factor is defined as (Simon, 1986)

$$Z_i = \left(\frac{A_i^3}{B_i}\right)^{1/2} \tag{120}$$

where Z_i is the shape factor, A_i is the flow area, and B_i is the water surface width at cross

section i. Calculate the critical shape factor:

$$Z_{c_i} = \left(\frac{Q_i^2}{g}\right)^{1/2} \tag{121}$$

where Q_i is the flow rate and g is the acceleration of gravity. Determine the critical depth from the shape factor versus depth curve.

(3) Using the critical depth as the control at the scour hole brink, calculate the flow profile in the downstream direction through the scour hole. The flow area, depth, wetted perimeter, and friction slope for each cross section are stored for this flow profile also.

(4) Calculate the conjugate flow profile to the downstream profile (upstream control) by computing the momentum versus flow depth curves. Momentum at point i is defined as

$$M_i = \bar{y}_i A_i + \frac{Q_i^2}{gA_i} \tag{122}$$

where $\bar{y}_i$ is the vertical distance from the water surface to the centroid of the flow area, A_i is the flow area, Q_i is the flow rate, and g is the acceleration of gravity.

(5) Knowing the momentum at each cross section of the downstream profile, the momentum of the conjugate profile is known at each cross section and the depth of the conjugate profile can be found by increasing the depth incrementally along the momentum versus depth curve until the calculated momentum equals the given momentum (within tolerance).

(6) Check for intersection of the conjugate profile with the upstream profile. If the two profiles intersect, a jump has occurred in the scour hole at the point of intersection. The flow profile of the scour hole becomes the downstream profile up to the occurrence of the jump and the upstream profile from the jump to the scour hole exit. The downstream control for the channel reach just upstream of the scour hole is set to critical depth and routing continues upstream of the scour hole. If the conjugate profile does not intersect the upstream profile, the upstream profile (downstream control) becomes the scour hole profile. The control for the channel reach just upstream is set to the depth at the scour hole brink.

(7) Begin routing upstream of the scour hole using the control set in step 6.

A critical portion of the scour hole routing is determining when the flow is open channel flow with gradually varied flow, or when the flow forms an hydraulic jump, submerged jet, or free jet. The routing routines discussed above will determine the actual profile through the scour hole. In CHANNEL, the following decision criteria are used to determine the proper flow form (refer to Figure 2.4):

Slope on segment B less than critical

- Flow profile is open channel flow with gradually expanding and contracting flow (see Figure 2.4a).

Slope on segment B greater than critical

- If the tailwater depth, d_t, is greater than d_c, at the brink (curve 4 in Figure 2.4b), then the scour hole is assumed to act as an open channel with gradually expanding and contracting flows.
- If the tailwater depth, d_t, is less than d_c but greater than zero (profile 5 in Figure 2.4b), treat as a submerged jet.
- If an hydraulic jump occurs on either of segments B, C, or D using procedures stated in step 6 above, treat as open channel flow upstream of the jump and a submerged jet downstream of the jump.
- If the tailwater level is below the brink elevation, Y_b, determine if the scour hole geometry can support a free overfall. If it can, then treat as a free overfall. If it cannot, a submerged jet is present in the scour hole. Procedures for determining if the scour hole geometry can support a free overfall are presented in section 3.3.

Computations continue upstream until the channel inlet or a steep sloped GVFR #1 is reached.

3.3. FREE JET PROFILES

Before calculation of a free jet profile is feasible, it must be established that the scour hole geometry can support a free overall. CHANNEL performs several checks on the scour hole geometry to determine if a free overfall can exist. The following is a discussion of that procedure.

3.3.1. Brink Location

The first step is to determine the potential jet brink location. The free jet brink is defined as the point along the channel where the flow has the potental to separate from the channel boundary. To locate this point, CHANNEL begins at the scour hole entrance and checks for segments within the scour hole that have supercritical slope. If a segment has supercritical slope, the model calculates the normal flow depth on that segment, the end-depth ratio from equation (14):

$$EDR = T_e = \frac{F_o^2}{F_o^2 + \frac{4}{9}} \tag{14}$$

and the jet streamline slope from a variation of equation (34):

$$\left(\frac{dy}{dx}\Big|_{brink}\right) = \psi = d_{n_u}\left[\frac{1 - \frac{T_e}{2} + \frac{F_o^2}{2}\left(1 - \frac{1}{T_e^2}\right)}{\left(\frac{F_o^2}{T_e^2} + \frac{3T_e}{4}\right)}\right]^{\frac{1}{2}} + S_{o_u} \tag{123}$$

where d_{nu} is the normal depth and S_{ou} is the bed slope upstream of the segment under

consideration. If the jet streamline slope is less than the channel segment slope, a free jet is possible and the brink location is set to the first node of the channel segment. This is illustrated in Figure 3.7. Free jets can also occur when headwall undercuts exist. CHANNEL checks for undercutting of the headwall and if the beginning of an undercut is reached before a segment is found whose slope exceeds the streamline slope, the brink is located at the beginning of the undercut, as shown in Figure 3.8.

Jets formed under the conditions just described are termed supercritical jets.

If the model has not located the brink from the above procedures, another check is made utilizing user judgement to decide if a free jet is possible. This check establishes that a free jet can or cannot exist in scour holes with the overfall brink located at the first node of the scour hole. In this case, the upstream GVFR slope is subcritical and equation (123) cannot be used to determine streamline slope. Equation (28) would predict a streamline slope equal to the GVFR segment slope just upstream of the scour hole entrance (redundant information). Therefore, CHANNEL compares the difference between the scour hole entrance segment slope and the slope of the segment just upstream of the entrance. If the difference is larger than the value input by the user, a free jet is possible, as illustrated in Figure 3.9. The potential brink is located at the scour hole entrance. This method is used due to a lack of information on jet separation from the boundary.

Jets formed under these conditions are termed subcritical jets.

3.3.2. Free Jet Establishment

Once it has been determined that the scour hole can support a free jet, the model checks for the relationship between the tailwater elevation and the brink elevation. If the tailwater elevation falls between the brink elevation and critical depth elevation at the brink (profile 5 in Figure 2.4b), the flow is considered to be a submerged jet. If the tailwater elevation falls below the brink elevation, a free jet is considered to exist in the scour hole.

3.3.3. Jet Trajectory

In order to determine the point where the jet impinges on the channel boundary and the resulting shear distribution, the jet trajectory must be computed. CHANNEL begins by calculating the end-depth ratio by

subcritical jet:

$$EDR = \frac{d_b}{d_c} = .6971 - .0232\ S_R - .0019\ S_R^2 + .000153\ S_R^3 + 8.56 \times 10^{-6}\ S_R^4 - 7.7 \times 10^{-7}\ S_R^5 + 1.26 \times 10^{-6}\ S_R^6 \quad (8)$$

where

$$S_R = \frac{S_o}{S_c} \quad (9)$$

and S_o is the upstream channel slope and S_c is the critical channel slope, or by

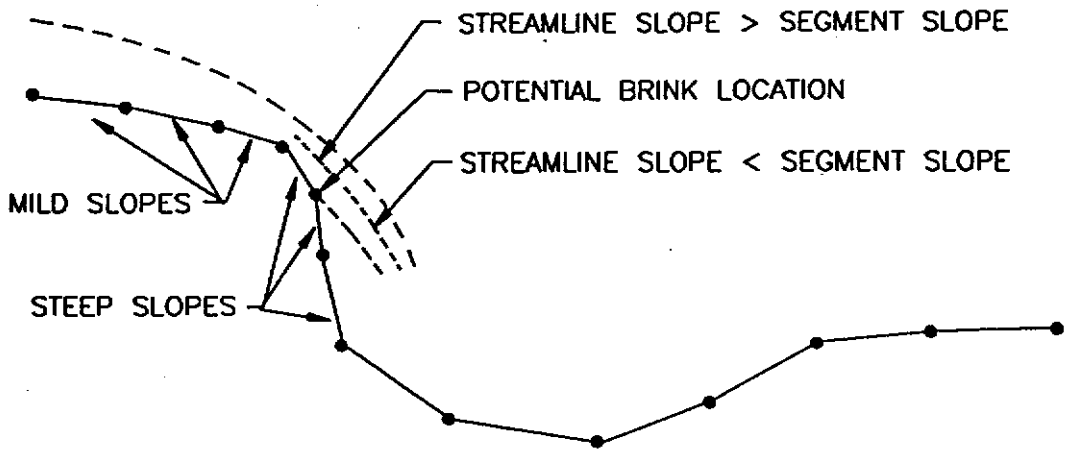

Figure 3.7. Location of potential jet brink for a free jet.

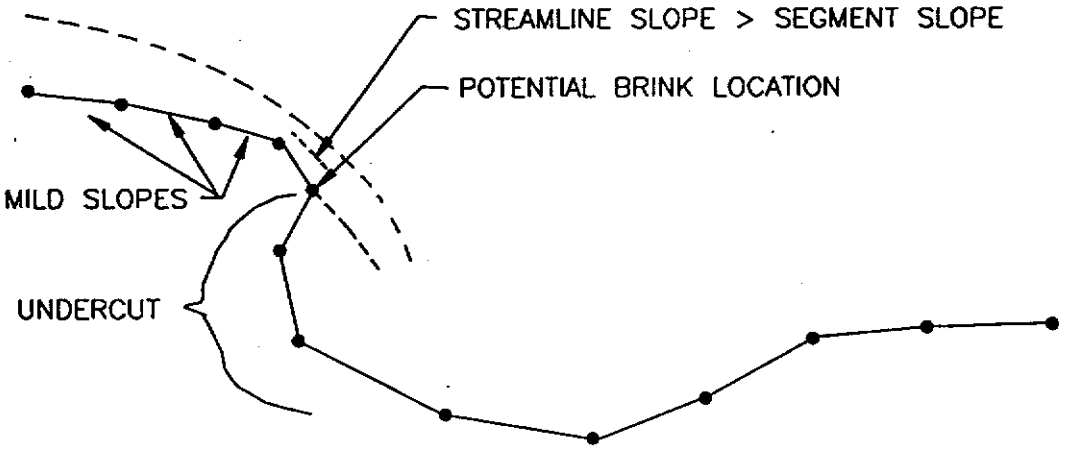

Figure 3.8. Potential brink location at an undercut headwall.

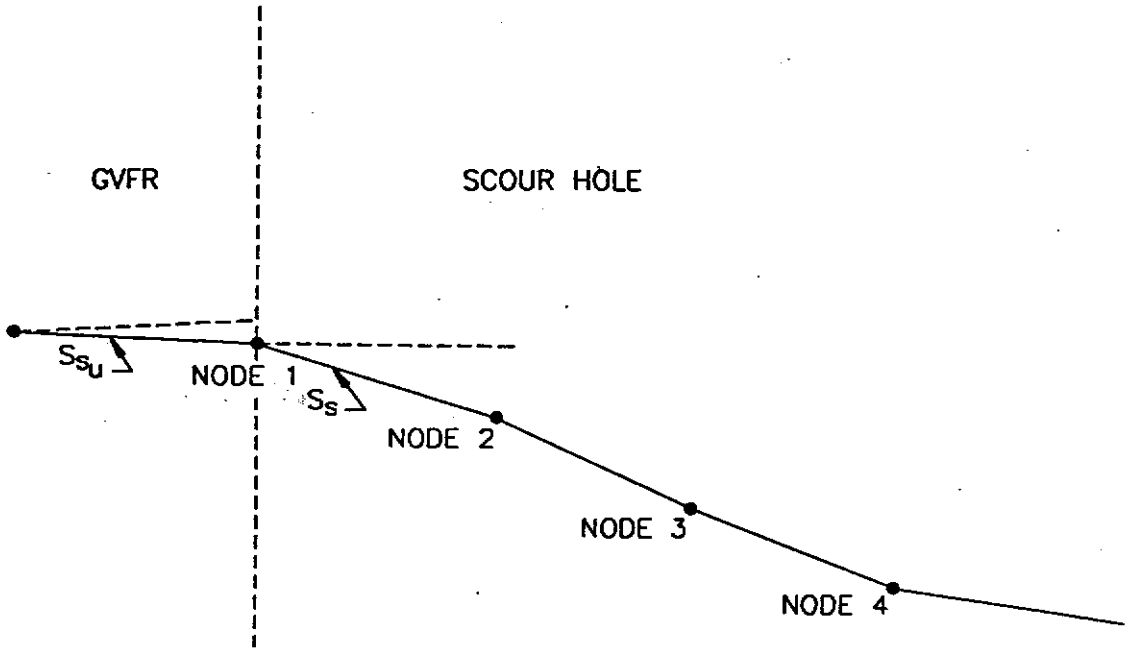

IF $S_s - S_{s_u} \geq S_{s_c}$; FREE JET IS POSSIBLE WITH BRINK LOCATED AT NODE 1

IF $S_s - S_{s_u} < S_{s_c}$; FREE JET NOT POSSIBLE

Figure 3.9. Location of potential jet brink under subcritical jet conditions.

supercritical jet:

$$EDR = \frac{d_b}{d_n} = \frac{F_o^2}{F_o^2 + \frac{4}{9}} \tag{14}$$

where

$$F_o = \frac{U_n}{\sqrt{g\, d_n}} \tag{15}$$

where U_n is the upstream velocity corresponding to the normal depth, d_n, and g is the acceleration of gravity. The brink depth is then calculated from

$$d_b = d_c\,(EDR)(RF); \quad \frac{d_c}{k_s} \le 10 \tag{12}$$

$$d_b = d_c(EDR); \quad \frac{d_c}{k_s} > 10 \tag{13}$$

where R_F is calculated by

$$RF = -0.75 + 1.05\,\frac{d_c}{k_s}; \quad \frac{d_c}{k_s} \le 10 \tag{10}$$

$$RF = 1; \quad \frac{d_c}{k_s} > 10 \tag{11}$$

where d_c is critical depth and k_s is bed grain roughness given by d_{65}. Knowing the brink depth, the flow area at the brink is determined. With the flow area and the flow rate from the flow routing algorithm, the y and z components of the flow velocity at the brink are then calculated from

$$V_{oy} = V_b \sin\alpha \tag{124}$$

$$V_{oz} = V_b \cos\alpha \tag{125}$$

where V_b is the brink velocity and alpha is the slope angle of the channel segment just upstream of the brink.

The z coordinate of the point of impact between the jet and the surface of the plunge pool is determined from:

subcritical jet:

$$z_i = (V_{ox})\, t_i \tag{24}$$

where t_i, the time required for the flow to travel from the brink to the point of impact, is solved from

$$y_i = D_p = (V_{oy})\, t_i - \frac{g t_i^2}{2} \tag{25}$$

and D_p is the distance from the brink to the tailwater surface; or by

supercritical jet:

$$z_i = \frac{1}{\varepsilon}\left[\sqrt{\psi^2 - 2\varepsilon D_p} - \psi\right] \tag{36}$$

where

$$\varepsilon = \left(\frac{T_e}{F_o}\right)^2 \tag{37}$$

ψ is calculated from equation (123), T_e is the end-depth ratio, and F_o is the Froude number (equation (15)).

The angle of impact is calculated from:

subcritical jet:

$$\phi = \tan^{-1}\left(\frac{V_{oy} - g t_i}{V_{ox}}\right) \tag{126}$$

supercritical jet:

$$\phi = \tan^{-1}\left[-(\psi + \varepsilon z_i)\right] \tag{127}$$

Jet width at the point of plunge is determined from

$$2b_o = d_b \cos\phi \tag{32}$$

where b_o is the jet half-width.

The point where the jet impinges on the channel boundary is determined by projecting the point of impact to the boundary at the angle ϕ. This is illustrated in Figure 3.10. The length along the line of projection (H_f) is used in shear computations.

The angle the impact point line of projection forms with the channel boundary is termed the impingement angle. The impingement angle is calculated from

$$\theta = \phi + \alpha_{pip} \tag{128}$$

where α_{pip} is an angle reflecting scour hole geometry and the spread of the jet around the point of

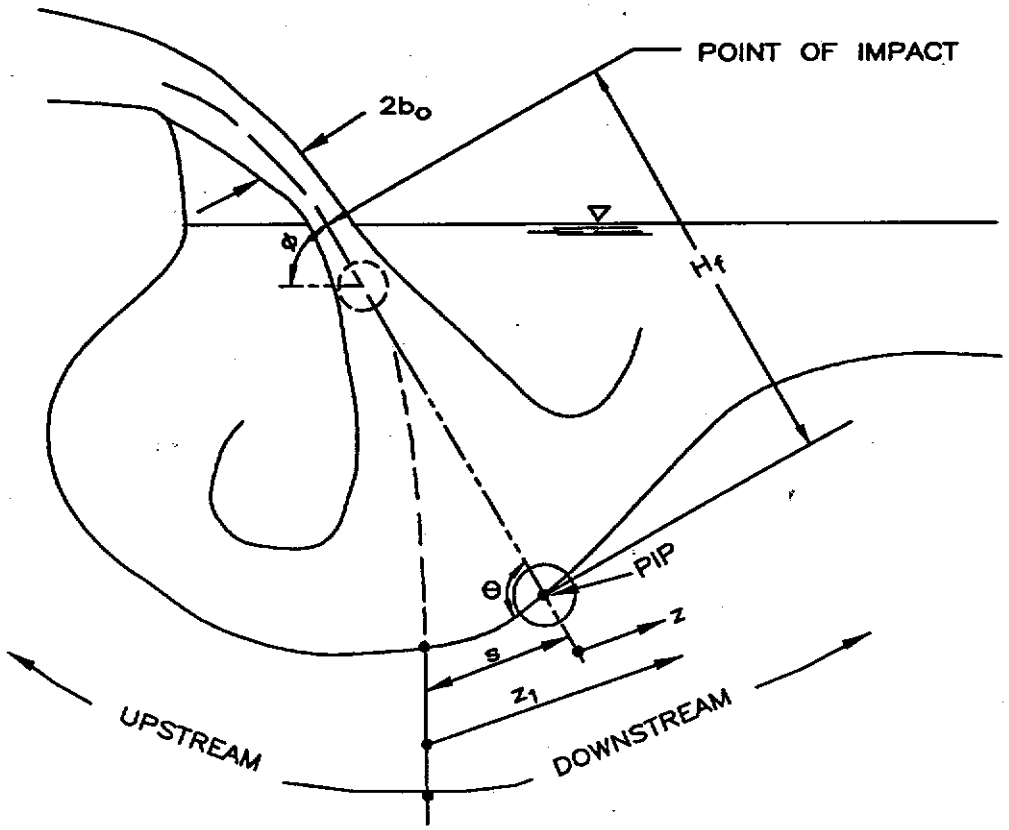

Figure 3.10. Location of point of impingement (pip).

impingement (pip). Calculation of α_{pip} is discussed in section 3.4.1.2b.

If the pip occurs beyond the scour hole exit as illustrated in Figure 3.11a, CHANNEL will assimilate enough of the downstream GVFR into the scour hole to insure that the pip is the within the limits of the scour hole (Figure 3.11b).

3.4. SEDIMENT GENERATION

Once the flow profile data for each cross section has been calculated and stored, the detachment/deposition calculations begin. First, the shear distribution at each cross section is estimated. Then the transport capacity at each cross section is calculated. Using the transport capacity and sediment load, the amount of detachment/deposition occurring at each cross section is determined.

3.4.1. Shear Distribution

Two types of shear stress distribution must be calculated: lateral and longitudinal. CHANNEL uses lateral shear stress distributions to determine the amount of detachment that occurs at a cross section. For gradually varied flow this is straightforward. In segments where hydraulic jumps, submerged jets, or free jets occur, longitudinal shear stress distributions are calculated which are transformed into lateral shear distributions.

3.4.1.1. Lateral Shear Stress Distribution

CHANNEL gives the user two options for lateral shear stress distribution: the Wang, Foster, and Wilson's (1992) modified Foster and Lane (1983) equation and the area method of Lundgren and Jonsson (1964).

Using the modified Foster and Lane equation, the shear at any node j of cross section i is given by

$$\tau_j = \tau_d\left(1 + \frac{1}{\zeta}\right)\left[1 - \left(1 - 2x_{j,i}\right)^{\zeta}\right]$$

$$w_i/d_i \geq 2.8 \qquad (129)$$

$$\zeta = \left(\frac{2w_i}{d_i}\right)^{\frac{1}{2}}$$

or

$$\tau_j = \sigma\left[1 - \left(1 - 2x_{j,i}\right)^{\frac{1}{\sigma - 1}}\right]$$

$$1.0 \leq w_i/d_i < 2.8 \qquad (130)$$

$$\sigma = 1.1226\left(\frac{w_i}{d_i}\right)^{0.23}$$

or

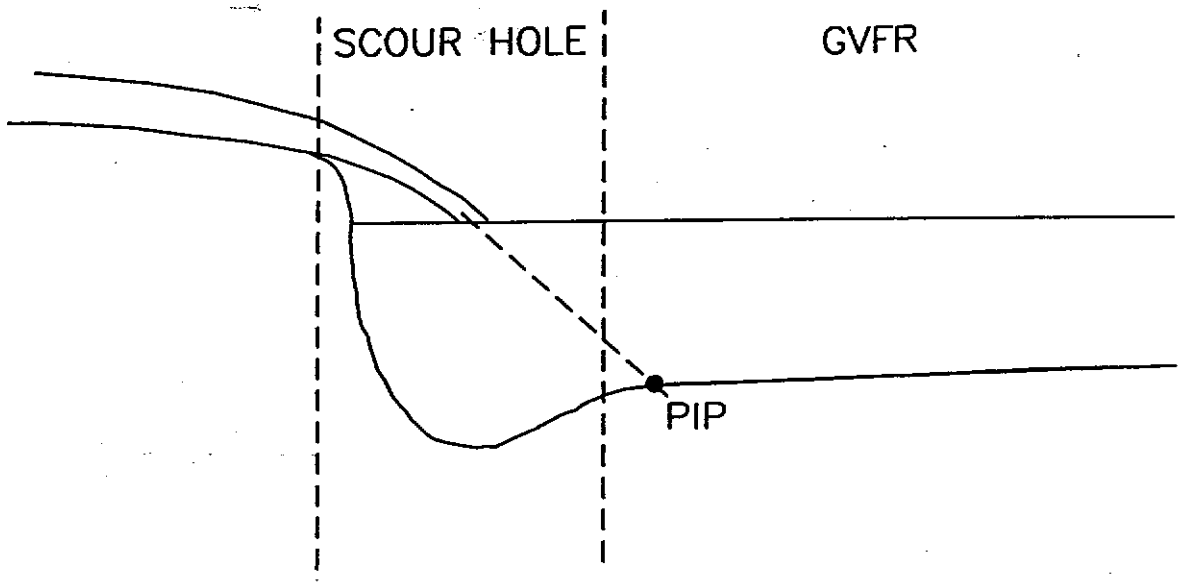

(a) pip located outside of scour hole boundary.

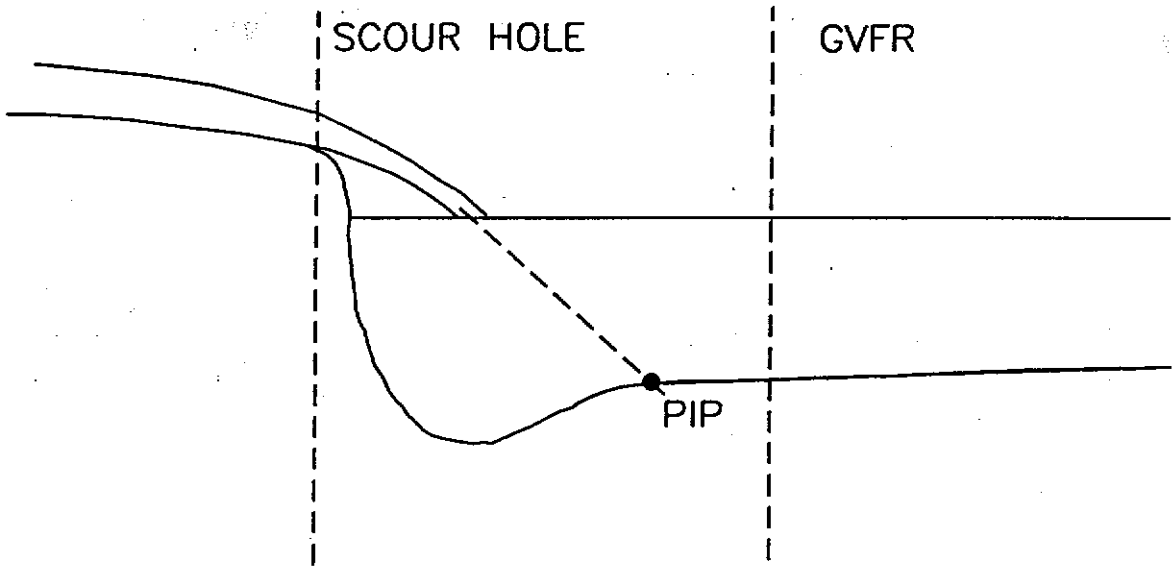

(b) new location of scour hole boundary to include pip in scour hole.

Figure 3.11. Schematic showing relocation of scour hole boundary to include pip within scour hole.

$$\tau_j = \tau_a [1 - (1 - 2x_{j.})^{2.9}] \qquad w_i/d_i < 1.0 \qquad (131)$$

where τ_a is given by

$$\tau_a = \gamma R_i S_{f_i} \qquad (42)$$

and

$$x_{j.} = \frac{x_j}{WP_i} \qquad (41)$$

where WP_i is the wetted perimeter length. The shear on cross section segment j is taken to be the average of the shears at nodes j and j+1.

In the Lundgren and Jonsson (1964) method, the shear on segment j is given by

$$\tau_j = \frac{\gamma \Delta A_j S_f}{\Delta WP_j} \qquad (134)$$

where τ_j is the shear on segment j, S_{fi} is the friction slope, and ΔWP_j is the length of segment j. ΔA_j is evaluated by Lundgren and Jonsson's (1964) area method. Figure 3.12a shows a cross section where, at each node below the water surface, a line that bisects the angle between two adjacent segments has been projected to the water surface. ΔA_j is defined as the area bounded by segment j, the water surface, and the corresponding bisectors. As can be seen in Figure 3.12a, it is possible for bisectors to intersect below the water surface. This is undesirable because of the complexity involved in calculating ΔA_j where this occurs. The situation is remedied in CHANNEL by shifting the bisectors until they no longer intersect below the water surface. Figures 3.12b and 3.12c illustrate this process. The procedure used is as follows:

(1) Start with the first bisector.

(2) Determine the x coordinate of the bisector-water surface intersection.

(3) Check each subsequent bisector-water surface intersection for an x coordinate less than the x coordinate found in step (2).

(4) If another bisector is found that intersects the current bisector below the water surface, bisect the distance between the points where each bisector meets the water surface and set both bisector's water surface intersection x coordinates to this value. Save this value as the current bisector's water surface intersection x coordinate (see Figure 3.12b).

(5) Step to the next bisector and continue steps 2-4 until all bisectors along the cross section have been checked.

(6) Start with the last bisector and repeat steps 3-5 in the opposite direction. These coordinate values are also stored.

(7) Loop through each bisector and set the water surface intersection x coordinate to the average of the values stored in steps 4 and 6.

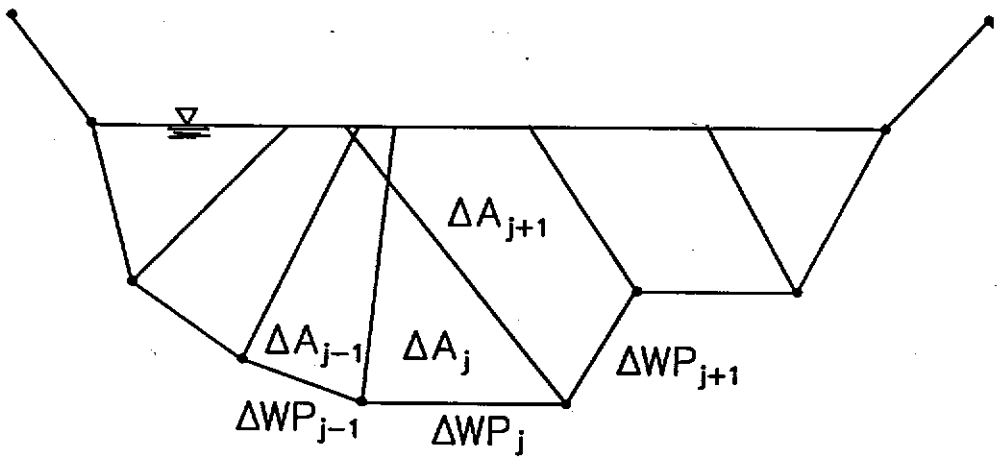

(a) channel cross section with initial boundary segment angle bisectors.

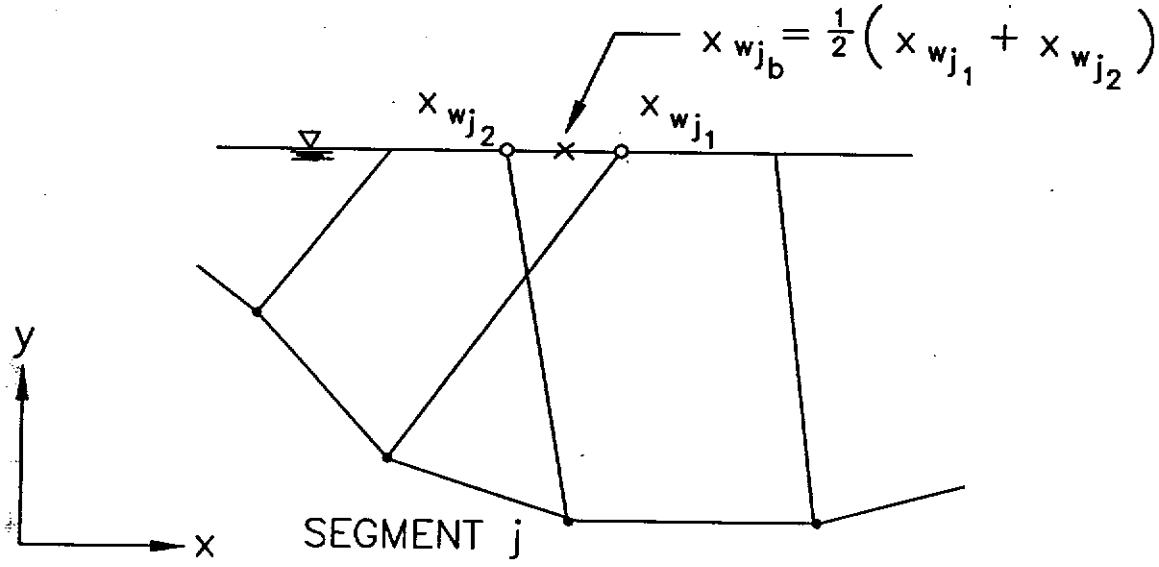

(b) illustration of location of new bisector-water surface intersection for segment j.

Figure 3.12. Illustration of CHANNEL adaptation of Lundgren and Jonsson (1964) area method.

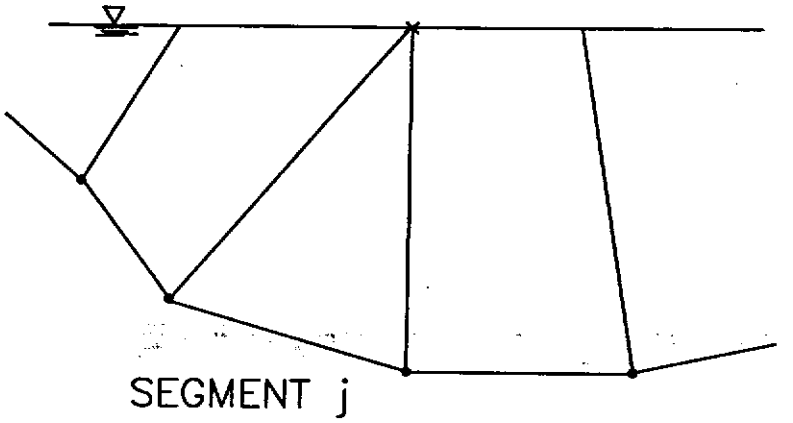

(c) new bisector positions after shifting bisector-water surface intersection.

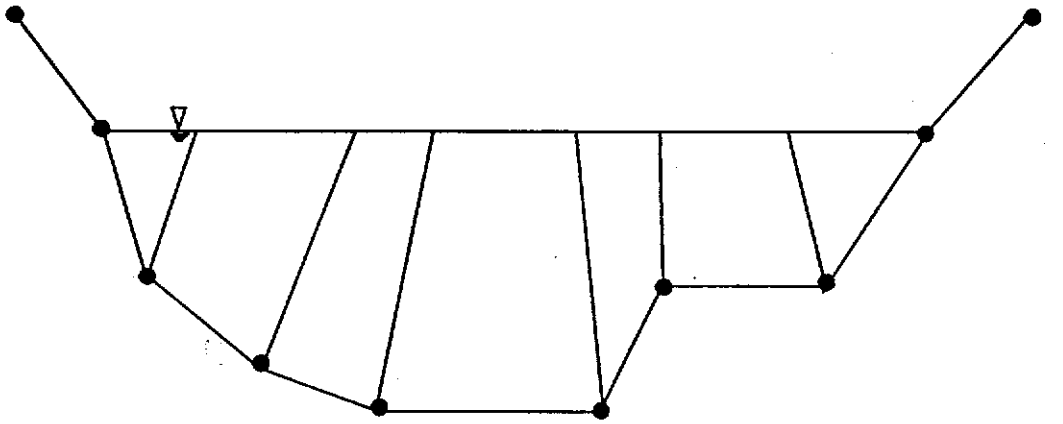

(d) cross section with new bisector configuration.

Figure 3.12 (cont'd). Illustration of CHANNEL adaptation of Lundgren and Jonsson (1964) area method.

The purpose of steps 6 and 7 is to "smooth" out the shears calculated over the cross section perimeter. Performing steps 1-5 without steps 6 and 7 tends to skew the shear stress distribution to one side of the cross section. Figure 3.12d shows the same cross section in Figure 3.12a with new bisector locations.

3.4.1.2. Longitudinal Shear Distributions

Longitudinal shear distributions are calculated for free jets, submerged jets, and the downstream portion of hydraulic jumps. The shear models are same for jumps and submerged jets. These two entities will be discussed first with a discussion of free jets following.

3.4.1.2a. Shear in Hydraulic Jumps and Submerged Jets

Jumps and submerged jets are handled almost identically by CHANNEL. Lateral shear distributions are computed upstream of the jump roller and upstream of the point of plunge for submerged jets. The point just upstream of the roller or upstream of the point of plunge is defined as the brink. This is illustrated in Figure 3.13. Downstream of the brink, longitudinal shear distributions are computed utilizing wall jet equations or impinging jet equations, depending upon the scour hole geometry.

To determine if wall jet or impinging jet equations should be used, the angle of the jet streamline at the brink is calculated from

$$\beta = .316 \sin\alpha + 0.15 \ln\left(\frac{D_p + y_o}{y_o}\right) + 0.13 \ln\left(\frac{d_t}{y_o}\right) - 0.05 \ln\left(\frac{U_o}{\sqrt{g y_o}}\right) \tag{86}$$

where D_p is the height of the brink above the point of impingement, y_o is the depth of flow at the brink, U_o is the flow velocity at the brink, α is the slope of the brink section of the scour hole and d_t is the depth of the tailwater above the point of impingement. If $\beta - \alpha < \delta_c$ (refer to section 2.3.2.2.) where δ_c is a user defined value, the jet is considered to be a wall jet and the shear at downstream cross sections is calculated from

$$\tau_i = C_f \rho \frac{U_o^2}{2} \tag{69}$$

where

$$C_f = \frac{0.2}{\left(\frac{z_i}{b_o}\right)\left(\frac{U_o b_o}{\nu}\right)^{\frac{1}{12}}} \tag{70}$$

where z_i is the distance along the boundary from the brink to cross section i. τ_i is assumed to be the maximum shear stress that occurs on the cross section i's boundary and is applied at the point on the boundary at the point corresponding to the centroid of the flow area. This is shown in Figure 3.14.

If $\beta - \alpha \geq \delta_c$, the jet is considered to be an impinging jet. Discussion of impinging jet shear equations are reserved for the following discussion on free jet shear distributions.

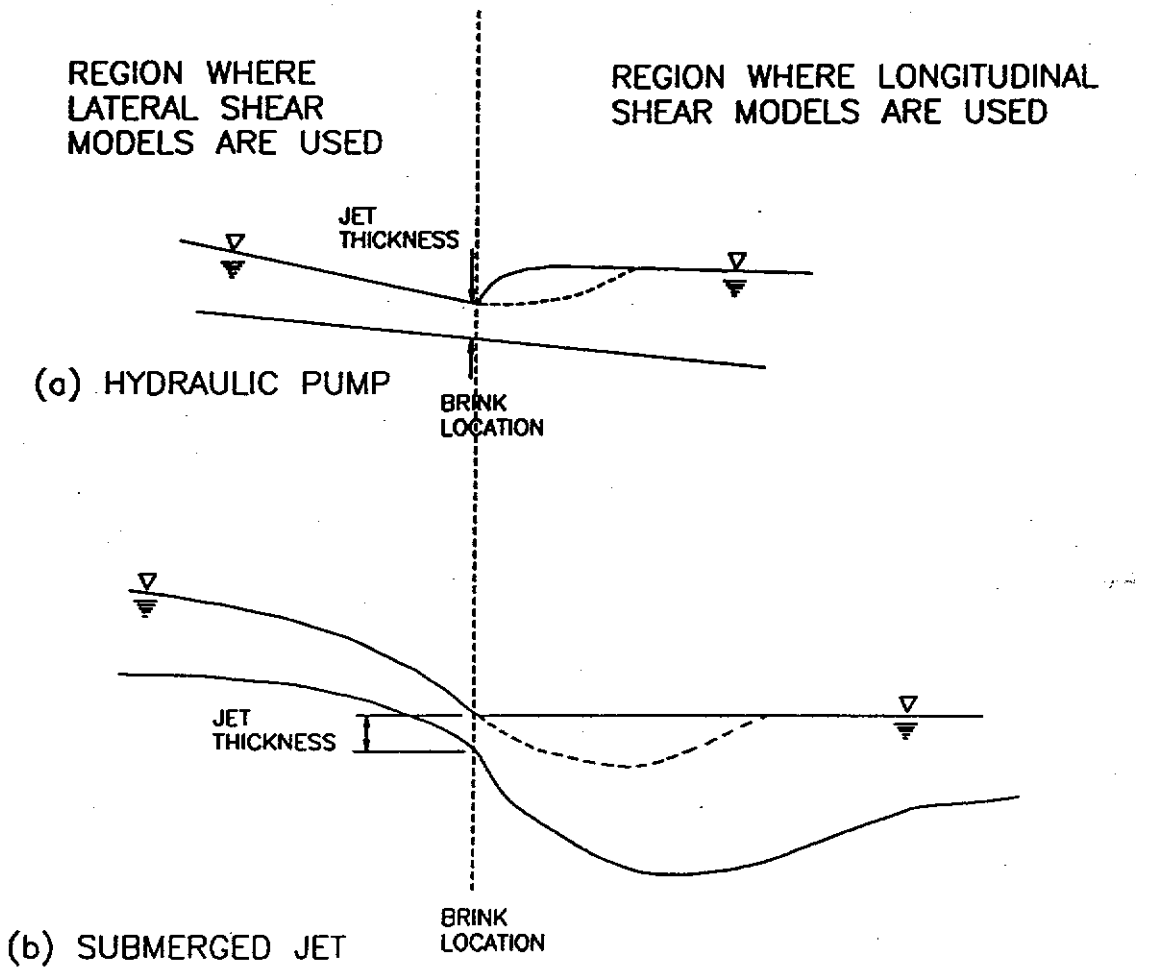

Figure 3.13. Brink locations for (a) hydraulic jump and (b) submerged jet.

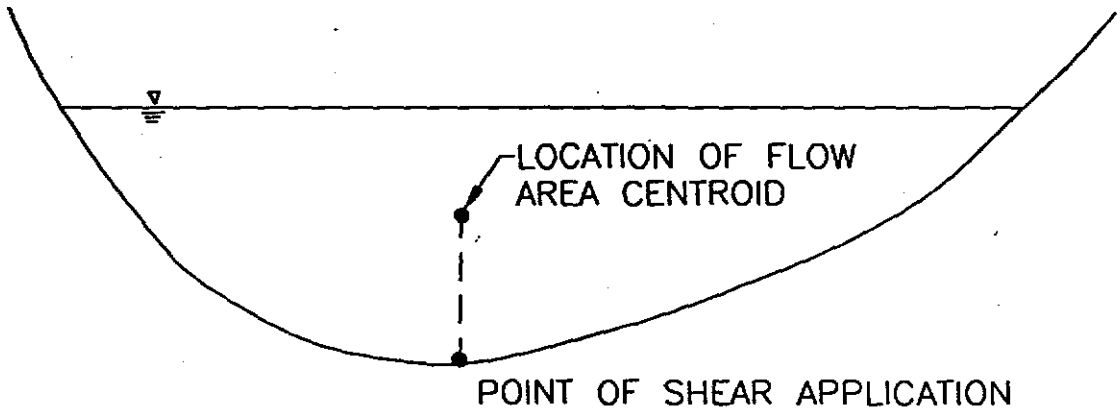

Figure 3.14. Point of application of shear calculated from equation (77).

3.4.1.2b. Free Jet Shear Distributions

When a free jet occurs in a scour hole, the first task performed is to locate the point of stagnation (see Figure 2.5). The stagnation displacement from the point of impingement is calculated from

$$s = \frac{2.15\, H_f \left(1 - \frac{\theta}{90}\right)}{8 \sin\theta} \tag{71}$$

where H_f is the length of the flow path of the jet through the plunge pool and θ is the impingement angle calculated from equation (128).

Upon location of the stagnation point, CHANNEL divides the scour hole into two zones: the impingement zone (Zone II, Figure 2.5) and the wall jet zone (Zone III, Figure 2.5). The model uses an iterative procedure to determine the extent of the impingement zone and the values of α_{pip} and θ. The procedure is outlined as follows (the reader is referred to Figure 3.15):

(1) Assume a value for $\theta = \phi + \alpha_{pip} = 45°$

(2) Calculate a value for ξ_u and ξ_d, the Beltaos (1976a) scaling parameters from

$$\xi_{u,d} = H_f \left[.1333 - \left(\frac{\theta_{u,d}}{130}\right)(.0166)\right]; \quad 0° \le \theta_{u,d} \le 130° \tag{135}$$

$$\xi_{u,d} = H_f \left[.1167 - (.05)\left(1 - \frac{180 - \theta_{u,d}}{50}\right)\right]; \quad 130° < \theta_{u,d} \le 180° \tag{136}$$

where

$$\theta_d = \theta$$

$$\theta_u = 180 - \theta$$

(3) Determine the extent of the impingement zone from

$$\begin{aligned} z_{1_u} &= \xi_u \eta_c \\ z_{1_d} &= \xi_d \eta_c \end{aligned} \tag{137}$$

where z_{1u} is the distance along the boundary from the stagnation point to the point of transition in the upstream direction, z_{1d} is the same distance in the downstream direction, and $\eta_c = 2.5$.

(4) With z_{1u} z_{1d}, determine the coordinates of the points on the boundary that correspond to the upstream and downstream points of transition.

(5) Divide the upstream and downstream impingement regions of the boundary into 10 equal

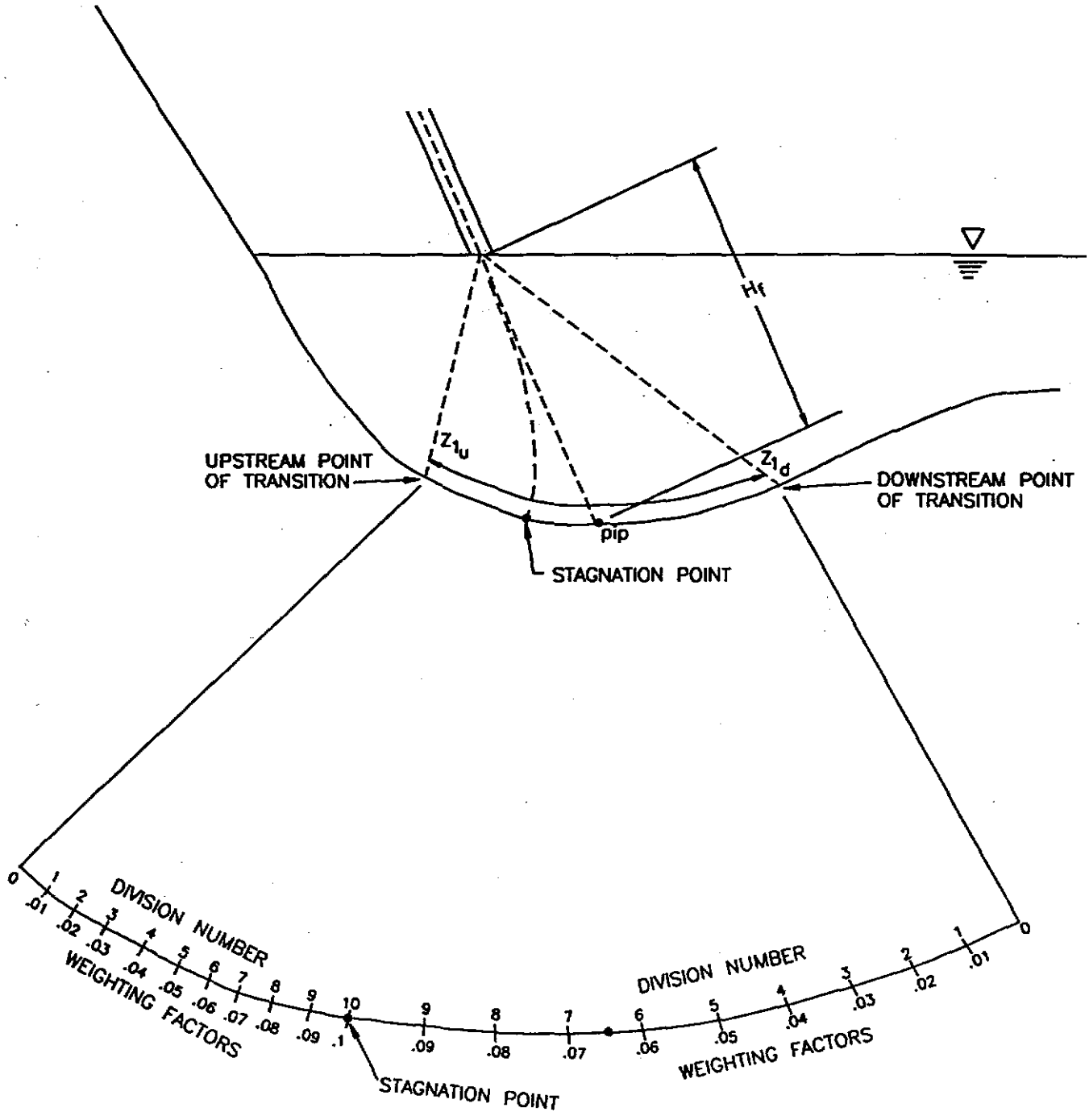

Figure 3.15. Schematic illustrating procedure used to determine θ and α_{pip} in equation (128).

divisions. Assign each division a weighting factor. The divisions closest to the stagnation point are assigned a factor of 0.09 and the divisions farthest from the stagnation point are assigned a factor of 0.00. The sum of the weighting factors over the impingement zone equals one.

(6) Calculate the weighted average impingement zone boundary slope from

$$S_{o_s} = \sum_{j=1}^{10} WF_{j_u} S_{o_{j_u}} + \sum_{j=1}^{10} WF_{j_d} S_{o_{j_d}} \tag{138}$$

where S_{os} is the weighted average impingement region boundary slope, the subscript j refers to the boundary division number, WF is the weighting factor, the subscript u refers to upstream of the stagnation point, the subscript d refers to downstream of the stagnation point, and S_o is the boundary slope at point j. α_{pip} is then calculated from

$$\alpha_{pip} = \tan^{-1}(S_{o_s}) \tag{139}$$

(7) Calculate a new value for θ using equation (128).

(8) Repeat steps 2-7 until successive values of θ converge to within the user input tolerance.

After values for θ_u, θ_d, ξ_u, and ξ_d are determined, the maximum shears at the points of transition are calculated from:

$$\tau_{m_{u,d}} = \frac{C_*(\theta_{u,d})\ \rho\ U_o^2\ b_o}{H_f} \tag{77}$$

where C_* is given by equations (78) and (79). The shears calculated from equation (77) are assumed to be the maximum shears occurring on the sections. CHANNEL also assumes that these shears are applied at point along the cross section boundary that corresponds to the flow area centroid (see Figure 3.14). These shears are used to develop the lateral shear distributions over the cross section boundaries. Transformation of longitudinal shears into lateral shear distributions is discussed in section 3.4.1.2c.

CHANNEL now proceeds to calculate the maximum shear values for all cross sections within the impingement zone. Under ideal conditions, the shear on these cross sections would be predicted from

$$\tau_{i_{u,d}} = \tau_{m_{u,d}}[erf\ (0.833\ \eta_{u,d}) - 0.2\ \eta_{u,d}\ g\ (\eta_{u,d})] \tag{72}$$

However, the above equation predicts the shear to be zero at the stagnation point, which, theoretically, would result in a spike occurring in the channel profile at the stagnation point, as shown in Figure 3.16. Due to jet oscillations and other factors, this spike is not observed in the field or in lab situations. Therefore CHANNEL linearly interpolates between τ_{mu} and τ_{md} to obtain the longitudinal shear distribution for cross sections within the impingement zone. This is also shown in Figure 3.16.

The shear in the wall jet zones is computed by first calculating the distance, z_i, of cross section i from the stagnation point. Cross sections in the wall jet zones must have a

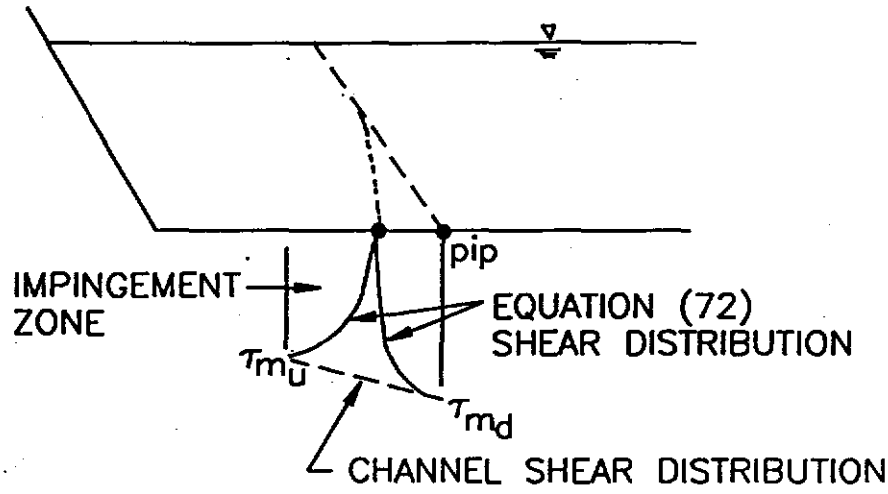

Figure 3.16. Longitudinal impingement zone shear distribution predicted by equation (72) and the shear distribution used by CHANNEL.

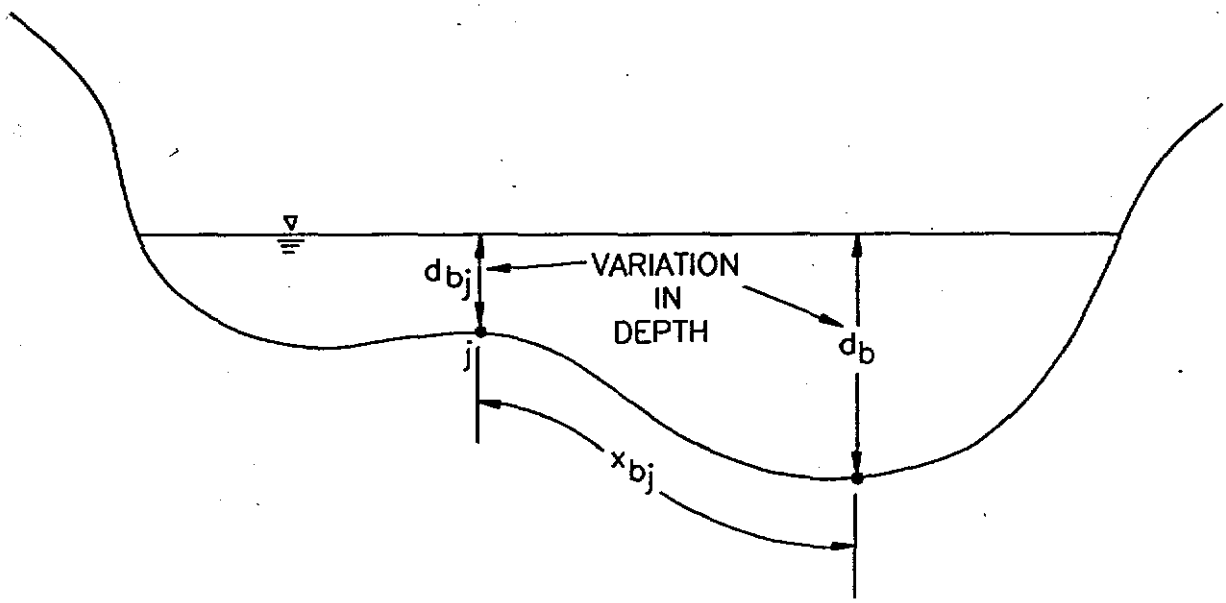

Figure 3.17. Variation in the flow depth at the brink. This variation in depth translates into variation in jet thickness via equation (32).

non-dimensional distance value η_i greater than 2.5 where η_i is given by

$$\eta_{i_{s,d}} = \frac{z_{i_{s,d}}}{\xi_{u,d}} \tag{140}$$

The shear at cross sections upstream of the stagnation point is obtained from

$$\tau_{i_u} = \frac{2.5\ \tau_{m_u}}{\eta_{i_u}} \tag{141}$$

where τ_{mu} is calculated from equation (77). Equation (141) is used in lieu of equations (80)-(84) in order to provide continuity in the shear distribution at the points of transition.

Downstream of the stagnation point, the shear is calculated from

$$\tau_{i_d} = \frac{2.5\ \tau_{m_d}}{\eta_{i_d}} + 1.35\ C_s\ \gamma\ R_i\ S_{f_i} \tag{142}$$

where C_s is factor calculated from

$$C_s = 1 + S_s\left(F_s - 1\right) \tag{143}$$

where F_s is a user input constant greater than or equal to 1 and S_s is a weighting factor given by

$$S_s = \sin\alpha_i \tag{144}$$

where α_i is the channel boundary slope angle at cross section i. S_s is limited to the positive real number domain. This algorithm requires some calibration to determine F_s. The algorithm was developed in order to limit undercutting of the downstream face of the scour hole during the simulation. The authors have never observed a scour hole with downstream undercutting and feel that its occurrence, although possible, is rare in the field. Implementation of the above algorithm, with proper calibration, will produce reasonable scour hole profiles.

3.4.1.2c. Transforming Longitudinal Shears into Lateral Shear Distributions

No model for predicting the lateral shear distribution resulting from jets can be found in the literature. CHANNEL assumes that since the thickness of the jet varies at the brink, as shown in Figure 3.17, the resulting lateral shear distributions on cross sections in the scour hole will vary proportionally with the variation of jet thickness at the brink.

To calculate the lateral shear distributions, CHANNEL first computes a brink depth (or initial jet thickness) function that is normalized by the maximum depth on the brink cross section. This function is given by

$$d_{b_*} = \frac{d_{b_j}}{d_{b_m}} = g\left(x_{b_*}\right) \tag{145}$$

where d_{bj} is the depth at node j of the brink cross section and x_{b*} is the normalized distance along

the cross section boundary from the point of maximum depth to node j, given by

$$x_{b_*} = \frac{x_{b_j}}{W_b} \tag{146}$$

where x_{bj} is the distance along the boundary from the point of maximum depth to node j and W_b is the distance along the boundary from the point of maximum depth to the water surface. x_{b*} varies from -1 to 1 and d_{b*} (or $g(x_{b*})$) varies from 0 to 1.

Next, for each cross section in the scour hole, a function (labeled x_*) similar to equation (146) is developed with values for each node below the water surface. Using this function and the x_{b*} function, CHANNEL linearly interpolates for values of $g(x_{j*})$ from $g(x_{b*})$ for each node j. The shear at node j is calculated from

$$\tau_{ij} = g(x_{j_*})\ \tau_i \tag{147}$$

where τ_i is the longitudinal shear at cross section i and τ_{ij} is the shear at node j of cross section i. The shear in segment j of cross section i is given by

$$\tau_j = \frac{1}{2}(\tau_{ij} + \tau_{ij+1}) \tag{148}$$

3.4.1.2d. Extension of Longitudinal Shear Calculations into GVFRs

After the lateral shear distributions have been calculated for each cross section in the scour hole, CHANNEL checks the GVFR just downstream to determine if the jet equations should be used for shear calculations or if lateral shear models should be used. CHANNEL also checks to determine if the jet dissipates before the scour hole exit is reached. If the jet has sufficiently dissipated, lateral shear models are used instead of jet models. The check is accomplished by the following procedure:

(1) After the lateral shear distributions for jets are computed, calculate the average shear on cross sections downstream of the stagnation point from

$$\tau_{a_{jet}} = \frac{\sum \tau_j L_j}{\sum L_j} \tag{149}$$

where L_j is the length of cross section segment j and τ_j is the shear acting on segment j.

(2) Calculate the average shear based upon the friction slope at each cross section from equation (42).

(3) Calculate the shear velocities at each cross section using both τ_{ajet} and τ_a:

$$U_{*_{jet}} = \sqrt{\frac{\tau_{a_{jet}}}{\rho}}$$
$$U_* = \sqrt{\frac{\tau_a}{\rho}} \tag{150}$$

(4) Use the following criteria to determine the shear model to use:

$$\begin{aligned} &\textit{if} \quad U_{*_{jet}} \geq U_* && \textit{use longitudinal shear model} \\ &\textit{if} \quad U_{*_{jet}} < U_* && \textit{use lateral shear model} \end{aligned}$$

3.4.2. Transport Capacity

CHANNEL uses the Yalin (1963) equation as modified by Foster and Meyer (1972b) and presented in Chapter 2.

3.4.2.1. Single Particle Size Transport

With the correct shear velocity (jet or lateral), the boundary Reynold's number is calculated and the critical mobility number, Y_{cr}, is computed from the Shields' curve as modified by Mantz (1977) and shown in Figure 3.18. The Shields' curve is discretized in CHANNEL as (Hirschi, Barfield, and Moore; 1985)

$$\begin{aligned} Y_{cr} &= \frac{0.1}{R_{e_b}^{0.3}} && R_{e_b} < 1.0 \\ Y_{cr} &= \frac{0.1}{R_{e_b}^{0.5}} && 1.0 \leq R_{e_b} < 10.8 \\ Y_{cr} &= 0.02 R_{e_b}^{0.177} && 10.8 \leq R_{e_b} < 120.0 \\ Y_{cr} &= 0.047 && R_{e_b} \geq 120.0 \end{aligned} \qquad (151)$$

where R_{eb} is the boundary Reynold's number. The particle transport can then be calculated from

$$\begin{aligned} \frac{T_c}{S_g d \rho U_*} &= 0.0635\delta\left[1 - \frac{1}{\beta}\ln(1+\beta)\right] \\ \beta &= 2.45 S_g^{-0.4} Y_{cr}^{0.5} \delta \\ \delta &= \frac{Y}{Y_{cr}} - 1 \\ Y &= \frac{U_*^2}{(S_g - 1) g d} \end{aligned} \qquad (152)$$

where T_c is the transport capacity, S_g is particle specific gravity, d is particle diameter, ρ is fluid density, and others as previously defined.

3.4.2.2. Multiple Particle Transport Capacity

For sediment mixtures, the transport capacity is distributed among particle classes. This

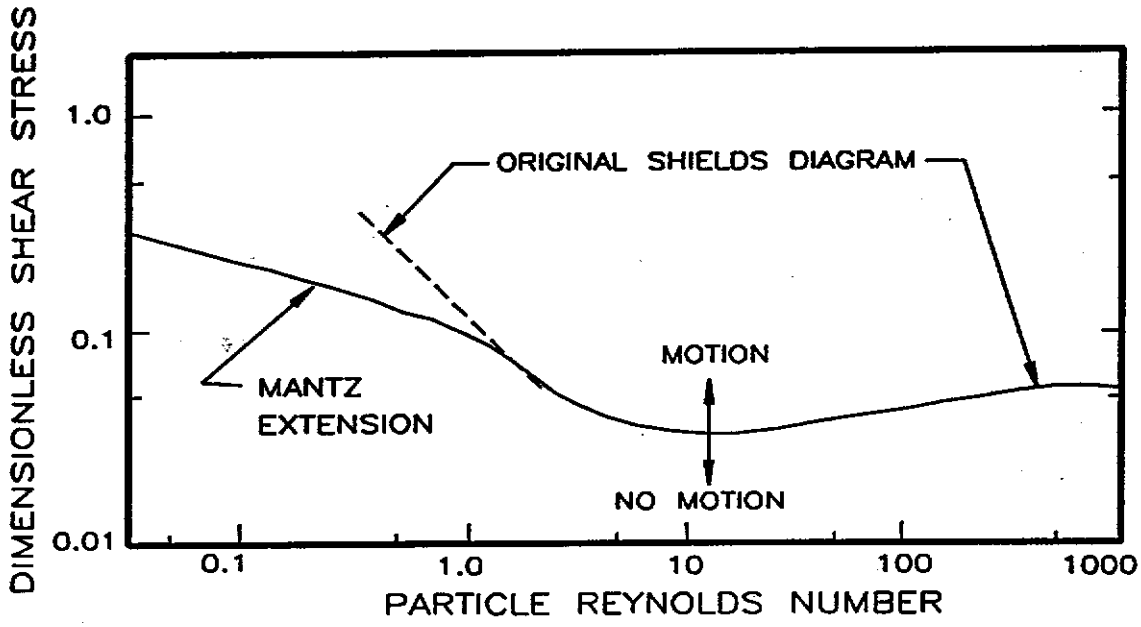

Figure 3.18. Shields' diagram as modified by Mantz (1977).

is done by the following:

(1) total δ for the sediment mixture (n particle types):

$$T = \sum_{i=1}^{n} \delta_i$$

$$\delta_i = \frac{y_i}{y_{cr}} - 1 \tag{153}$$

(2) Calculate the effective number of transport particles $[Ne]_i$:

$$[Ne]_i = N_i \frac{\delta_i}{T} \tag{154}$$

where N_i is the total number of particles of type i for a uniform material.

(3) Calculate the effective dimensionless transport rate:

$$[\phi_e]_i = \phi_i \frac{\delta_i}{T} \tag{155}$$

where $[\phi_e]_i$ is the effective mass for particle type i in the mixture and ϕ_i is the ϕ evaluated for particle type i with uniform material.

(4) Calculate the potential transport capacity for particle type i in a mixture, T_{cpi}:

$$T_{cpi} = [\phi_e]_i \, S_{gi} \, d_i \sqrt{\rho_w \tau} \tag{156}$$

When there was excess transport capacity in a particle class and a deficit in another, shift the transport capacity in order to utilize all existing transport using the following steps.

A. When the sediment load for particle class i, q_{si}, was less than or equal to T_{cpi}, ($q_{si} \leq T_{cpi}$), calculate the required transport ϕ_{ri}:

$$\phi_{ri} = \frac{q_{si}}{S_{gi} \, d_i \sqrt{\rho_w \tau}} \tag{157}$$

Calculate the actual transport capacity, T_{ci}, for particle class i:

$$T_{ci} = q_{si} \tag{158}$$

B. For all particle classes where $q_{si} \leq T_{cpi}$, calculate the fraction of total transport capacity actually needed:

$$SPT = \sum_{i=1}^{n-n_{xc}} \frac{\phi_{ri}}{\phi_i} \tag{159}$$

where n_{xc} was the number of particle classes where $q_{si} > T_{cpi}$.

C. Calculate the excess sediment transport fraction, E_{xc}, that was distributed among the transport deficit classes:

$$E_{xc} = 1 - SPT \tag{160}$$

D. For the transport deficit particle classes where $q_{si} > T_{cpi}$, calculate the sum of the δ_i's:

$$SDLT = \sum_{i=1}^{n_{xc}} \delta_i \tag{161}$$

E. Distribute the excess transport capacity among the n_{xc} particle classes for $q_{si} > T_{cpi}$ in proportion to their individual δ_i:

$$T_{ci} = \frac{\delta_i}{SDLT} E_{xc} \phi_i S_{gi} d_i \sqrt{\rho_w \tau} \tag{162}$$

F. If after repeating steps 1-5 all n particle classes had $q_{si} > T_{ci}$, it was assumed that the proper transport capacities were found.

G. If after repeating steps 1-5 all n_{xc} particle classes had $q_{si} < T_{ci}$, redistribute the excess transport capacity equally among all n particle classes:

$$SMUS = \sum_{i=1}^{n} \frac{\phi_{ri}}{\phi_i} \tag{163}$$

$$T_{ci} = \frac{q_{si}}{SMUS} \tag{164}$$

3.4.3. Detachment/Deposition Processes

Knowing the sediment load, shear distribution, and transport capacity at a cross section, the amount of detachment or deposition occurring on the cross section can be calculated. Discussion will begin with detachment, followed by a discussion of deposition.

3.4.3.1. Detachment

Given the shear distribution along a cross section boundary, and given that the transport capacity exceeds the sediment load, the potential detachment rate is given by

$$D_{rcj} = K_j(\tau_j - \tau_{cj}) \tag{165}$$

where D_{rcj} is the potential detachment rate on segment j, K_j is an erodibility constant, τ_j is the shear force acting on segment j, and τ_{cj} is the critical shear. The total potential detachment rate

on a cross section is the sum of the segment potentials, or

$$D_{rc} = \sum D_{rc_j} = \sum K_j(\tau_j - \tau_{c_j}) \quad (166)$$

Equations (165) and (166) are straightforwardly applied to cross sections having no previously deposited sediment. Calculation of potential detachment on cross sections with previously deposited sediment requires several steps. These steps are outlined below.

(1) Calculate the detachment potential on all matrix material exposed to the flow including 'peaks' between valleys layered with sediment (if any). See Figure 3.19.

(2) Calculate the detachment potential from the exposed sediment layer.

(3) If the sum of the potential detachment from the sediment layer is less than the mass contained in the layer, the detachment potential is 'filled' and no further computations are necessary.

(4) If the sum of the detachment potential from the sediment layer is greater than the mass contained in the layer, the rest of the potential detachment must come from subsequent layers and the 'newly exposed' matrix material (see Figure 3.20). If this is the case, the following procedure is required:

A. Calculate the detachment potential deficit left by the layer or

$$DPD = D_{rc_L} - M_L \quad (167)$$

where DPD is the detachment potential deficit, D_{reL} is the potential detachment from the layer having insufficient mass, and M_L is the mass of the layer.

B. The DPD is the amount of mass required to complete the detachment potential and is in terms of the current sediment layer's properties. This must be addressed when calculating the potential from the next layer and newly exposed matrix. Calculate

$$RATIO_m = \frac{K_m}{K_{L_c}} \quad (168)$$

$$RATIO_d = \frac{K_{L_n}}{K_{L_c}} \quad (169)$$

where K_m is the matrix material erodibility constant, K_{Lc} is the erodibility of the current layer, and K_{Ln} is the erodibility of the next layer. K_m is the weighted average of the K_j values for the newly exposed matrix material segments.

C. Determine the newly exposed perimeter length (WPP).

D. Calculate the shear excess on the newly exposed matrix material and sediment layer. Since CHANNEL deposits sediment horizontally on a cross section

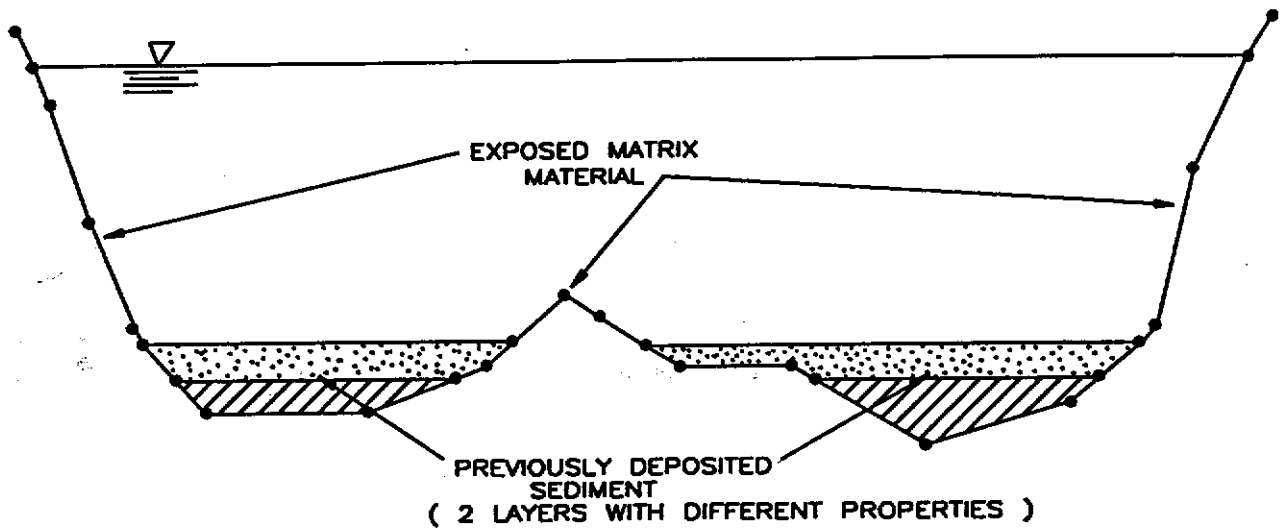

Figure 3.19. A typical cross section with previously deposited sediment.

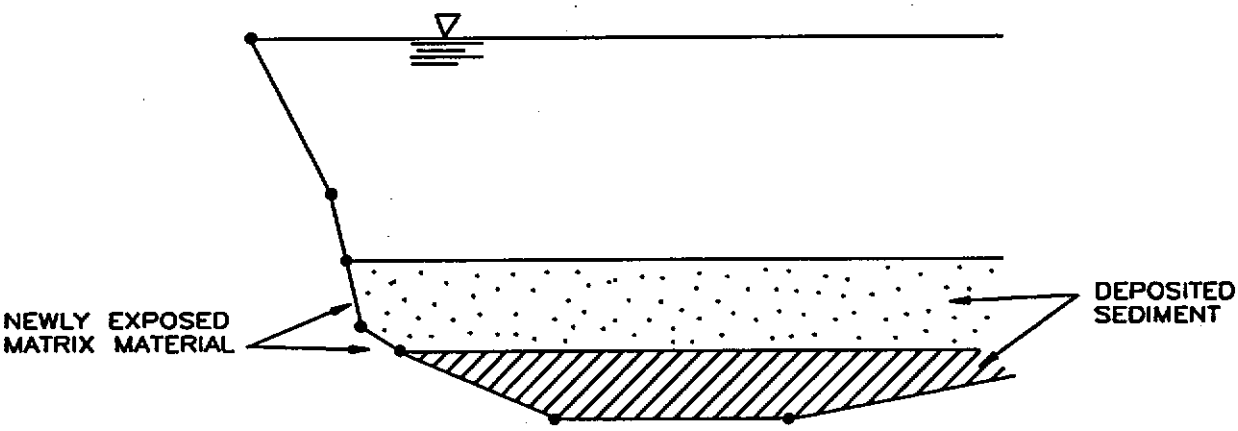

Figure 3.20. Location of newly exposed matrix material upon removal of top sediment layer.

(to be discussed in a subsequent section), the shear was determined on a segment with an angle of zero (from horizontal). Application of that shear to a newly exposed segment with a different angle would be inappropriate. CHANNEL multiplies the shear by the cosine of the newly exposed segment angle, β, or

$$\tau_{e_j} = \tau_j \cos\beta \tag{170}$$

The shear excess becomes

$$SE = \tau_{e_j} - \tau_{c_{e_j}} \tag{171}$$

where τ_{ej} is the shear applied to the newly exposed segment, and τ_{ecj} is the critical shear of the segment material.

E. Calculate the newly exposed surfaces potential detachment rate from:

matrix material:

$$D_{rc_{e_j}} = RATIO_m \frac{\left(\tau_{e_j} - \tau_{c_{e_j}}\right)}{\left(\tau_j - \tau_{c_j}\right)} \frac{\lambda_j}{WPP} DPD \tag{172}$$

sediment layer:

$$D_{rc_{e_j}} = RATIO_d \frac{\left(\tau_j - \tau_{c_{L_j}}\right)}{\left(\tau_j - \tau_{c_j}\right)} \frac{\lambda_j}{WPP} DPD \tag{173}$$

where D_{rcej} is the detachment potential on segment j (newly exposed), λ_j is the newly exposed segment length, τ_{cLj} is the critical shear of the newly exposed sediment layer and others as previously defined.

F. Repeat steps A. - E. until the deficit is filled or all deposited sediment has been removed.

After obtaining the potential detachment rate, the actual rate of detachment can be determined from

$$D_{r_j} = D_{rc_j}\left(1 - \frac{q_s}{T_c}\right) \tag{174}$$

where D_{rj} is the actual detachment rate on a segment. Actual detachment rate calculations are made following the same procedure as outlined above for potential detachment except that the term $(1 - q_s/T_c)$ is carried through the calculations. The total detachment rate on a cross section is given by

$$D_r = \sum D_{r_j} \tag{175}$$

The amount of mass detached from a cross section segment is given by

$$M_D = D_{r_j} \Delta t \tag{176}$$

where Δt is the time increment used during the computation. M_D values are stored for use in the routine that produces changes to channel geometry. The detachment rate is distributed among particle size classes by

$$D_{r_{jk}} = D_{r_j}(PF_k) \tag{177}$$

where PF_k is the fraction of mass in class size k.

3.4.3.2. Deposition

When total sediment load exceeds the total transport capacity, the potential rate of deposition is calculated from

$$D_{rc} = T_c - q_s \tag{178}$$

Equation (178) yields potential deposition in terms of a "negative" potential detachment. The actual deposition rate is determined from

$$D_{r_k} = \frac{V_{s_k}}{q}(T_{c_k} - q_{s_k}) \tag{179}$$

where D_{rk} is the deposition rate of the k^{th} particle class, V_{sk} is the k^{th} class settling velocity, q is the flow rate per unit channel width, T_{ck} is the transport of the k^{th} class, and q_{sk} is the portion of the sediment load comprised only of particles in the k^{th} class. The total deposition rate is the sum of the deposition in each class, or

$$D_r = \sum D_{r_k} \tag{180}$$

The total mass deposited at a cross section is given by equation (176). When CHANNEL calculates the deposition rate, it accounts for channel slope. Vertical and near vertical faces within scour holes will not have any material deposited upon them. CHANNEL accounts for this when calculating V_{sk}. V_{sk} in equation (179) is actually the component of the settling velocity normal to the boundary or

$$V_{s_{k_n}} = V_{s_k} \cos\beta \tag{181}$$

where β is the slope angle and V_{skn} is the value used in equation (179).

3.5. SEDIMENT ROUTING

To route sediment, CHANNEL uses equation (88):

$$\frac{\partial q_s}{\partial x} = D_r + D_L \tag{88}$$

In cases of open channel flow, submerged jets, and hydraulic jumps, equation (88) is applied using the following procedure:

(1) Begin at the first cross section of the channel (inlet section). This is labeled cross section i in the following steps.

(2) Knowing the sediment load and transport capacity at i, calculate the potential detachment/deposition rate and the actual detachment/deposition rate as per sections 3.4.3.1 and 3.4.3.2. At section i, the sediment load is input by the user if it is the inlet section. For subsequent sections, the sediment load at i is determined from previous calculations.

(3) Estimate the sediment load at section i+1. The first estimate is taken to be the lateral inflow sediment load. Subsequent estimates are calculated from

$$q_{s_{i+1}} = q_{s_i} + D_{r_{i+\frac{1}{2}}} + D_{L_{i+1}} \tag{182}$$

where $D_{ri+1/2}$ is the detachment/deposition rate at some point (called the ω point) between i and i+1. The user chooses where this point will fall between i and i+1. If the user inputs a value of $\omega = 0$, the ω point falls at i+1. If $\omega = 1$, the ω point is at i. If $\omega = 0.5$, the point falls midway between i and i+1.

(4) Calculate the potential detachment/deposition rate at section i+1.

(5) Calculate the transport capacity at section i+1 using the sediment load calculated in step (3).

(6) Estimate the sediment load at i+1/2 from

$$q_{s_{i+\frac{1}{2}}} = \omega q_{s_i} + (1 - \omega) q_{s_{i+1}} \tag{183}$$

(7) Estimate the transport capacity at i+1/2 from

$$T_{c_{i+\frac{1}{2}}} = \omega T_{c_i} + (1 - \omega) T_{c_{i+1}} \tag{184}$$

(8) Estimate the potential detachment/deposition rate at i+1/2:

$$D_{rc_{i+\frac{1}{2}}} = \omega D_{rc_i} + (1 - \omega) D_{rc_{i+1}} \tag{185}$$

(9) Estimate the actual detachment/deposition rate at i+1/2:

$$D_{r_{i+\frac{1}{2}}} = D_{rc_{i+\frac{1}{2}}}\left(1 - \frac{q_{s_{i+\frac{1}{2}}}}{T_{c_{i+\frac{1}{2}}}}\right)\cos\beta_{i+\frac{1}{2}} \qquad \textit{detachment}$$

$$D_{r_{i+\frac{1}{2}}} = D_{rc_{i+\frac{1}{2}}}\left(1 - \frac{q_{s_{i+\frac{1}{2}}}}{T_{c_{i+\frac{1}{2}}}}\right) \qquad \textit{deposition} \qquad (186)$$

where $\beta_{i+1/2}$ is the slope angle at i+1/2. The term $\cos\beta_{i+1/2}$ is included in the detachment equation to account for the reduction of sediment load as a factor in the transport of particles on steeper slopes. In other words, on a vertical or near vertical slope, particles will be transported regardless of the sediment load in the flow. This same phenomenon is accounted for in deposition during the calculation of V_{sk} in equation (179).

(10) Estimate a new sediment load at i+1 using equation (182).

(11) Compare new sediment load at i+1 with previous estimate. If the difference is within tolerance, move the routing one cross section downstream and begin again. If the difference is not within tolerance, repeat steps 4-10 until the old and new estimates of sediment load at i+1 converge to a value within tolerance.

The above procedure continues until the end of the channel is reached or an impinging jet is encountered. When an impinging jet is encountered, the above procedure stops at the jet brink. At this point, the sediment load in the jet at the brink is partitioned into upstream and downstream components by

$$q_{s_d} = q_{s_{jet}} R_d$$
$$q_{s_u} = q_{s_{jet}} R_u \qquad (187)$$

where R_d and R_u are the fractions of the jet that move downstream and upstream, respectively, at the stagnation point. R_d and R_u are given by

$$R_d = \frac{1+\cos\theta}{2} \qquad (188)$$

$$R_u = \frac{1-\cos\theta}{2} \qquad (189)$$

where θ is the angle of impingement. The sum of q_{sd} and q_{su} equals the sediment load at the point of stagnation. The sediment load just upstream of the stagnation point is q_{su} and the sediment load just downstream is q_{sd}.

The routing procedure now begins to move upstream with point i being the stagnation point. Routing continues upstream until the flow is recycled into the jet. At this point the sediment load in the jet becomes

$$q_{s_{jet}} = q_{s_{jet_{old}}} + q_{s_r} \qquad (190)$$

where q_{sr} is the sediment load being recycled into the jet. This process is illustrated in Figure 3.21. The routing begins again at the stagnation point and the process is continued until the jet sediment load has converged to a constant value. The routing then progresses downstream from the impingement point using q_{sd} as the sediment load at point i. The routing continues in this manner until the channel exit is reached.

3.6. CHANGING CHANNEL GEOMETRY

Changes to the overall channel shape are accomplished by making adjustments to each of the channel's cross sections. Procedures for adjusting the cross sections are different under conditions of detachment than conditions of deposition.

3.6.1. Changes Resulting from Detachment

As the actual detachment rate on each cross section segment is calculated, CHANNEL calculates the mass detached by

$$M_{D_j} = D_{r_j} \Delta t \tag{191}$$

where M_{Dj} is the mass detached on segment j and Δt is the length of the time step. Using M_{Dj}, the segment displacement vector magnitude is calculated from

$$(Disp)_j = \frac{M_{D_j}}{\rho_{bj} L \lambda_j} \tag{192}$$

where ρ_b is the material bulk density, λ_j is the segment length, and L is the length of the channel represented by the cross section and is determined by

$$L = \frac{(\Delta L_{i-1} + \Delta L_{i+1})}{2} \tag{193}$$

where ΔL_{i-1} and ΔL_{i+1} are the distances from the cross section under consideration and the two adjacent cross sections upstream and downstream the channel respectively. After obtaining the displacement magnitudes for each segment, the magnitude of the displacement vector of each node on the cross section is determined by

$$(Disp)_{j_{avg}} = (Disp)_j WF_j + (Disp)_{j+1} WF_{j+1} \tag{194}$$

and the resultant angles by

$$\varepsilon_{j_{avg}} = \varepsilon_j WF_j + \varepsilon_{j+1} WF_{j+1} \tag{195}$$

where

$$WF_j = \frac{\lambda_j (Disp)_j}{\lambda_j (Disp)_j + \lambda_{j+1} (Disp)_{j+1}} \tag{196}$$

and ε_{javg} is the angle of the displacement vector for segment j. This process is illustrated by Figure

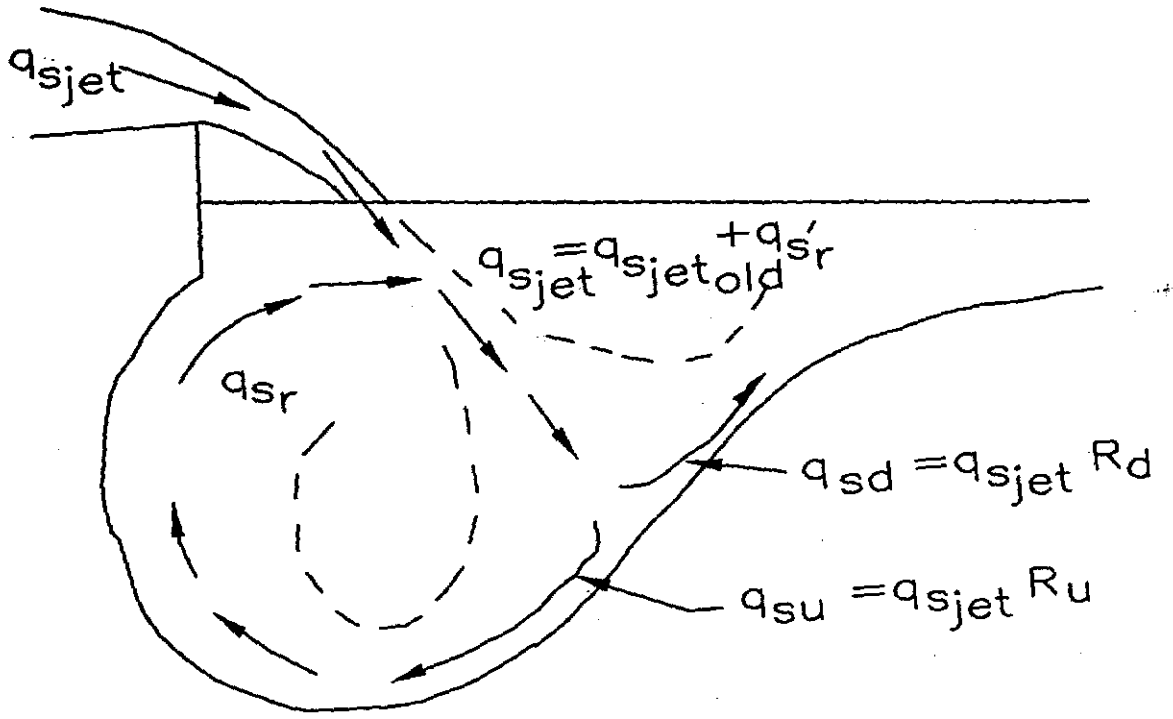

Figure 3.21. Partitioning of the sediment load within an impinging jet.

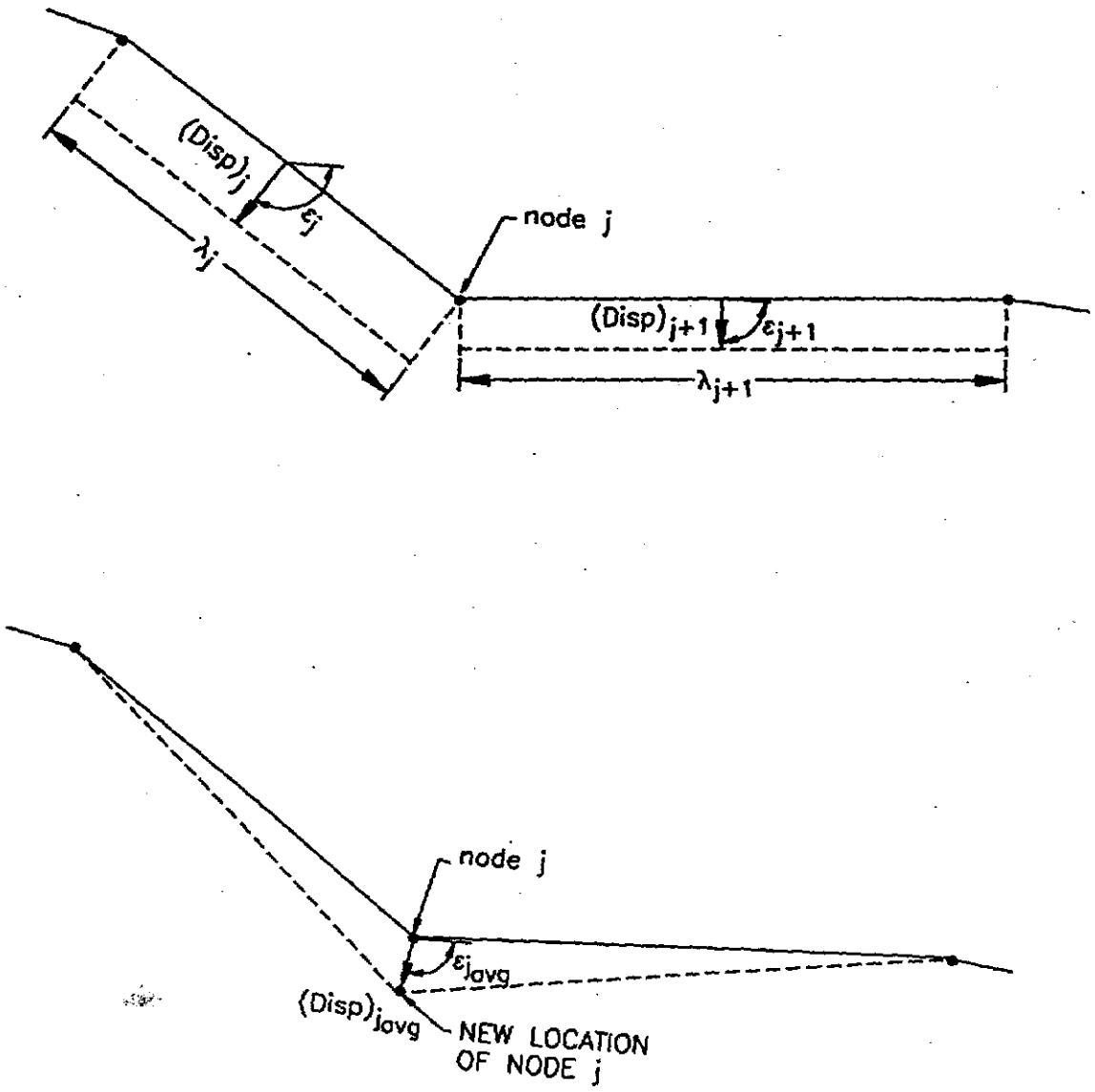

Figure 3.22. Channel boundary movement algorithm.

3.22.

A drawback of the above procedure is that as cross section nodes get close together, the chances for cross section segments to intersect at points other than at the node points increases. If segments intersect at points other than at the nodes, as illustrated in Figure 3.23, computational problems arise. CHANNEL does not allow this to occur and accomplishes the task by applying the same technique to the displacement vectors as is applied to the segment bisectors in the Lundgren and Jonsson (1964) area method as presented in section 3.4.1.1. The only difference between the two applications is that the lowest point of nodal displacement in the cross section is used instead of the water surface.

3.6.2. Changes Resulting from Deposition

After calculating the deposition rate of each particle class the total mass to be deposited is calculated by

$$M_{dep} = D_r \Delta t \tag{197}$$

and the fraction of the total mass contained in each class by

$$PF_k = \frac{D_{r_k}}{\sum D_{r_k}} \tag{198}$$

Utilizing the class fraction data, the following parameters are determined:

Sediment bulk density is calculated by (Hirschi, Barfield, and Moore; 1985):

$$\rho_{bdep} = 1000\left(0.1273 d_{avg}^{-0.21} + 0.755\right) S_{g_{avg}} \tag{199}$$

where ρ_{bdep} is the bulk density of deposited material in kg/m^3, d_{avg} is the weighted average particle diameter in mm, and S_{gavg} is the weighted average particle specific gravity.

Sediment critical shear is calculated utilizing the Shields curve (Hirschi, Barfield, and Moore; 1985) and is defined by

$$\tau_{c_{dep}} = Y_{cr} g \left(S_{g_{avg}} - 1\right) d_{avg} \rho \tag{200}$$

where τ_{cdep} is the sediment critical shear, Y_{cr} is the critical mobility number, g is the acceleration of gravity, and ρ is the fluid density.

CHANNEL proceeds to determine the thickness of the deposit. The cross sectional area of the deposit is first calculated by

$$A_{dep} = \frac{M_{dep}}{\rho_{b_{dep}} L} \tag{201}$$

where M_{dep} is the mass of sediment to be deposited and L is the length of the channel where the cross section is representative. With A_{dep}, CHANNEL determines the horizontal elevation of the top of the deposit, depicted in Figure 3.24, and the new boundary corresponds to the top of the deposit.

If previously deposited sediment exists on the cross section, CHANNEL compares the

Figure 3.23. Illustration of cross section segment intersection at points other than the nodes.

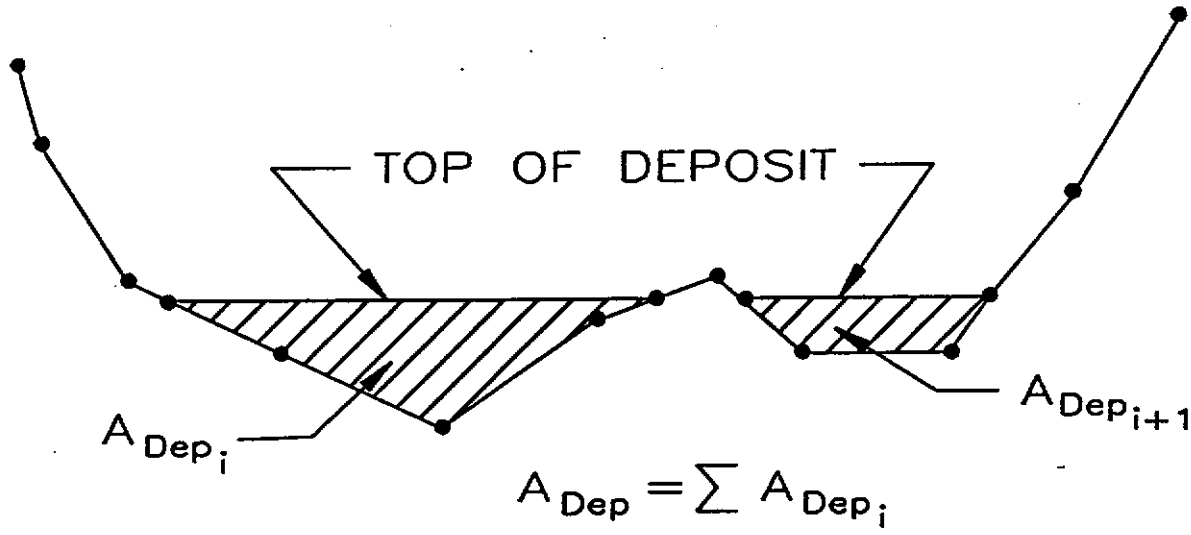

Figure 3.24. Deposition of sediment upon a cross section.

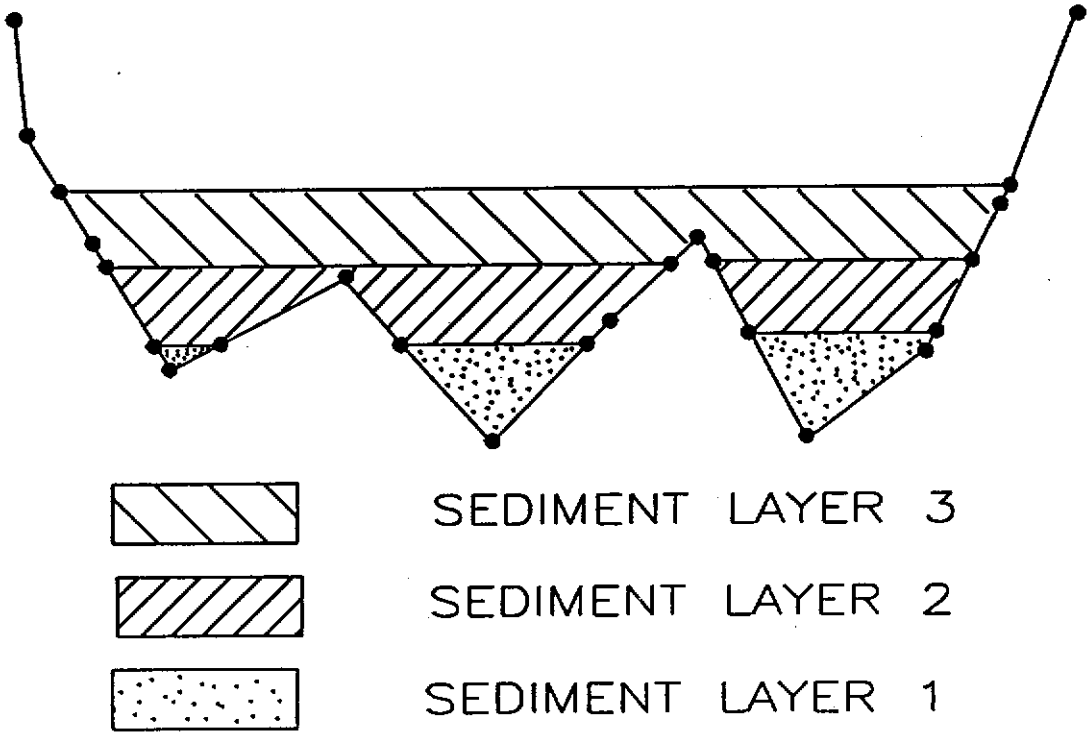

Figure 3.25. Deposition of sediment upon a cross section with previously deposited sediment.

calculated values of ρ_b and τ_c of the sediment being deposited with the values of the previously deposited material. If the percent difference in either ρ_b or τ_c exceeds the allowable percent difference input by the user, the model makes a distinction between the sediments and keeps track of the sediment layers throughout subsequent computations. This is illustrated in Figure 3.25. If the percent differences are not significant the sediment is assimilated into the existing layer and the new layer's properties are assumed to be the weighted averages of the previous layer's and the currently deposited material's properties.

3.6.3. Changes Resulting from Shear on the Channel Banks While Depositing Material on the Bed

When sediment load exceeds the transport capacity, the channel tends to become wider and more shallow. This is due to the shearing away of sediment on the banks while depositing on the bed. In CHANNEl, the user may opt to use a channel widening algorithm on cross sections where deposition occurs. Detachment on the walls is not transport limited. The algorithm is outlined below and illustrated in Figure 3.26.

(1) Deposit sediment on channel bottom.

(2) Calculate detachment on sidewalls exposed to the flow above the sediment.

(3) Calculate the mass to be deposited from the sidewalls.

(4) Deposit the sediment on the bottom with the algorithm given in section 3.6.2.

(5) Calculate the displacement of the sidewalls by the algorithm presented in section 3.6.1.

3.6.4. Changes Due to Headwall Sloughing

Once a scour hole with a headwall has formed in the channel and an impinging jet has begun to undercut the headwall, CHANNEL checks for headwall sloughing. This is done by locating the undercut extremes as shown in Figure 3.27. If the horizontal distance, λ, between the extremes exceeds a user specified limit, λ_c, CHANNEL begins the headwall sloughing algorithm.

The first step is to calculate the slough area at each cross section in the headwall. This area is shown in Figure 3.28. CHANNEL assumes a vertical headwall face is formed after sloughing. These slough areas area translated into a slough volume by multiplying the slough area at each section by the depth of the cross section slice. Cross section slices are illustrated in Figure 3.29. The sum of the slice volumes is an estimate of the total slough volume.

CHANNEL proceeds to determine the depth of the deposited material above the lowest point in the scour hole. This process begins by assuming a depth, calculating the volume in the scour hole below the assumed depth, and comparing the scour hole volume with the slough volume. If the volumes don't equal to within tolerance, a new depth is assumed and the process continues until the correct depth is found. The sloughed mass is then deposited on each cross section below the deposit depth using the procedures outlined in section 3.6.2. The resulting channel shape is shown in Figure 3.30.

3.7. PROFILE CHARACTERIZATION

At the end of each time step, CHANNEL checks each GVFR for developing scour holes. The potential for a scour hole exists if:

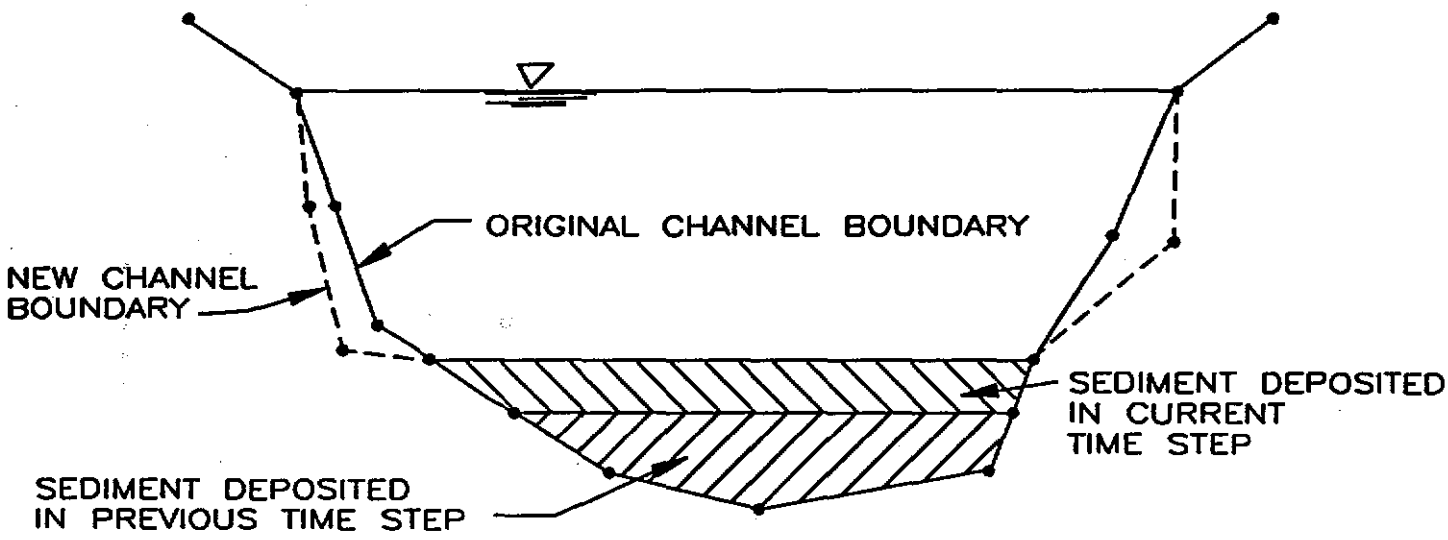

Figure 3.26. Channel widening during deposition.

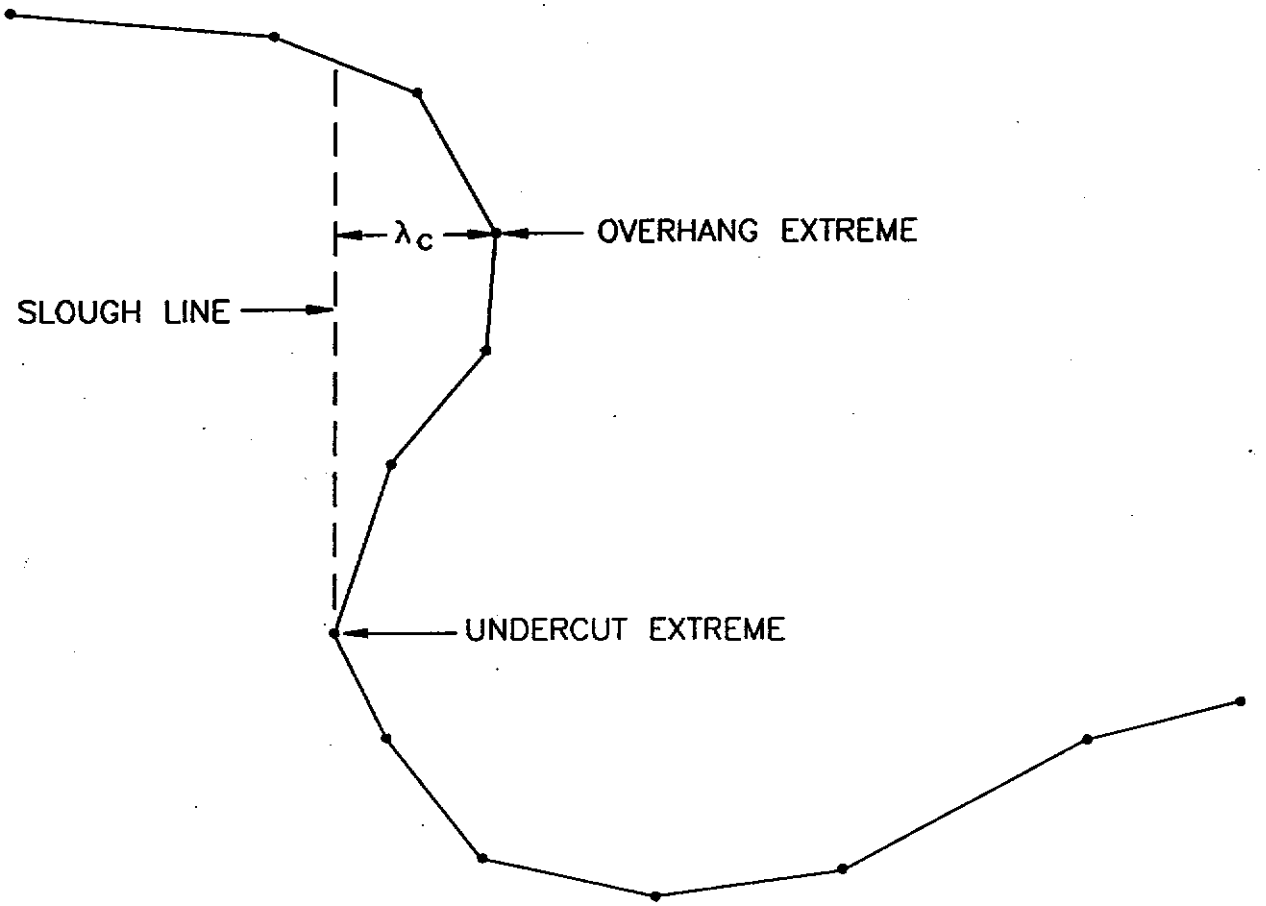

Figure 3.27. Headwall undercut extremes.

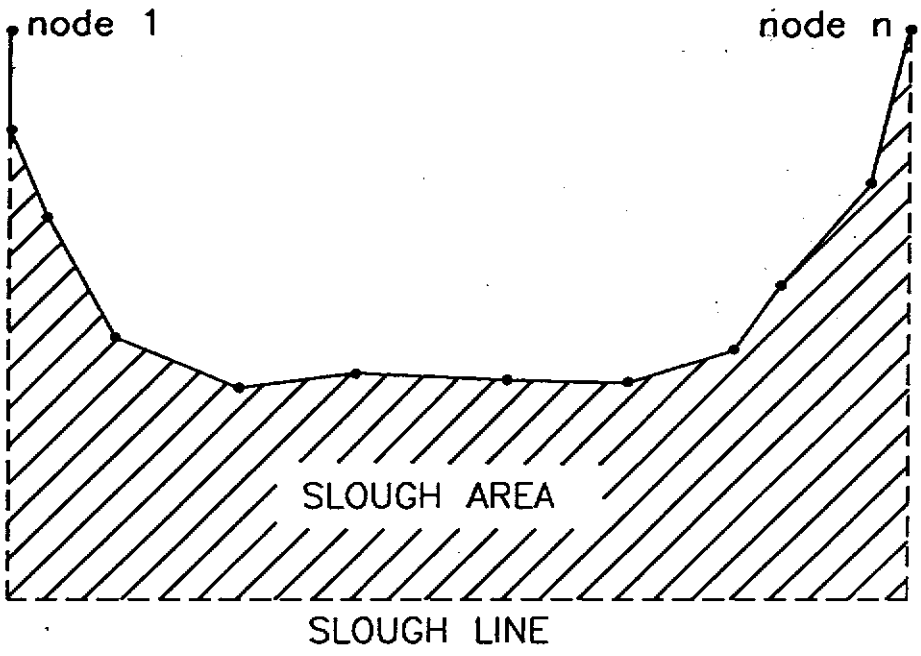

Figure 3.28. Slough area at a random cross section on the headwall.

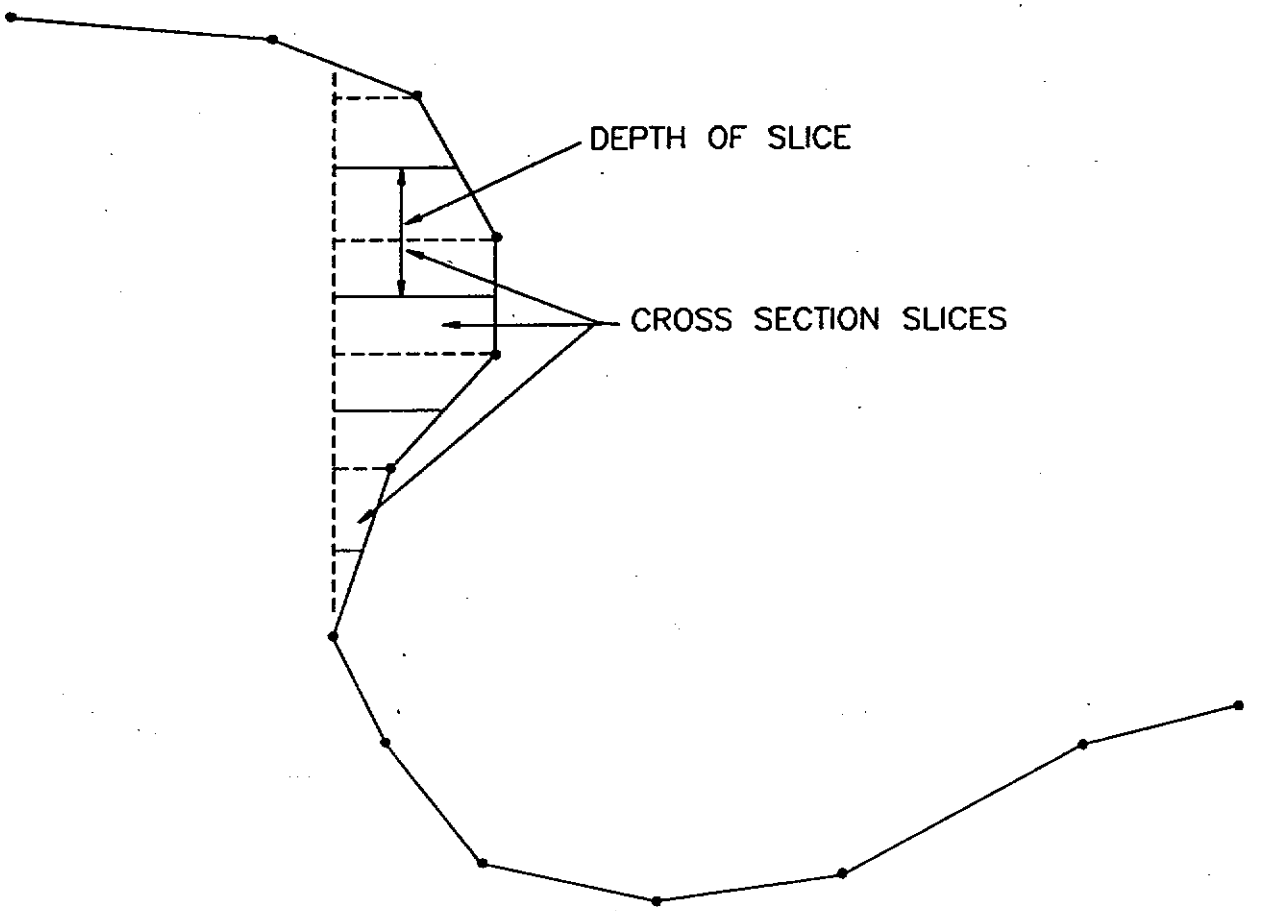

Figure 3.29. Illustration of cross section 'slices' used in calculating headwall slough volume.

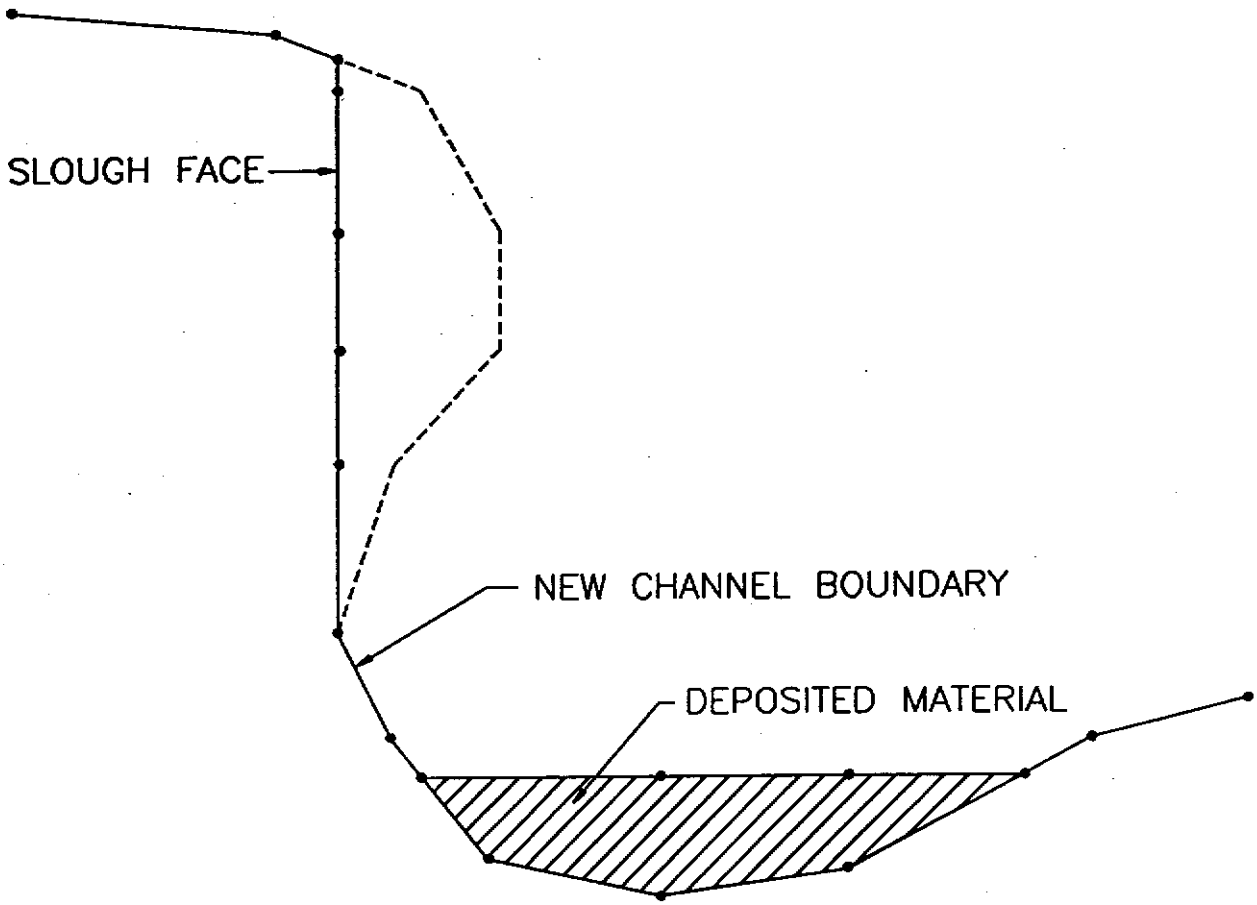

Figure 3.30. New channel shape after headwall sloughing.

(1) A profile segment transitions from subcritical to supercritical slope (see Figure 3.31) and the angle α exceeds a user defined angle, α_*.

(2) The user indicates the boundaries of a scour hole at the time of input.

If it is determined that the start of a scour hole exists, the scour hole exit is defined as the first downstream segment that has a mild slope after a region of adverse slope; or the model encounters the end of the channel; or the model travels past a user specified number of profile segments.

CHANNEL also has the ability to add cross sections to the channel in regions that require a higher degree of profile resolution, such as the jet impingement regions. To do this, the model takes the two cross sections bounding the section of profile where the new section is to be added, and produces an average cross section shape. This new shape is weighted toward the closest parent section. The closer the new section is to a particular parent, the more it looks like that parent section.

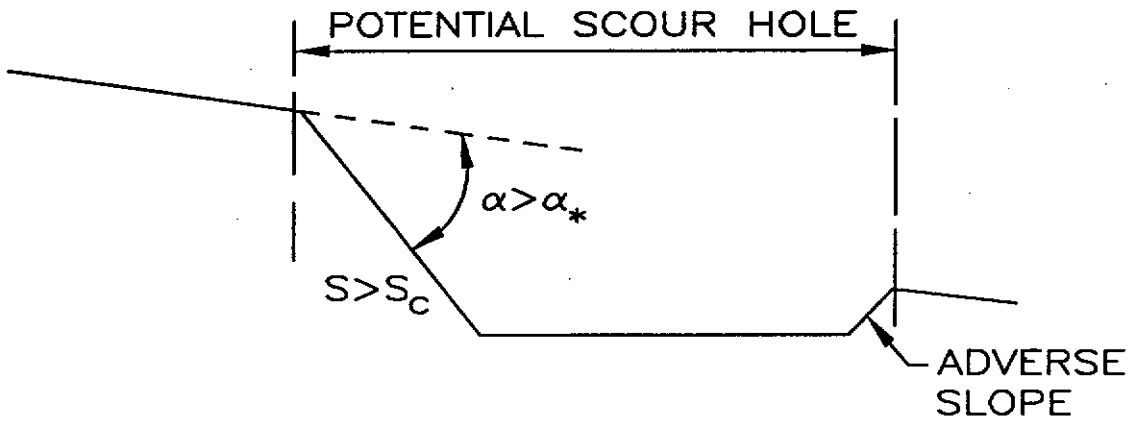

Figure 3.31. Definition of the limits of a potential scour hole.

CHAPTER 4

SUMMARY

As presented in the previous chapters, models were developed which predict channel erosion resulting from shear in gradually varied flow, shearing forces resulting from submerged and hydraulic jumps, and shearing forces resulting from free jets impinging a plunge pool. These models are linked with a pseudo-steady-state runoff routing algorithm to develop the CHANNEL model. This model predicts general channel erosion resulting from time varying gradually varied flow as well as from the development and propagation of channel headwalls. The modeling approach is modular and fundamentally based.

CHANNEL uses the standard step method coupled with hydraulic jump and jet trajectory prediction models to calculate the flow profile through the channel in each time step. The model checks for hydraulic jump, submerged jet, and/or free jet formation within the scour hole(s) and adjusts the flow profile accordingly. The flow phenomenon present within the scour hole(s) determines the shear models used in the sediment generation component of the model.

To begin sediment generation calculations, CHANNEL first determines which shear model is appropriate (longitudinal or lateral distributions). After the shear distributions have been calculated, the longitudinal shear distributions are transformed into lateral shear distributions along each cross section boundary. Shear transformations are based upon the jet thickness as determined by the variation of the flow depth at the jet brink. Given the shear distributions, CHANNEL uses the shear excess concept to make detachment calculations. Interactions between detachment/deposition, transport capacity, and sediment load are defined by the Foster and Meyer (1972a) model. Sediment routing is done by solving the pseudo-steady-state sediment routing equation.

CHANNEL uses a simple movement vector calculation model to make changes to the channel boundary. All changes are effected on individual cross sections. Profile changes are inherent in the changes made to the cross sections due to the cross section linkage method of profile representation.

As the simulation progresses through time, CHANNEL checks for headwall formation, undercutting, sloughing, and upstream propagation. It is also capable of varying the number of cross sections in a given reach to improve the resolution in the sediment routing routines.

As of this writing, the CHANNEL model can successfully simulate scour hole development and headwall sloughing and propagation. Some problems still exist in handling the transition to free jets within scour holes.

REFERENCES

Ackers, P. and W. R. White. 1973. Sediment transport; New approach and analysis. Jour. Hydr. Div., ASCE 99(HY11):2041-2060.

Alonso, C. V., W. H. Neibling and G. R. Foster. 1981. Estimating sediment transport capacity in watershed modeling. Trans. ASAE, 24(5):1211-1220, 1226.

Beltaos, S. 1976a. Oblique impingement of plane turbulent jets. J. Hydr. Div., ASCE 102(HY9):1177-1192.

Beltaos, S. 1976b. Oblique impingement of circular turbulent jets. J. Hydr. Res. 14(10:17-36.

Beltaos, S. and N. Rajaratnam. 1973. Plane turbulent impinging jets. J. Hydr. Res. 11:29-59.

Beltaos, S. and N. Rajaratnam. 1974. Impinging circular turbulent jets. J. Hydr. Div., ASCE 100 (HY10):1313-1328.

Beltaos, S. and N. Rajaratnam. 1977. Impingement of axisymmetric developing jets. J. Hydr. Res. 15(4):311-325.

Blevins, R. D. 1984. Applied fluid dynamics handbook. Van Nostrand Reinhold Co.

Bormann, N. E. and P. Y. Julian. 1991. Scour downstream of grade control structures. J. Hydraulic Engr. 117(5):579-594.

Brush, L. M. and M. G. Wolman. 1960. Knickpoint behavior in noncohesive materials: A laboratory study. Bull. Geol. Soc. Amer. 71(1):59-74.

Chow, V. T. 1959. Open channel hydraulics. McGraw-Hill, New York.

Conte, S. D. and C. de Boor. 1980. Elementary numerical analysis: an algorithmic approach. McGraw Hill, New York.

Davis, S. S. 1978. Deposition of nonuniform sediment by overland flow on concave surfaces. M.S. Thesis. Purdue Univ., W. Lafayette, IN.

Delleur, J. W., J. C. I. Dooge and K. W. Gent. 1956. Influence of slope roughness on the free overfall. J. Hydr. Div. ASCE, 82(HY4):1038-30-1038-35.

Doddiah, D., M. L. Albertson and R. Thomas. 1953. Scour from jets. In: roceedings of a Joint Meeting of the International Assoc. for Hydr. Res. and ASCE, 5th Congress, Minneapolis, MN pp. 161-169.

Einstein, H. A. 1968. Deposition of suspended particles in a gravel bed. Journal of the Hydraulics Division, Proc. of the ASCE, 94 (HY5):1197-1205.

Einstein, H. A. 1950. The bedload function for sediment transportation in open channel flows. Technical Bulletin 1026, Soil Cons. Service, USDA. Washington, D.C.

Finkner, S. C., M. A. Nearing, G. R. Foster, and S. E. Gilley. 1989. A simplified equation for modeling sediment transport capacity. Transactions of the ASAE, 32(5):1545-1550.

Foster, G. R. 1982. Modeling the erosion process. IN: C. T. Haan. (ed.) Hydrology modeling of small watersheds. Monograph No. 5. American Society of Agricultural Engineers, St. Joseph, MI.

Foster, G. R. and L. D. Meyer. 1972a. A closed-form soil erosion equation for upland areas. IN: Sedimentation (Einstein), H. W. Shen (ed.). Colorado State University, Fort Collins, CO Chapter 12.

Foster, G. R. and L. D. Meyer. 1972b. Transport of soil particles by shallow flow. Transactions of the ASAE, 15(1):99-102.

Foster, G. R. and L. D. Meyer. 1975. Mathematical simulation of upland erosion by fundamental erosion mechanics. IN: Present and Prospective Technology for Predicting Sediment Yields and Sources. ARS-S-40. USDA-Agricultural Research Services. pp. 190-207.

Foster, G. R. and L. J. Lane. 1983. Erosion by concentrated flow in farm fields. PP. 9.65-9.82 in Proceedings of the D. B. Simons Symposium on Erosion and Sedimentation. Ft. Collins, Colorado, Colorado State University.

Graf, W. H. 1971. Hydraulics of Sediment Transport. McGraw-Hill Book Co., New York, NY. 544 pp.

Haan, C. T., B. J. Barfield and J. C. Hayes. 1992. Design hydrology and sedimentology for small catchments. Academic Press, New York (In Press).

Hager, W. H. 1983. Hydraulics of plane free overfall. J. Hydr. Eng., ASCE 109(12):1683-1697.

Hager, W. H. 1984. Errata: Hydraulics of plane free overfall. J. Hydr. Eng., ASCE 110(12):1887-1888.

Hansen, G. J., K. M. Robinson and D. M. Temple. 1990. Pressure and stress distribution due to a submerged impinging jet. Proceedings of the ASCE 1990 Conference on Hydraulic Engineering, American Society of Civil Engineers, New York.

Harvey, M. D., C. C. Watson and Stanley Schumm. 1985. Gully erosion. Tech. Note 366, Bureau of Land Management, U.S. Dept. of the Interior, Washington, D.C.

Hirschi, M. C. and B. J. Barfield. 1988a. KYERMO - A physically based research erosion model. Part I. Model development. Transactions of the ASAE, 31(3):804-813.

Hirschi, M. C. and B. J. Barfield. 1988b. KYERMO - A physically based research erosion model. Part II: Model sensitivity analysis and testing. Transactions of the ASAE. 31(3):814-820.

Hirschi, M. C., B. J. Barfield and I. D. Moore. 1985. Modeling erosion on long steep slopes with emphasis on the rilling process. Research Report No. 148, Water Resources Research Institute, University of Kentucky.

Lane, E. W. 1953. Progress report on studies in the design of stable channels by the Bureau of Reclamation. ASCE Proceedings, Irrigation and Drainage Division, Separate No. 280, 31 pp.

Lane, E. W. 1955. Design of stable channels. ASCE Transactions. 120:1234-1279.

Lane, L. J. and M. A. Nearing. 1989. USDA-Water erosion prediction project: Hillslope model documentation. NSERL Report No. 2, USDA-ARS National Soil Erosion Research Laboratory, West Lafayette, IN.

Laursen, E. M. 1958. Total sediment load of streams. Jour. of Hydr. Div., ASCE 84(HY1):1530-1, 1530-36.

Leighly, J. B. 1932. Toward a theory of the morphologic significance of turbulence in the flow of water in streams. University of California Publications in Geography, 6(1):1-22.

Lundgren, H. and I. G. Jonsson. 1964. Shear and velocity distribution in shallow channels. Jour. of Hydr. Division, ASCE, 90(HY1):1-21.

Mantz, P. A. 1977. Incipient transport of fine grains and flakes of fluid - extended shields diagram. Proceedings of the ASCE 103(HY6):601-615.

May, J. H. 1989. Geotechnical aspects of rock erosion in emergency spillway channels. Report 4. Geologic and hydrodynamic controls on the mechanics of knickpoint migration. Tech. Report REMR-GT-3, Geotechnical Laboratory, Waterways Experiment Station, US Army Corps of Engrs., Vicksburg, MS.

Meyer-Peter, E. and R. Muller. 1948. Formulas for bed load transport. pp. 39-64. IN: Proceedings of the 2nd Congress of the IAHR, Stockholm.

Poreh, M. and E. Hefez. 1967. Initial scour and sediment motion due to an impinging submerged jet. Inter. Assoc. Hydr. Res. Proc. 12th Congress Vol. 3:9-16.

Rajaratnam, N. 1981. Erosion by plane turbulent jets. J. Hydr. Res. 19(4):339-359.

Rajaratnam, N. 1982. Erosion by unsubmerged plane water jets. In: Applying Research to Hydraulic Practice, ASCE Conf. Jackson, MS. pp. 280-288.

Rajaratnam, N. 1983. Theory of turbulent jets. Ch. 10 in Cheremisinoff and Gupta, Eds: Handbook of fluids in motion. Ann Arbor Science, Ann Arbor, MI.

Rajaratnam, N. and D. Muralidhar and S. Beltaos. 1976. Roughness effects on rectangular free overfall. J. Hydr. Div., ASCE 102(HY5):599-614.

Raudkivi, A. J. 1976. Loose Boundary Hydraulics. New York: Pergamon, 397 pp.

Replogle, J. A. and V. T. Chow. 1966. Tractive-force distribution in open channels. Jour. Hydr. Div., ASCE, 92(HY2):169-191.

Rohlf, R. A. 1981. Development of a deterministic mathematical model for interrill and rill runoff and erosion. Unpub. M.S. Thesis, Department of Civil Engineering, University of Kentucky, Lexington, KY, 84 pp.

Rouse, H. 1936. Discharge characteristics of the free overfall. Civil Engineering 6(4):257-260.

Rouse, H. 1943. Discussion: Energy loss at the base of a free overfall. Transactions ASCE 108(2204):1383-1387.

Schumm, S. A., M. D. Harvey and C. C. Watson. 1984. Incised Channels: Morphology, Dynamics, and Control. Water Resources Publ., Littleton, CO.

Shields, A. 1936. Application of the theory of similarity and turbulence research to the bed load movement. (In German) Mitt. Preuss. Vers. Wasser Schiff., 26:5-24.

Simon, A. L. 1986. Hydraulics. John Wiley and Sons, New York.

Simons, D. B. and F. Senturk. 1977. Sediment Transport Technology. Ft. Collins, CO; Water Resources Publication.

Stein, O. B. 1990. Mechanics of headcut migration in rills. Doctoral dissertation, Colorado State University, Ft. Collins, CO.

Storm, D. E., B. J. Barfield and L. Ormsbee. 1990. Hydrology and sedimentology of dynamic rill networks. Vol. I:B Erosion model development. Research Report No. 178. Kentucky Water Resources Research Institute, University of Kentucky, Lexington, KY.

Strelkoff, T. S. and M. S. Moayeri. 1970. Pattern of potential flow in a free overfall. J. Hydr. Div., ASCE 96(HY4):879-901.

Yalin, M. S. 1963. An expression for bed-load transportation. Proceedings of the ASCE, 89(HY3):221-250.

Yalin, M. S. 1977. Mechanics of Sediment Transport. 2nd ed. Pergamon Press. 298 pp.

Yang, C. T. 1973. Incipient motion and sediment transport. Jour. of the Hydr. Div., Proc. of the ASCE, 99(HY10):1679-1704.

Wang, Y., G. R. Foster, and B. N. Wilson. 1992. Channel erosion processes. ASAE paper No. 922003. American Society of Agricultural Engineers, St. Joseph, MI 49085.

Wilson, B. N. 1992. A detachment model for cohesive sediment. ASAE Paper No. 922020. American Society of Agricultural Engineers, St. Joseph, MI 49085.